UTPP-47

Search for New Neutral Gauge Bosons in 1.8-TeV Proton-Antiproton Collisons

Eiichiro HAYASHI

A dissertation submitted to the Doctoral Program
in Physics, the University of Tsukuba
in partial fulfillment of the requirements for the
degree of Doctor of Philisophy (Science)

September 1996

Search for New Neutral Gauge Bosons in 1.8-TeV Proton-Antiproton Collisions

Eiichiro HAYASHI

A dissertation submitted to the Doctoral Program
in Physics, the University of Tsukuba
in partial fulfillment of the requirements for the
degree of Doctor of Philosophy (Science)

September 1996

Abstract

We have searched for additional neutral heavy bosons in dielectron decay mode in $\overline{p}p$ collisions at $\sqrt{s} = 1.8\,\mathrm{TeV}$ using the CDF detector for dielectron invariant mass above 150 GeV/c^2. The data were collected during the 1992-1993 and 1994-1995 runs corresponding to an integrated luminosity of 110 pb^{-1}. The largest invariant mass observed is 511 GeV/c^2. We present a 95% confidence level limit on the production cross section times branching ratio for a Z' decaying into an electron pair, $\sigma_{Z'} \cdot \mathrm{B}(Z' \rightarrow e^+e^-)$, as a function of the dielectron invariant mass. Assuming standard model coupling strengths, we exclude Z' mass below 655 GeV/c^2 at 95% confidence level. In addition, we set lower bounds on the Z' mass for several models based on the E_6 symmetry group and the alternative left-right model.

Acknowledgements

I would like to thank Professor Kunitaka Kondo for his support throughout my graduate career. He provided me with the opportunity to work at CDF. I have learned from his attitude toward physics that how one should confront a huge amount of tasks and conduct a careful experiment. I am also grateful for his careful reading of the text and his many criticisms to the point.

I am especially grateful to Dr. Kaori Maeshima for her continuous support and encouragement. She suggested the topic of this thesis, provided me with guidance at crucial points in the analysis, and commented on all sections of the text. I learned a great deal from her precise way of thinking. I could not have finished this work without her continuous support.

I want to thank Professor Koji Takikawa and Professor Shinhong Kim for their continued encouragement and their support throughout my graduate career. Discussions on physics and my analysis with them were very precious.

I want to thank Dr. David Stuart for his careful reading of the text and his suggestions.

Many thanks go to Pawel de Barbaro, Arie Bodek, Carla Grosso-Philcher and Manoj Pillai, who gave me many useful suggestions and advice for this analysis. Also I would like to thank all the people in the exotic group at CDF.

Fumio Abe, Kurt Biery, Robert Kennedy, Youhei Morita, Masaharu Nomachi, Jim Pangburn, Jim Patrick, Elizabeth Sexton and other online group members are appreciated for their help to my work on the data acquisition at CDF.

Discussion on physics and other various things with Yoshihiro Seiya, Ryutaro Oishi, Fumihiko Ukegawa, Mikio Takano and Kiyoshi Yasuoka were very beneficial for me.

I also would like to thank Naomi Maeshima Williams for her advice on English.

Conversations with Junsuke Iwai, Nobuaki Oshima made my stay at Fermilab unforgettable. I was very fortunate to have a good time with Takashi Asakawa and Tsuyoshi Takada in Aurora.

I should thank Shin Aota, Hosai Nakada, Junichi Suzuki, Hirotoshi Toyoda and other my colleagues staying at Fermilab for their help. I also wish to thank other

members of the Tsukuba high energy physics group for their constant help. They include Kazuhiko Hara, Shigeyuki Miyashita, Itsuo Nakano and other colleagues.

I thank the Fermilab staffs and the technical staffs of the participating institutions for their vital contributions. I thank many CDF collaborators who have developed the detector and other analysis environment.

I want to express my great appreciation to Carol Picciolo, Kyoko Kunori, Mutsumi Uenishi and Kazuko Kumashiro for their help through their secretary works.

Finally and most importantly I thank my family for their constant support and encouragement.

This work was supported by the Ministry of Education, Science and Culture of Japan; the U.S. Department of Energy and National Science Foundation; the Italian Istituto Nazionale di Fisica Nucleare; the Natural Sciences and Engineering Research Council of Canada; the National Science Council of the Republic of China; and the A. P. Sloan Foundation.

Contents

List of Figures

List of Tables

The CDF Collaboration

F. Abe,[14] H. Akimoto,[32] A. Akopian,[27] M. G. Albrow,[7] S. R. Amendolia,[23] D. Amidei,[17] J. Antos,[29] C. Anway-Wiese,[4] S. Aota,[32] G. Apollinari,[27] T. Asakawa,[32] W. Ashmanskas,[15] M. Atac,[7] P. Auchincloss,[26] F. Azfar,[22] P. Azzi-Bacchetta,[21] N. Bacchetta,[21] W. Badgett,[17] S. Bagdasarov,[27] M. W. Bailey,[19] J. Bao,[35] P. de Barbaro,[26] A. Barbaro-Galtieri,[15] V. E. Barnes,[25] B. A. Barnett,[13] E. Barzi,[8] G. Bauer,[16] T. Baumann,[9] F. Bedeschi,[23] S. Behrends,[3] S. Belforte,[23] G. Bellettini,[23] J. Bellinger,[34] D. Benjamin,[31] J. Benlloch,[16] J. Bensinger,[3] D. Benton,[22] A. Beretvas,[7] J. P. Berge,[7] J. Berryhill,[5] S. Bertolucci,[8] A. Bhatti,[27] K. Biery,[12] M. Binkley,[7] D. Bisello,[21] R. E. Blair,[1] C. Blocker,[3] A. Bodek,[26] W. Bokhari,[16] V. Bolognesi,[7] D. Bortoletto,[25] J. Boudreau,[24] L. Breccia,[2] C. Bromberg,[18] N. Bruner,[19] E. Buckley-Geer,[7] H. S. Budd,[26] K. Burkett,[17] G. Busetto,[21] A. Byon-Wagner,[7] K. L. Byrum,[1] J. Cammerata,[13] C. Campagnari,[7] M. Campbell,[17] A. Caner,[7] W. Carithers,[15] D. Carlsmith,[34] A. Castro,[21] D. Cauz,[23] Y. Cen,[26] F. Cervelli,[23] H. Y. Chao,[29] J. Chapman,[17] M.-T. Cheng,[29] G. Chiarelli,[23] T. Chikamatsu,[32] C. N. Chiou,[29] L. Christofek,[11] S. Cihangir,[7] A. G. Clark,[23] M. Cobal,[23] M. Contreras,[5] J. Conway,[28] J. Cooper,[7] M. Cordelli,[8] C. Couyoumtzelis,[23] D. Crane,[1] D. Cronin-Hennessy,[6] R. Culbertson,[5] J. D. Cunningham,[3] T. Daniels,[16] F. DeJongh,[7] S. Delchamps,[7] S. Dell'Agnello,[23] M. Dell'Orso,[23] L. Demortier,[27] B. Denby,[23] M. Deninno,[2] P. F. Derwent,[17] T. Devlin,[28] M. Dickson,[26] J. R. Dittmann,[6] S. Donati,[23] J. Done,[30] T. Dorigo,[21] A. Dunn,[17] N. Eddy,[17] K. Einsweiler,[15] J. E. Elias,[7] R. Ely,[15] E. Engels, Jr.,[24] D. Errede,[11] S. Errede,[11] Q. Fan,[26] I. Fiori,[2] B. Flaugher,[7] G. W. Foster,[7] M. Franklin,[9] M. Frautschi,[31] J. Freeman,[7] J. Friedman,[16] H. Frisch,[5] T. A. Fuess,[1] Y. Fukui,[14] S. Funaki,[32] G. Gagliardi,[23] S. Galeotti,[23] M. Gallinaro,[21] M. Garcia-Sciveres,[15] A. F. Garfinkel,[25] C. Gay,[9] S. Geer,[7] D. W. Gerdes,[17] P. Giannetti,[23] N. Giokaris,[27] P. Giromini,[8] L. Gladney,[22] D. Glenzinski,[13] M. Gold,[19] J. Gonzalez,[22] A. Gordon,[9] A. T. Goshaw,[6] K. Goulianos,[27] H. Grassmann,[23] L. Groer,[28] C. Grosso-Pilcher,[5] G. Guillian,[17] R. S. Guo,[29] C. Haber,[15] E. Hafen,[16] S. R. Hahn,[7] R. Hamilton,[9] R. Handler,[34] R. M. Hans,[35] K. Hara,[32] A. D. Hardman,[25] B. Harral,[22] R. M. Harris,[7] S. A. Hauger,[6] J. Hauser,[4] C. Hawk,[28] E. Hayashi,[32] J. Heinrich,[22] K. D. Hoffman,[25] M. Hohlmann,[1,5] C. Holck,[22] R. Hollebeek,[22]

L. Holloway,[11] A. Hölscher,[12] S. Hong,[17] G. Houk,[22] P. Hu,[24] B. T. Huffman,[24] R. Hughes,[26] J. Huston,[18] J. Huth,[9] J. Hylen,[7] H. Ikeda,[32] M. Incagli,[23] J. Incandela,[7] G. Introzzi,[23] J. Iwai,[32] Y. Iwata,[10] H. Jensen,[7] U. Joshi,[7] R. W. Kadel,[15] E. Kajfasz,[7a] T. Kamon,[30] T. Kaneko,[32] K. Karr,[33] H. Kasha,[35] Y. Kato,[20] T. A. Keaffaber,[25] L. Keeble,[8] K. Kelley,[16] R. D. Kennedy,[28] R. Kephart,[7] P. Kesten,[15] D. Kestenbaum,[9] R. M. Keup,[11] H. Keutelian,[7] F. Keyvan,[4] B. Kharadia,[11] B. J. Kim,[26] D. H. Kim,[7a] H. S. Kim,[12] S. B. Kim,[17] S. H. Kim,[32] Y. K. Kim,[15] L. Kirsch,[3] P. Koehn,[26] K. Kondo,[32] J. Konigsberg,[9] S. Kopp,[5] K. Kordas,[12] W. Koska,[7] E. Kovacs,[7a] W. Kowald,[6] M. Krasberg,[17] J. Kroll,[7] M. Kruse,[25] T. Kuwabara,[32] S. E. Kuhlmann,[1] E. Kuns,[28] A. T. Laasanen,[25] N. Labanca,[23] S. Lammel,[7] J. I. Lamoureux,[3] T. LeCompte,[11] S. Leone,[23] J. D. Lewis,[7] P. Limon,[7] M. Lindgren,[4] T. M. Liss,[11] N. Lockyer,[22] O. Long,[22] C. Loomis,[28] M. Loreti,[21] J. Lu,[30] D. Lucchesi,[23] P. Lukens,[7] S. Lusin,[34] J. Lys,[15] K. Maeshima,[7] A. Maghakian,[27] P. Maksimovic,[16] M. Mangano,[23] J. Mansour,[18] M. Mariotti,[21] J. P. Marriner,[7] A. Martin,[11] J. A. J. Matthews,[19] R. Mattingly,[16] P. McIntyre,[30] P. Melese,[27] A. Menzione,[23] E. Meschi,[23] S. Metzler,[22] C. Miao,[17] G. Michail,[9] R. Miller,[18] H. Minato,[32] S. Miscetti,[8] M. Mishina,[14] H. Mitsushio,[32] T. Miyamoto,[32] S. Miyashita,[32] Y. Morita,[14] J. Mueller,[24] A. Mukherjee,[7] T. Muller,[4] P. Murat,[23] H. Nakada,[32] I. Nakano,[32] C. Nelson,[7] D. Neuberger,[4] C. Newman-Holmes,[7] M. Ninomiya,[32] L. Nodulman,[1] S. H. Oh,[6] K. E. Ohl,[35] T. Ohmoto,[10] T. Ohsugi,[10] R. Oishi,[32] M. Okabe,[32] T. Okusawa,[20] R. Oliver,[22] J. Olsen,[34] C. Pagliarone,[2] R. Paoletti,[23] V. Papadimitriou,[31] S. P. Pappas,[35] S. Park,[7] A. Parri,[8] J. Patrick,[7] G. Pauletta,[23] M. Paulini,[15] A. Perazzo,[23] L. Pescara,[21] M. D. Peters,[15] T. J. Phillips,[6] G. Piacentino,[2] M. Pillai,[26] K. T. Pitts,[7] R. Plunkett,[7] L. Pondrom,[34] J. Proudfoot,[1] F. Ptohos,[9] G. Punzi,[23] K. Ragan,[12] A. Ribon,[21] F. Rimondi,[2] L. Ristori,[23] W. J. Robertson,[6] T. Rodrigo,[7a] S. Rolli,[23] J. Romano,[5] L. Rosenson,[16] R. Roser,[11] W. K. Sakumoto,[26] D. Saltzberg,[5] A. Sansoni,[8] L. Santi,[23] H. Sato,[32] V. Scarpine,[30] P. Schlabach,[9] E. E. Schmidt,[7] M. P. Schmidt,[35] A. Scribano,[23] S. Segler,[7] S. Seidel,[19] Y. Seiya,[32] G. Sganos,[12] A. Sgolacchia,[2] M. D. Shapiro,[15] N. M. Shaw,[25] Q. Shen,[25] P. F. Shepard,[24] M. Shimojima,[32] M. Shochet,[5] J. Siegrist,[15] A. Sill,[31] P. Sinervo,[12] P. Singh,[24] J. Skarha,[13] K. Sliwa,[33] F. D. Snider,[13] T. Song,[17] J. Spalding,[7] P. Sphicas,[16] F. Spinella,[23] M. Spiropulu,[9] L. Spiegel,[7] L. Stanco,[21] J. Steele,[34] A. Stefanini,[23] K. Strahl,[12] J. Strait,[7] R. Ströhmer,[9] D. Stuart,[7] G. Sullivan,[5] A. Soumarokov,[29] K. Sumorok,[16] J. Suzuki,[32] T. Takada,[32] T. Takahashi,[20]

T. Takano,[32] K. Takikawa,[32] N. Tamura,[10] F. Tartarelli,[23] W. Taylor,[12] P. K. Teng,[29] Y. Teramoto,[20] S. Tether,[16] D. Theriot,[7] T. L. Thomas,[19] R. Thun,[17] M. Timko,[33] P. Tipton,[26] A. Titov,[27] S. Tkaczyk,[7] D. Toback,[5] K. Tollefson,[26] A. Tollestrup,[7] J. Tonnison,[25] J. F. de Troconiz,[9] S. Truitt,[17] J. Tseng,[13] N. Turini,[23] T. Uchida,[32] N. Uemura,[32] F. Ukegawa,[22] G. Unal,[22] S. C. van den Brink,[24] S. Vejcik, III,[17] G. Velev,[23] R. Vidal,[7] M. Vondracek,[11] D. Vucinic,[16] R. G. Wagner,[1] R. L. Wagner,[7] J. Wahl,[5] C. Wang,[6] C. H. Wang,[29] G. Wang,[23] J. Wang,[5] M. J. Wang,[29] Q. F. Wang,[27] A. Warburton,[12] G. Watts,[26] T. Watts,[28] R. Webb,[30] C. Wei,[6] C. Wendt,[34] H. Wenzel,[15] W. C. Wester, III,[7] A. B. Wicklund,[1] E. Wicklund,[7] R. Wilkinson,[22] H. H. Williams,[22] P. Wilson,[5] B. L. Winer,[26] D. Wolinski,[17] J. Wolinski,[18] X. Wu,[23] J. Wyss,[21] A. Yagil,[7] W. Yao,[15] K. Yasuoka,[32] Y. Ye,[12] G. P. Yeh,[7] P. Yeh,[29] M. Yin,[6] J. Yoh,[7] C. Yosef,[18] T. Yoshida,[20] D. Yovanovitch,[7] I. Yu,[35] L. Yu,[19] J. C. Yun,[7] A. Zanetti,[23] F. Zetti,[23] L. Zhang,[34] W. Zhang,[22] and S. Zucchelli[2]

(CDF Collaboration)

[1] *Argonne National Laboratory, Argonne, Illinois 60439*

[2] *Istituto Nazionale di Fisica Nucleare, University of Bologna, I-40126 Bologna, Italy*

[3] *Brandeis University, Waltham, Massachusetts 02254*

[4] *University of California at Los Angeles, Los Angeles, California 90024*

[5] *University of Chicago, Chicago, Illinois 60637*

[6] *Duke University, Durham, North Carolina 27708*

[7] *Fermi National Accelerator Laboratory, Batavia, Illinois 60510*

[8] *Laboratori Nazionali di Frascati, Istituto Nazionale di Fisica Nucleare, I-00044 Frascati, Italy*

[9] *Harvard University, Cambridge, Massachusetts 02138*

[10] *Hiroshima University, Higashi-Hiroshima 724, Japan*

[11] *University of Illinois, Urbana, Illinois 61801*

[12] *Institute of Particle Physics, McGill University, Montreal H3A 2T8, and University of Toronto, Toronto M5S 1A7, Canada*

[13] *The Johns Hopkins University, Baltimore, Maryland 21218*

[14] *National Laboratory for High Energy Physics (KEK), Tsukuba, Ibaraki 305, Japan*

[15] *Lawrence Berkeley Laboratory, Berkeley, California 94720*

[16] *Massachusetts Institute of Technology, Cambridge, Massachusetts 02139*

[17] *University of Michigan, Ann Arbor, Michigan 48109*

[18] *Michigan State University, East Lansing, Michigan 48824*

[19] *University of New Mexico, Albuquerque, New Mexico 87131*

[20] *Osaka City University, Osaka 588, Japan*

[21] *Universita di Padova, Istituto Nazionale di Fisica Nucleare, Sezione di Padova, I-35131 Padova, Italy*

[22] *University of Pennsylvania, Philadelphia, Pennsylvania 19104*

[23] *Istituto Nazionale di Fisica Nucleare, University and Scuola Normale Superiore of Pisa, I-56100 Pisa, Italy*

[24] *University of Pittsburgh, Pittsburgh, Pennsylvania 15260*

[25] *Purdue University, West Lafayette, Indiana 47907*

[26] *University of Rochester, Rochester, New York 14627*

[27] *Rockefeller University, New York, New York 10021*

[28] *Rutgers University, Piscataway, New Jersey 08854*

[29] *Academia Sinica, Taipei, Taiwan 11529, Republic of China*

[30] *Texas A&M University, College Station, Texas 77843*

[31] *Texas Tech University, Lubbock, Texas 79409*

[32] *University of Tsukuba, Tsukuba, Ibaraki 305, Japan*

[33] *Tufts University, Medford, Massachusetts 02155*

[34] *University of Wisconsin, Madison, Wisconsin 53706*

[35] *Yale University, New Haven, Connecticut 06511*

Chapter 1

Introduction

Theories for the electromagnetic and the weak interactions were combined in the Glashow-Weinberg-Salam electroweak theory [1]. The electroweak theory, together with quantum chromodynamics (QCD) (a theory for the strong interactions [2]), is commonly called as the standard model (SM).

All interactions are mediated by gauge particles in SM and their gauge structure is expressed as $SU(3)_C \times SU(2)_L \times U(1)_Y$, where $SU(3)_C$ and $SU(2)_L \times U(1)_Y$ corresponds to the QCD and the electroweak gauge, respectively.

At present, all experimental data in high energy phenomena are well-described by SM. However, the gravitational interaction is not combined, and the three forces of the electroweak, the strong, and the gravitation appear as independent entities with very different coupling strengths. In order to unify these forces, there have been many attempts to go beyond SM. New neutral gauge boson (Z') is predicted to exist in many extensions such as grand unified theories (GUTS) [3] and left-right symmetric models [4][5]. Thus, observation of the Z' boson would provide evidences for physics beyond SM. These models typically specify the strengths of the couplings of Z' to quarks and leptons. Hence, a production cross section as a function of the Z' mass is predicted in each model. On the other hand, the Z' mass values are not well predicted [6]. The Z' boson has been searched in many experiments [7][8] and astrophysical arguments [9] for many years and is yet to be observed.

In $\overline{p}p$ collisions, Z' bosons may be detected via their decays to lepton pairs. The Collider Detector at Fermilab Collaboration (CDF) reported the upper limit on the production cross section times branching ratio for a Z' decaying into an electron pair as a function of the Z' mass. A Z' mass limit was given to be 505 GeV/c^2 (95% confidence level) [10] where it was assumed that the coupling strengths of Z' to

quarks and leptons are the same as those of Z in SM. The analysis was performed for the $Z' \rightarrow e^+e^-$ channel using the data collected during the 1992-1993 Tevatron $\bar{p}p$ run. The amount of data corresponds to an integrated luminosity of 19.7 pb^{-1}.

During the 1994-1995 collider run, CDF collected data corresponding to 90 pb^{-1}, and has performed a Z' search in both dielectron and dimuon decay channels using combined data corresponding to an integrated luminosity of 110 pb^{-1} (see Appendix B).

This thesis describes a search for the Z' boson decaying into dielectrons using the data of 110 pb^{-1}. We present a 95% confidence level upper limit on the production cross section times branching ratio of Z' decaying into dielectrons using invariant mass distributions of electron pairs. Lower bounds on the Z' mass are also derived assuming the SM coupling strengths. In addition, we present Z' mass limits for several different theoretical models based on the E_6 group and for an alternative left-right model.

In the next section, we give an overview of basic ideas of the new neutral gauge boson in the E_6 models. The alternative left-right symmetric model is described in Section 1.2.

In the next chapter, we give a brief summary of the apparatus including the Tevatron collider and components of the CDF detectors which are relevant to this analysis. Selection criteria for dielectron events and a study of efficiencies are described in Chapter 3. In Chapter 4, contributions of background events and comparisons of data with expected background mass distributions are discussed. A description of the method achieving 95% confidence level limits on the Z' cross section times branching ratio and the mass limits for various models are given in Chapter 5. Finally, conclusions are given in Chapter 6.

1.1 New neutral gauge boson in E_6 model

The E_6 group is a subspace of the eight-dimensional root space of E_8, which is the exceptional group of rank 8 [11] and is spanned by eight unit vectors. The $E_8 \times E_8'$ gauge group is a good candidate of the heterotic superstring theory. Since the fermions of SM form chiral representations, where gauge bosons have different couplings to left- and right-handed fermion states, $E_8 \times E_8'$ can contain SM in its usual form. The E_8' describes a "shadow world" which interacts with ordinary matter only gravitationally. Compactification on a Calabi-Yau manifold [12] results in the

breaking:

$$E_8 \rightarrow SU(3) \times E_6 \tag{1.1}$$

The SU(3) gauge field becomes the spin connection on the compactified space. In this analysis we are concerned only with the E_6 gauge group.

The fundamental 27 representation of E_6 can be decomposed according to the SO(10) and SU(5) multiplets as

$$\mathbf{27} = (16,\bar{5}) + (16,10) + (16,1) + (10,\bar{5}) + (10,5) + (1,1), \tag{1.2}$$

and the decompositions are shown in Table 1.1. In addition to the usual fermions

SO(10)	SU(5)	Left-handed state	color	I_3	Y	Q
16	10	u	3	1/2	1/3	2/3
		d	3	−1/2	1/3	−1/3
		$\overline{u}$	$\overline{3}$	0	−4/3	−2/3
		e^+	1	0	2	1
	$\overline{5}$	$\overline{d}$	$\overline{3}$	0	2/3	1/3
		ν_e	1	1/2	−1	0
		e^-	1	−1/2	−1	−1
	1	$\overline{\nu}_e$	1	0	0	0
10	$\overline{5}$	$\overline{h}$	$\overline{3}$	0	2/3	1/3
		E^-	1	−1/2	−1	−1
		ν_E	1	1/2	−1	0
	5	h	3	0	−2/3	−1/3
		E^+	1	1/2	1	1
		$\overline{N}_E$	1	−1/2	1	0
1	1	n	1	0	0	0

Table 1.1: Quantum numbers of the fermions in the 27 presentation of E_6.

u, d, ν_e and e^-, there is a charge $-\frac{1}{3}$ quark isosinglet h, charged leptons E^-, and neutral leptons ν_E, N_E and n.

The following breakdown of E_6 is one of the patterns discussed frequently:

$$E_6 \rightarrow SO(10) \times U(1)_\psi \rightarrow SU(5) \times U(1)_\chi \times U(1)_\psi, \tag{1.3}$$

where SU(5) contains the standard $SU(3)_C \times SU(2)_L \times U(1)_Y$. Additional $U(1)_\psi$ and $U(1)_\chi$ groups lead to new neutral gauge bosons, Z_ψ and Z_χ, with flavor diagonal couplings. Physically observable states of the bosons can be expressed as a linear combination of Z_ψ and Z_χ with a mixing angle θ:

$$\begin{aligned} Z'(\theta) &\equiv \cos\theta \cdot Z_\psi - \sin\theta \cdot Z_\chi, \\ Z''(\theta) &\equiv \cos\theta \cdot Z_\chi + \sin\theta \cdot Z_\psi. \end{aligned} \tag{1.4}$$

Certain values of the angle θ give rise to theoretically interesting cases. Some of the cases include [4]:

- Model ψ
  $E_6 \rightarrow SO(10) \times U(1)_\psi$
  $Z' = Z_\psi \quad \text{for} \quad \theta = 0$

- Model χ
  $SO(10) \rightarrow SU(5) \times U(1)_\chi$
  $Z' = Z_\chi \quad \text{for} \quad \theta = -\pi/2$

- Model η
  $E_6 \rightarrow SU(3)_C \times SU(2)_L \times U(1)_Y \times U(1)_\eta$
  $Z' = Z_\eta \quad \text{for} \quad \theta = \sin^{-1}\sqrt{3/8}$

- Model I
  $E_6 \rightarrow SU(3)_C \times SU(2)_L \times U(1)_Y \times SU(2)_I \times U(1)'$
  $Z' = Z_I \quad \text{for} \quad \theta = \sin^{-1}\sqrt{5/8}$

The new neutral gauge bosons $Z_{\psi,\chi,\eta,I}$ are most frequently discussed in low-energy E_6 models.

The neutral-current Lagrangian for Z' in the E_6 models at low energy can be written:

$$\mathcal{L} = g\bar{f}\gamma_\mu(v'_f - a'_f\gamma_5)fZ'^\mu \tag{1.5}$$

The coupling factors, v'_f and a'_f, can be calculated once the charge for the extra U(1) is specified. Neglecting QCD radiative corrections, the width to a fermion pair is given by

$$\Gamma(Z' \rightarrow \bar{f}f) = C_f\left(\frac{g^2 M_{Z'}}{12\pi}\right)\left(1 - \frac{4m_f^2}{M_{Z'}^2}\right)^{\frac{1}{2}} \left[v'^2_f\left(1 + \frac{2m_f^2}{M_{Z'}^2}\right) + a'^2_f\left(1 - \frac{4m_f^2}{M_{Z'}^2}\right) \right] \tag{1.6}$$

where C_f is a color factor ($C_f = 3$ for quarks, $= 1$ for leptons). For the case that fermions are only (or by far dominant) contributions to the Z' width, $\Gamma_{Z'}/M_{Z'}$ is calculated by Barger *et al.* [13] as a function of $\cos\theta$ as shown in Figure 1.1 (a), where the mixing angle θ is labeled as α and n_g represents the number of exotics generations contributing to the Z' width. With an assumption of $m_f/M_{Z'} \ll 1$, the width can be written as

$$\Gamma(Z' \to \bar{f}f) = C_f(\frac{g^2 M_{Z'}}{12\pi})\left(v_f'^2 + a_f'^2\right). \tag{1.7}$$

As we will discuss in the later section (5.2.3), the Z' width may affect our limits on the production cross section since the limits are obtained by the Z' mass distributions. For narrower widths we obtain more stringent limits on the cross section. Here, we note that for all values of the mixing angle θ, $\Gamma^{tot}_{Z'}/M_{Z'}$ is far smaller than the one expected by scaling up the same ratio for the SM Z boson, where the partial width of Z to a fermion pair is given by

$$\Gamma(Z \to \bar{f}f) = C_f(\frac{g_Z^2 M_Z}{12\pi})\left(v_f^2 + a_f^2\right), \tag{1.8}$$

with g_Z being the coupling constant of $\mathrm{SU}(2)_L$ and defined by

$$g_Z \sin\theta_W = e. \tag{1.9}$$

The differential cross section for $q\bar{q} \to l^+l^- + X$ can be written as

$$\frac{d\sigma}{d\cos\theta^*} = \frac{\pi\alpha^2}{8m^2}\left[S_q(1+\cos^2\theta^*) + 2A_q\cos\theta^*\right], \tag{1.10}$$

where θ^* is the l^+l^- center-of-mass scattering angle, m is the lepton-pair mass. The factors S_q and A_q are given by

$$\begin{aligned} S_q &= \sum_{i,j}\left(\frac{g_i}{e}\right)^2\left(\frac{g_j}{e}\right)^2 m^4 P^{ss}_{ij}(C^q_{L_i}C^q_{L_j} + C^q_{R_i}C^q_{R_j})(C^l_{L_i}C^l_{L_j} + C^l_{R_i}C^l_{R_j}), \\ A_q &= \sum_{i,j}\left(\frac{g_i}{e}\right)^2\left(\frac{g_j}{e}\right)^2 m^4 P^{ss}_{ij}(C^q_{L_i}C^q_{L_j} - C^q_{R_i}C^q_{R_j})(C^l_{L_i}C^l_{L_j} - C^l_{R_i}C^l_{R_j}), \end{aligned} \tag{1.11}$$

where g_i is the coupling strengths for the i-th gauge boson and

$$P^{ss}_{ij} \equiv \frac{(s-M_i^2)(s-M_j^2) + (\Gamma_i M_i)(\Gamma_j M_j)}{\left[(s-M_i^2)^2 + (\Gamma_i M_i)^2\right]\left[(s-M_j^2)^2 + (\Gamma_j M_j)^2\right]} \tag{1.12}$$

with $M_i(\Gamma_i)$ being the mass(width) of the i-th gauge boson. The terms of C_{L_i} and C_{R_i} are the couplings of the i-th neutral gauge bosons to the fermions q and l, which can be written as

$$C_L^f \equiv C_R^f \equiv eQ_f \quad \text{for } \gamma, \tag{1.13}$$

$$C_{L,R}^f \equiv \frac{g}{\cos\theta_W}\left[\left(v_f\cos\theta_3 - v_f'\sin\theta_3\right) \pm \left(a_f\cos\theta_3 - a_f'\sin\theta_3\right)\right] \quad \text{for } Z, \tag{1.14}$$

$$C_{L,R}^f \equiv \frac{g}{\cos\theta_W}\left[\left(v_f'\cos\theta_3 + v_f\sin\theta_3\right) \pm \left(a_f'\cos\theta_3 + a_f\sin\theta_3\right)\right] \quad \text{for } Z', \tag{1.15}$$

where the signs $\pm$ correspond to L, R, and θ_3 is the mixing angle of Z-Z'. This mixing is expected to be negligible small ($|\sin\theta_3| < 0.01$) by LEP results [14]. The production cross section of Z' is shown as a function of the Z' mass in Figure 1.2.

Another sub-case of the E_6 gauge group discussed frequently is the left-right symmetric model (LR) [15]:

$$E_6 \rightarrow SU(3)_C \times SU(2)_L \times SU(2)_R \times U(1)_L \times U(1)_R\,, \tag{1.16}$$

where $U(1)_L \times U(1)_R$ can be written as

$$U(1)_L \times U(1)_R \rightarrow U(1)_{V=L+R}\,. \tag{1.17}$$

The $SU(2)_L \times SU(2)_R \times U(1)_V$ leads to 3 gauge bosons, $W_R^{\pm}$ and Z_R in addition to the $W_L^{\pm}$, Z_L bosons and the photon. Assuming that the left and right gauge coupling constants would be the same, $g_L = g_R = g$, relations between the masses of the neutral and charged gauge bosons are written:

$$M_{Z_L} = \frac{M_{W_L}}{\cos\theta},$$

$$M_{Z_R} = \frac{M_{W_R}\cos\theta}{\sqrt{\cos 2\theta}}, \tag{1.18}$$

where the angle θ is defined by

$$\sin^2\theta \equiv \frac{g'^2}{g^2 + 2g'^2} \tag{1.19}$$

with $g' \equiv g\tan\theta_W$.

In the limit of the large mass of W_R^+ and with identification $\sin\theta = \sin\theta_W$, the left-right symmetric gauge theory predicts all the lowest-order neutral current interactions to be exactly the same as in the Weinberg-Salam theory (WS). In addition, the same masses for the left-handed gauge bosons are also predicted as follows:

$$M_{W_L}(LR) = M_{W_L}(WS),$$
$$M_{Z_L}(LR) = M_{Z_L}(WS). \tag{1.20}$$

The production cross section of $Z_R \to e^+e^-$ for the Tevatron $\bar{p}p$ experiments ($\sqrt{s}$ = 1.8 TeV) was calculated by F. Feruglio *et al.* [16] as shown in Table 1.2. They also calculated the branching ratio to dileptons as

$$Br(Z_R \to e^+e^- + X) = Br(Z_R \to \mu^+\mu^- + X) \simeq 6 \times 10^{-4}. \tag{1.21}$$

M_R (GeV)	Inclusive production cross section (pb^{-1})
300	84
500	6.9
700	0.7

Table 1.2: Predicted inclusive production cross sections in $\bar{p}p$ collisions at $\sqrt{s}$ = 1.8 TeV.

1.2 New neutral gauge boson in the alternative left-right symmetric model

The alternative left-right symmetric model (ALRM) which was proposed by Ernest Ma [17] is one of the $SU(2)_L \times SU(2)_R \times U(1)_V$ gauge groups, where the interactions by the $SU(2)_R$ gauge are introduced differently from those in LR. The width to a fermion pair in ALRM is given by

$$\Gamma(Z' \to \bar{f}f)$$
$$= C_f \left(\frac{g_Z^2 M_{Z'}}{24\pi}\right)\left(1 - \frac{4m_f^2}{M_{Z'^2}}\right)^{\frac{1}{2}}\left[\left(A_L^2 + A_R^2\right)\left(1 - \frac{m_f^2}{M_{Z'^2}}\right) + 6A_L A_R \frac{m_f^2}{M_{Z'^2}}\right], \tag{1.22}$$

where

$$A_L = -Q_L \sin\theta + Q'_L\sqrt{x_W}\cos\theta, \tag{1.23}$$

$$A_R = -Q_R \sin\theta + Q'_R\sqrt{x_W}\cos\theta, \tag{1.24}$$

with θ being the mixing angle of Z-Z' and $Q_L(Q'_L)$ and $Q_R(Q'_R)$ being the fermion charges for $Z(Z')$ given in Table 1.1. The total fermionic width of Z' is given by

$$\Gamma(Z' \rightarrow \text{fermions}) = (1.9 + 0.6 \cdot n_g) \times \left(\frac{M_Z}{M_{Z'}}\right) \quad \left[\text{GeV}\right]. \tag{1.25}$$

For $n_g = 0$, the ratio of $\Gamma_{Z'}/M_{Z'}$ is less than what would be expected by scaling up the same ratio for the SM Z boson which has been measured to be 2.49 GeV/c^2 [18]. This result also gives us conservative limits on the Z' mass.

Figure 1.3 from Barger and Whisnant [19] shows the predicted production cross section for Z' in ALRM for $\bar{p}p$ collisions at $\sqrt{s} = 2$ TeV.

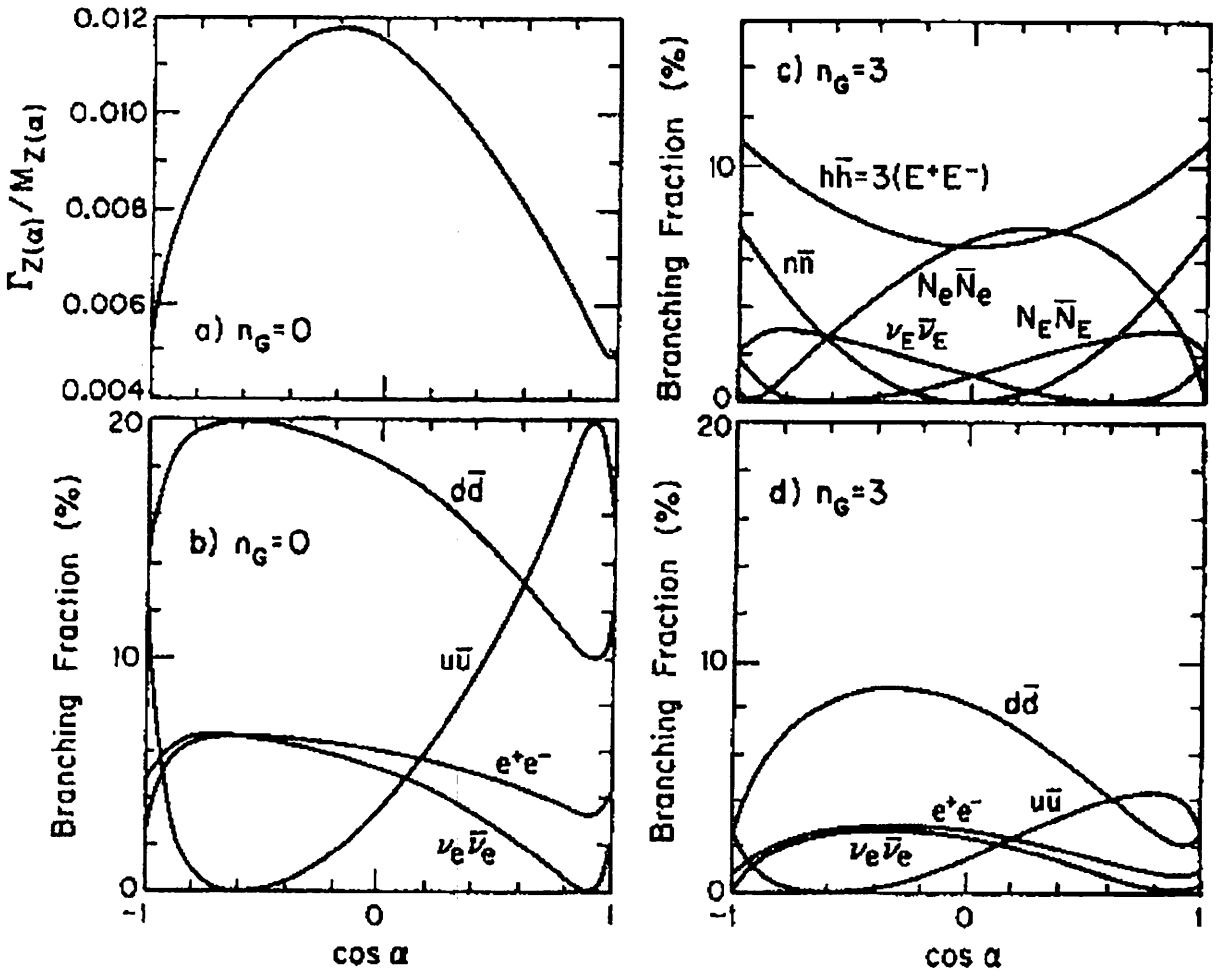

Figure 1.1: Figure (a) shows $\Gamma_{Z'(\theta)}/M_{Z'(\theta)}$ as a function of $\cos\alpha$(i.e., $\cos\theta$), for $n_g = 0$. Branching fractions for the Z' decays to known fermions as a function of $\cos\alpha$ are shown in (b) for $n_g = 0$ and (d) for $n_g = 3$. Figure (c) shows the branching fractions to exotic fermions for $n_g = 3$.

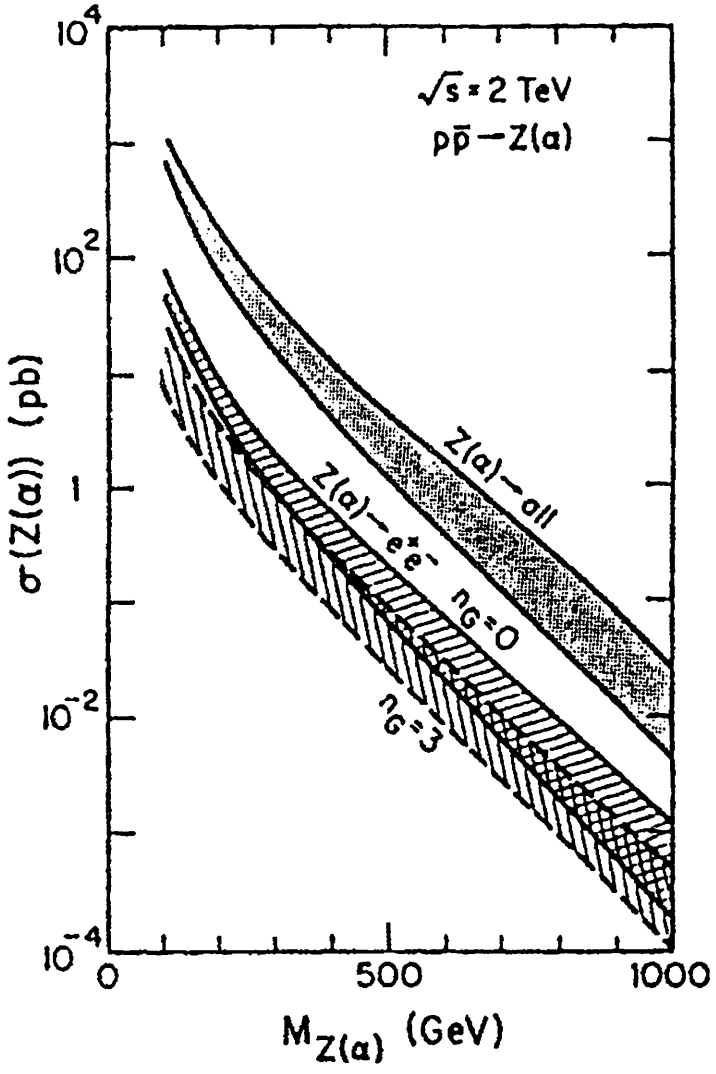

Figure 1.2: Predicted production cross section for Z' in the E_6 models for $\overline{p}p$ collisions at $\sqrt{s} = 2$ TeV [13].

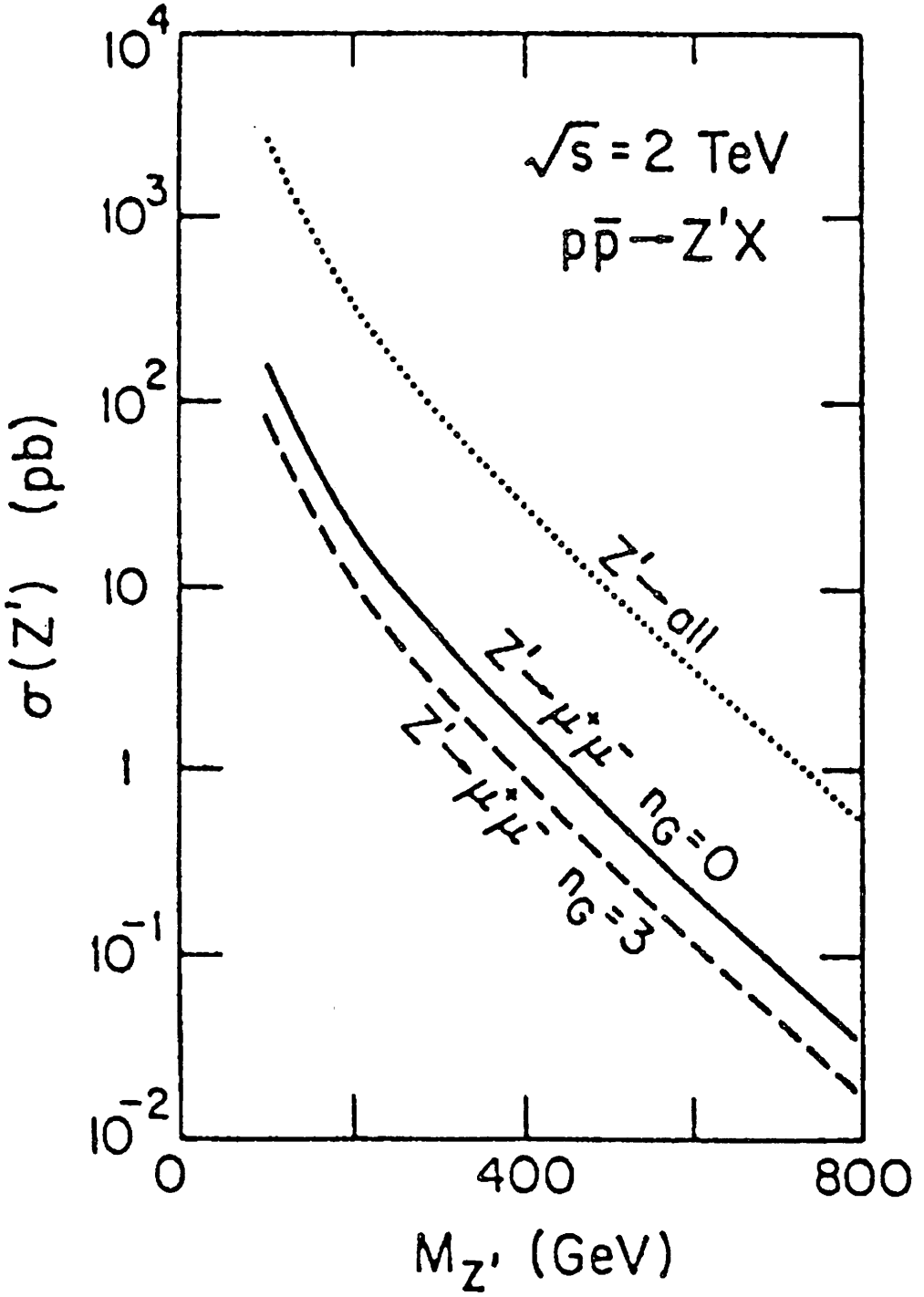

Figure 1.3: Predicted production cross section for Z' in ALRM for $\bar{p}p$ collisions at $\sqrt{s} = 2$ TeV.

Chapter 2

Apparatus

This experiment is performed at the Fermi National Accelerator Laboratory (Fermilab) in Batavia, Illinois, U.S.A. using the Tevatron accelerator which gives proton-antiproton collisions at a center-of-mass energy of 1.8 TeV. Particles which are produced by the collisions are detected by the Collider Detector at Fermilab (CDF). The Tevatron collider and the CDF detector are described below emphasizing what we used in our analysis.

2.1 Tevatron $\bar{p}p$ collider

The Tevatron $\bar{p}p$ collider complex consists of five stage accelerators as illustrated in Figure 2.1. In the first stage, negatively charged hydrogen ions are accelerated to 750 keV by a large DC voltage accelerator (Cockroft-Walton electrostatic accelerator). In the Linac, a 150-meter-long linear accelerator, these particles are accelerated to 400 MeV. The two electrons are then stripped off the hydrogen ions, leaving bare protons, which are injected into the Booster, a synchrotron with a diameter of approximately 150 meters, located in a tunnel 6 meters below the ground. Once the protons are accelerated by the Booster to 8 GeV, they are injected into the Main ring. The Main ring, a synchrotron with a diameter of 2 kilometers, is composed of water-cooled magnets operated at room temperature. The protons are accelerated by the Main ring to 150 GeV and injected into the Tevatron ring. The Tevatron is a synchrotron with a diameter of 2 kilometers and consists of superconducting magnets cooled by liquid helium. The protons are finally accelerated to 900 GeV in the Tevatron.

Protons in the Main ring are also used to initiate production of antiprotons.

The protons are accelerated to 120 GeV and then directed to a tungsten target and produce antiprotons. The antiprotons are collected in the Debuncher ring. The captured beam of antiprotons, circulating in the Debuncher ring is then made more dense by a process called stochastic cooling. The antiprotons are then transferred to the Accumulator ring, where the antiprotons are merged into a single beam cooled further, and stored. the Debuncher and Accumulator rings are operated at 8 GeV, the same energy as the Booster. The antiprotons are injected into the Main ring and then accelerated to 150 GeV and to 900 GeV by the Tevatron.

Major achievements of the Tevatron are not only the beam energy, but also its luminosity. The product of luminosity and cross section gives the number of events produced:

$$N = \mathcal{L} \cdot \sigma \tag{2.1}$$

If we aim at a rare event, high luminosity is necessary to observe it. The luminosity $\mathcal{L}$ is written down as follows.

$$\mathcal{L} = \frac{N_p N_{\bar{p}} f B}{4\pi \epsilon \beta} \tag{2.2}$$

A large number of particles in a bunch or small beam size provides a large luminosity.

			typical value
N_p	:	number of protons per bunch	1×10^{11}
$N_{\bar{p}}$	:	number of antiprotons per bunch	7×10^{10}
f	:	revolution frequency (kHz)	50
B	:	number of bunches	6
ϵ	:	emittance (mm mrad)	2.6×10^{-3}
β	:	betatron oscillation length (m)	0.5

The Tevatron provided an instantaneous luminosity of $\mathcal{L} \sim 1 \times 10^{31}$ cm^{-2}s^{-1} during the period of 1992-1995 run. An integrated luminosity of 110 pb^{-1} has been collected by the CDF.

2.2 CDF Detector

The Collider Detector at Fermilab (CDF) is a general purpose detector designed to study the physics of high energy $\bar{p}p$ collisions. Many publications give detailed descriptions of the various components of the CDF detector [20]. It has

both azimuthal and forward-backward symmetry. A cutaway view of CDF is shown in Figures 2.2. The polar angle (θ) in spherical coordinates is measured from the proton beam axis, and the azimuthal angle (ϕ) from the plane of the Tevatron. The tracking systems in the CDF detector consist of the silicon vertex detector (SVX), the vertex tracking chamber (VTX) and the central tracking chamber (CTC). The CDF detector can be divided into three regions by η, Central region ($|\eta| < 1.1$), Plug region ($1.1 < |\eta| < 2.4$) and Forward/Backward region ($2.2 < |\eta| < 4.2$), where η is the pseudorapidity defined by ($\eta \equiv -\ln \tan(\theta/2)$).

In the Central region, there are the central electromagnetic calorimeter (CEM), the central electromagnetic strip chamber (CES) and the central hadron calorimeter (CHA). In the plug region, calorimeters consist plug electromagnetic calorimeter (PEM) and the plug hadron calorimeter (PHA). The CTC and calorimeters in the central and the plug regions are used in this analysis. In this section, we briefly summarize CDF detector components which are used in this analysis.

2.2.1 Tracking Chambers

VTX

The VTX provides a $\bar{p}p$ collision point in z coordinate along the proton beam line. The VTX is made up of eight octagonal modules with sense wires running perpendicular to the beam line. The VTX covers $|\eta| < 3.25$ and 280 cm in z. The VTX is able to measure the z of the interaction point with a resolution of 1 mm, while the ϕ resolution is limited to knowing which octant the track traversed. Thus using it for a charge determination and measurement of the momentum is impossible.

CTC

The CTC is a large multi-wire drift chamber in a 1.41 Tesla solenoidal magnetic field. It consists of 84 layers of sense wires arranged into nine "superlayers". Four of the superlayers have their wires at an angle, $\pm 3°$, for reconstruction in the r-z view. The most important feature of the CTC is its ability to measure high transverse momentum (P_T) isolated tracks which are critical to measurements of high P_T leptons. The transverse momentum (P_T) is defined by

$$P_T \equiv P \sin\theta, \tag{2.3}$$

where P is the observed momentum and θ is polar angle of the track. The momentum resolution of the CTC is $\delta P_T/P_T = 0.002 \times P_T$ in GeV/c and the z resolution is 4 mm. Figure 2.3 shows the pattern drilled into the endplate; the superlayers (five axial and four stereo) are clearly visible.
The properties of three tracking chambers are summarized in Table 2.1.

	Silicon vertex detector (SVX)	Vertex tracking chamber (VTX)	Central tracking chamber (CTC)
Polar angle coverage	$\|\eta\| < 1.0$	$\|\eta\| < 3.25$	$\|\eta\| < 1.5$
Inner, outer radii (cm)	2.7,7.9	8,22	30.9,132.0
Length (cm)	26	280	320
Layers	4	24	60 axial 24 stereo
Spatial resolution	15 μm $(r-\phi)$	200-500 μm $(r-z)$	200 μm $(r-\phi)$ 4 mm $(r-z)$
Momentum resolution	$\delta P_T/P_T = 0.001 \times P_T$[†]	-	$\delta P_T/P_T = 0.002 \times P_T$
Thickness ($\theta = 90°$)	$\approx 0.035 X_0$	$\approx 0.045 X_0$	$\approx 0.015 X_0$

[†] With both CTC and SVX hits incorporated into track fit.

Table 2.1: Description of the charged particle tracking chambers

2.2.2 Calorimetry

The active sampling medium of the CDF calorimeters is either scintillator in the central region ($|\eta| < 1.1$), or gas proportional chambers in the plug ($1.1 < |\eta| < 2.4$) and forward/backward ($2.4 < |\eta| < 4.2$) regions.

CEM

The CEM is a 31 layer lead-scintillator-type sampling calorimeter with wavelength shifter to measure energy. It consists of a series of wedges, each covering 15° in ϕ and containing an electromagnetic (CEM) section followed by a hadronic section (CHA). Each of wedges is divided into ten projective towers, each covering 0.1

units in $\Delta\eta$. The coverage region of the CEM is $|\eta|$ <1.1 and full 2π in azimuth. The energy resolution is $13.7\%/\sqrt{E_T} \oplus 2\%$, where E_T is the transverse energy defined by

$$E_T \equiv E \sin\theta, \tag{2.4}$$

with the observed energy (E) and polar angle (θ). Figure 2.4 shows the anatomy of an individual central calorimeter wedge.

CES

The central electromagnetic strip chambers (CES) are embedded at shower maximum position in the wedges of the CEM. The CES measures EM shower position and transverse development by measuring of the charge deposition on orthogonal strips and wires. The location of the CES is shown in Figure 2.4 and a schematic view of the CES is shown in Figure 2.5.

CHA and WHA

The CHA covers the full 2π azimuthal range and $|\eta| < 0.9$. The CHA is located outside of the CEM and it consists of 48 steel-scintillator modules each. To fill the gap between the CHA and PHA, the WHA covers the region $0.7 < |\eta| < 1.3$. Like the CHA, WHA consists of 48 steel-scintillator modules each. The energy resolutions of the CHA and the WHA are $50\%/\sqrt{E_T} \oplus 3\%$ and $75\%/\sqrt{E} \oplus 4\%$, respectively.

PEM

The PEM is located 1.73 m in z from the nominal interaction point and covers $1.1 < |\eta| < 2.4$. It consists of 4 quadrants on each end, each quadrant consists of 34 layers of proportional tubes sandwiched between lead plates. Figure 2.6 shows an exploded view of such a layer. The energy resolution of the PEM is $22\%/\sqrt{E} \oplus 2\%$. Near shower maximum position in the PEM, a layer with finer-spaced strips (PES) provides shower profile and precise position determination.

PHA

The PEM is directly followed by the PHA. The PHA also employs gas proportional tubes. The radiator of the PHA is steel. The covering region of the PHA is $1.3 < |\eta| < 2.4$. The resolution is $106\%/\sqrt{E} \oplus 6\%$.

System	η range	Energy resolution	Thickness
CEM	$\lvert\eta\rvert < 1.1$	$13.7\%/\sqrt{E_T} \oplus 2\%$	$18X_0$
PEM	$1.1 < \lvert\eta\rvert < 2.4$	$22\%/\sqrt{E} \oplus 2\%$	$18\text{-}21X_0$
FEM	$2.2 < \lvert\eta\rvert < 4.2$	$26\%/\sqrt{E} \oplus 2\%$	$25X_0$
CHA	$\lvert\eta\rvert < 0.9$	$50\%/\sqrt{E_T} \oplus 3\%$	$4.5\lambda_0$
WHA	$0.7 < \lvert\eta\rvert < 1.3$	$75\%/\sqrt{E} \oplus 4\%$	$4.5\lambda_0$
PHA	$1.3 < \lvert\eta\rvert < 2.4$	$106\%/\sqrt{E} \oplus 6\%$	$5.7\lambda_0$
FHA	$2.4 < \lvert\eta\rvert < 4.2$	$137\%/\sqrt{E} \oplus 3\%$	$7.7\lambda_0$

Table 2.2: Summary of CDF calorimeter properties. The CDF calorimetry is divided into EM (xEM) and hadronic (xHA) detectors, which together cover all ϕ and $|\eta| < 4.2$. Thicknesses are given in radiation lengths (X_0) and interaction lengths (λ_0) for the electromagnetic and hadronic calorimeters, respectively.

2.2.3 Beam-Beam counter

Beam-Beam counters (BBC) are mounted on the front face of each far-forward/backward EM shower counters. Each BBC consists of an array of 16 scintillator plates and 16 photomultiplier tubes that encircle the 360° around the beam pipe and covers the pseudorapidity range $3.24 < |\eta| < 5.90$. At the 1992-1993 run and a part of the 1994-1995 run whose instantaneous luminosities were low, a coincidence of at least one hit in each plane of the BBC is required to initiate the trigger system, while the BBC coincidence was not required at higher instantaneous luminosities since the mean number of $\bar{p}p$ interactions per crossing of p and $\bar{p}$ bunches is sufficiently high.

2.2.4 Luminosity measurement

The luminosity can be obtained by counting the rate of a certain process of which cross section is known. We use inelastic and elastic $\bar{p}p$ events, and the BBC's to detect them. That is,

$$\mathcal{L}_{BBC} = \frac{R_{BBC}}{\sigma_{BBC}}, \tag{2.5}$$

where $\mathcal{L}_{BBC}$ is the luminosity, R_{BBC} is the BBC event rate, and σ_{BBC} is the effective cross section of visible to the BBC's. The luminosity is corrected for multiple

interaction by

$$\mathcal{L} = \frac{-\ln(1 - \mathcal{L}_{BBC})}{\sigma_{BBC}/\mathcal{F}}, \tag{2.6}$$

where $\mathcal{F}$ is the crossing frequency (=300 kHz).

The effective cross section is obtained by the luminosity-independent method [21]. The value of σ_{BBC} can be expressed as

$$\sigma_{BBC} = \sigma_{tot} \cdot \frac{R_{BBC}}{R_{tot}}, \tag{2.7}$$

where σ_{tot} is the $\bar{p}p$ total cross section at $\sqrt{s} = 1.8\,\text{TeV}$, R_{tot} is the sum of the elastic and inelastic event rates. With recent direct measurements of the elastic and total cross sections by CDF Collaboration [22], the BBC cross section was obtained as

$$\sigma_{BBC} = 51.2 \pm 1.7 \text{ mb}. \tag{2.8}$$

After accounting for possible backgrounds in the BBC's, we obtain

$$\int \mathcal{L}\, dt = 110 \pm 9 \text{ pb}^{-1}, \tag{2.9}$$

where the systematic uncertainty associated with the luminosity measurement is conservatively estimated to be 8% [23].

2.2.5 Trigger system

The CDF employs a three-level trigger system. The lowest trigger (level 1) required that there be a tower in the calorimeter over a modest threshold (or coincidence of hits in two of four chambers), which rejects the majority of uninteresting events. At typical luminosities this trigger had an accept rate of $\sim$ 5 kHz. The level 2 trigger is a Fastbus based hardware trigger system. At this level, unlike level 1, clusters of energy are formed by the hardware "cluster finder", and tracks are reconstructed by the Central Fast Tracker (CFT). The 5 kHz input rate is reduced to about 50 Hz, and these passed on to the third level trigger (level 3). The level 3 trigger was a software trigger running on UNIX machines (48 nodes, 96 buffers), on which events were being processed in parallel. The software run was essentially the complete offline reconstruction code. The majority of the CPU time used in the level 3 trigger was taken up by the track reconstruction. The output from the level 3 was written to 8mm tapes at about 10 Hz. A subset of the events was flagged in the level 3 trigger and written on a disk as a separate file for immediate offline processing. These events were used in this analysis after re-processing with the final database constants.

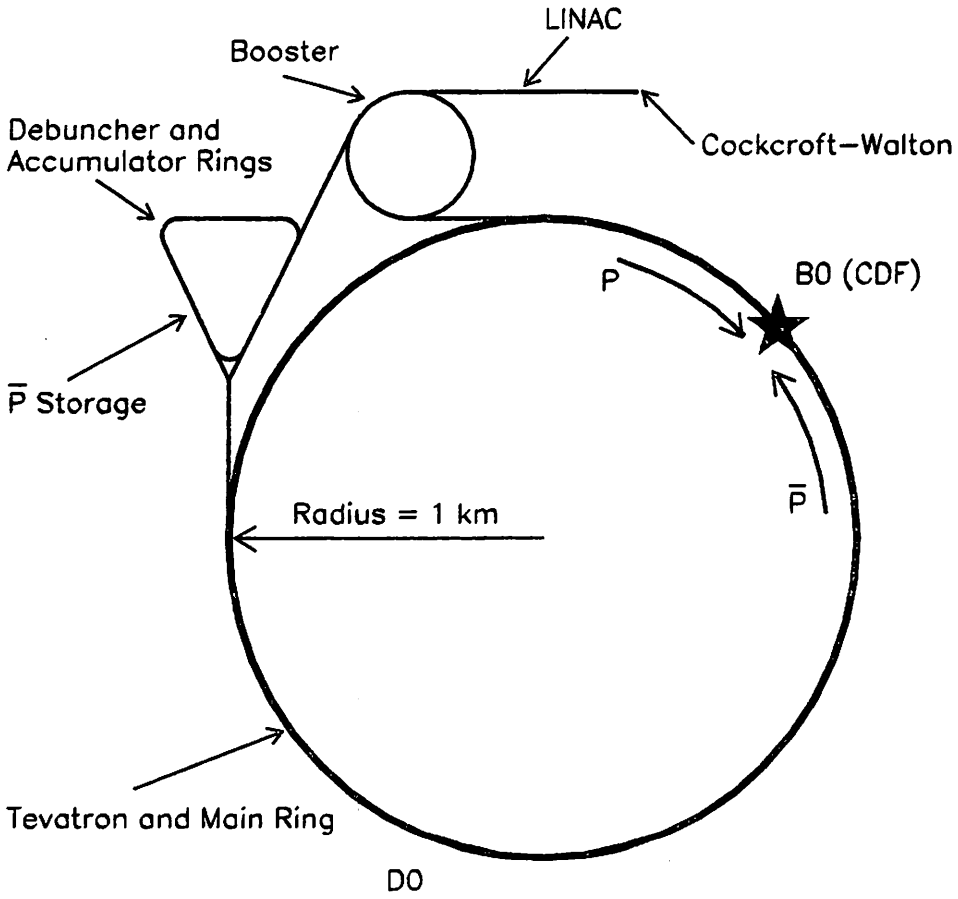

Figure 2.1: The perspective view of the Tevatron Proton-Antiproton Collider at Fermi National Accelerator Laboratory.

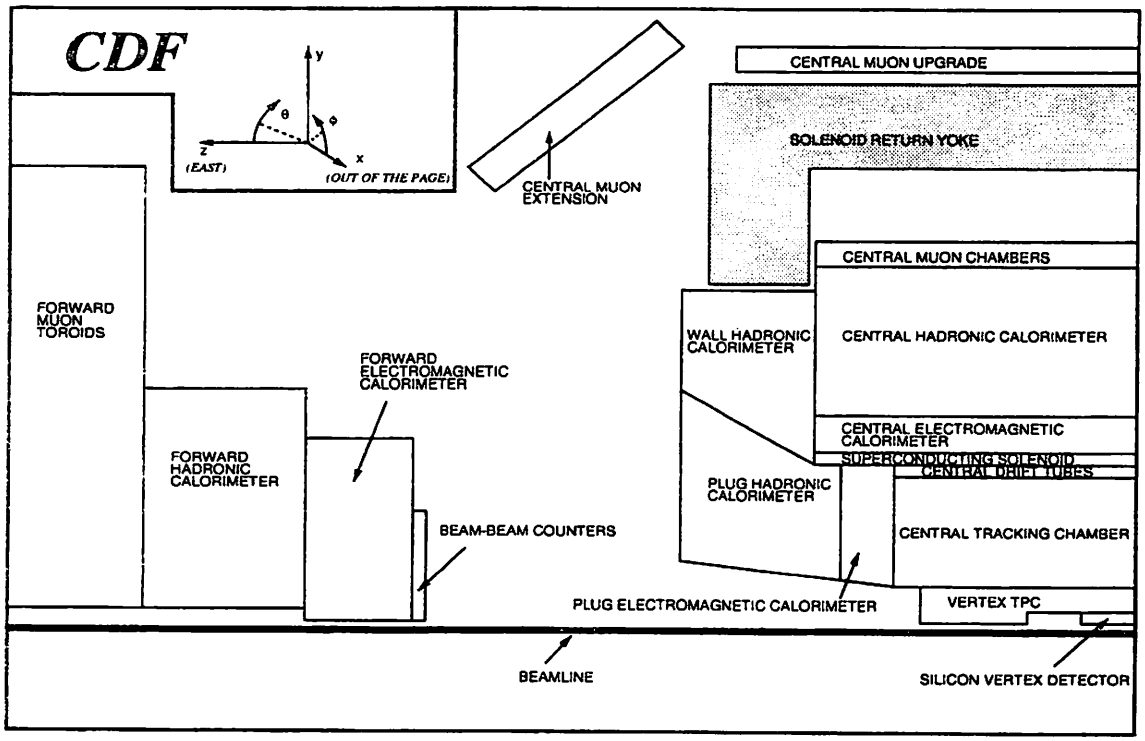

Figure 2.2: Perspective view of the Collider Detector at Fermilab.

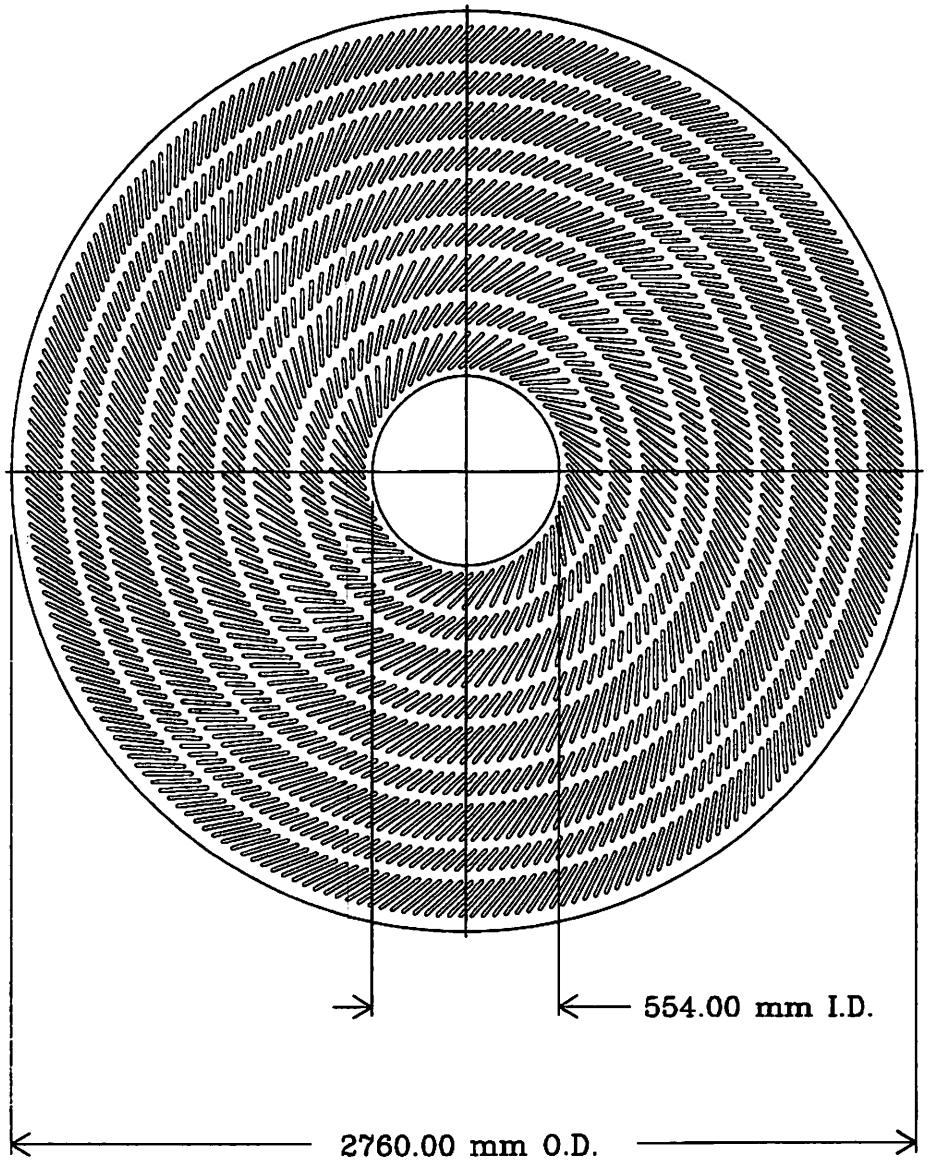

Figure 2.3: The central tracking chamber.

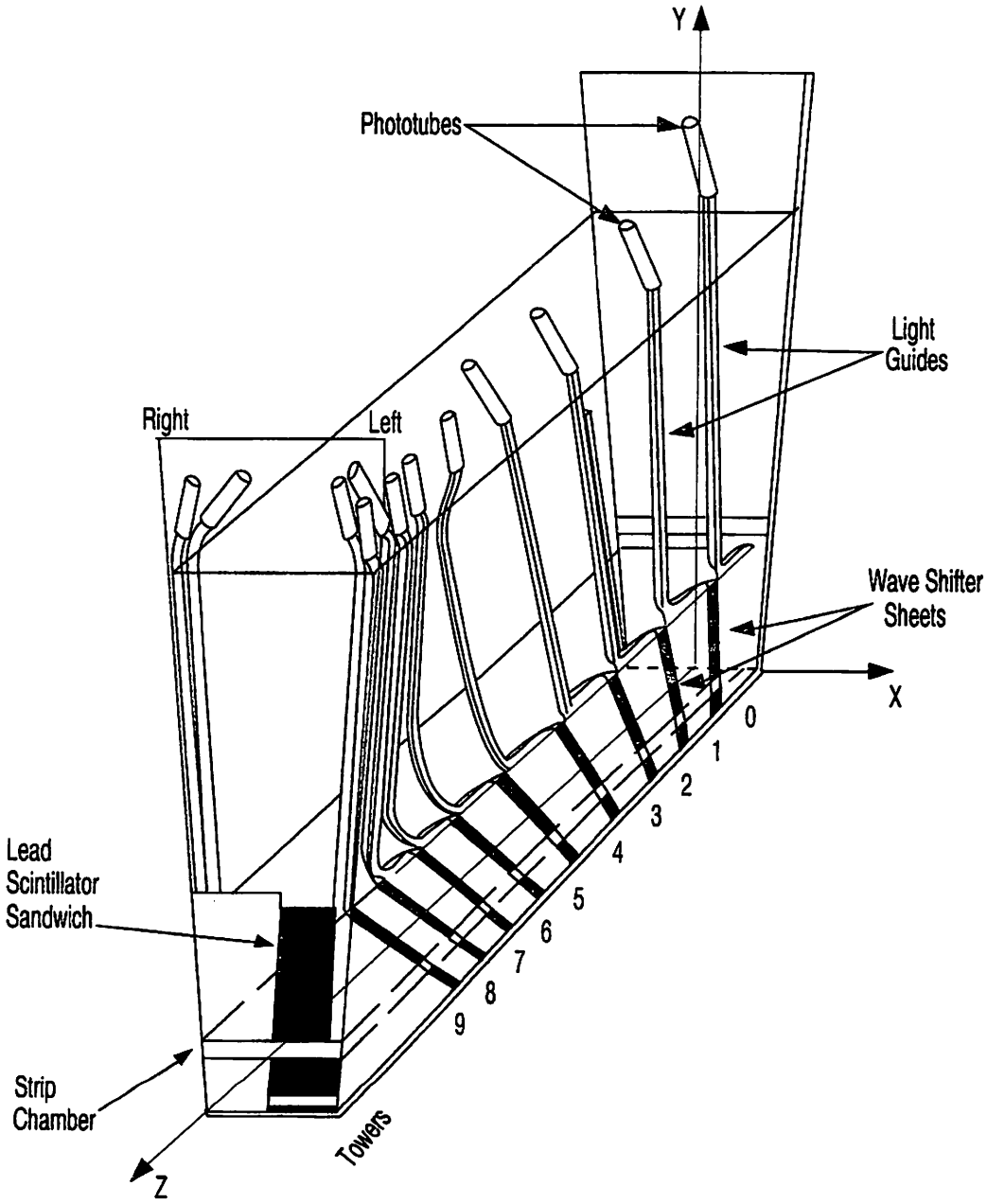

Figure 2.4: The central EM calorimeter wedge. It is followed by the hadronic compartment. The EM compartment contains a strip-wire proportional chamber.

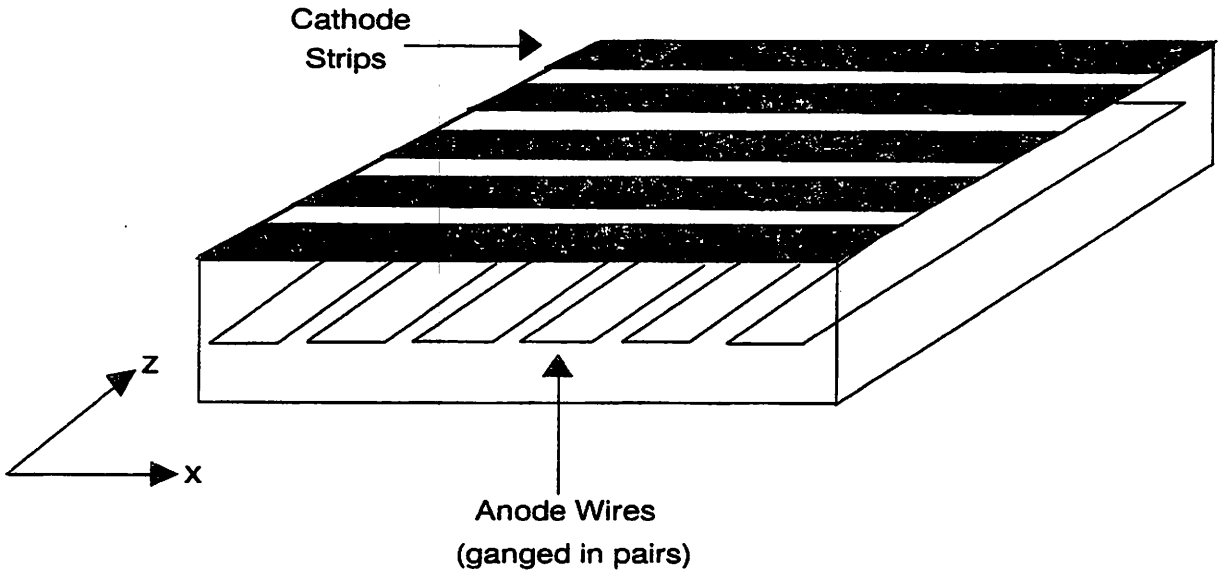

Figure 2.5: Schematic view of a CES detector.

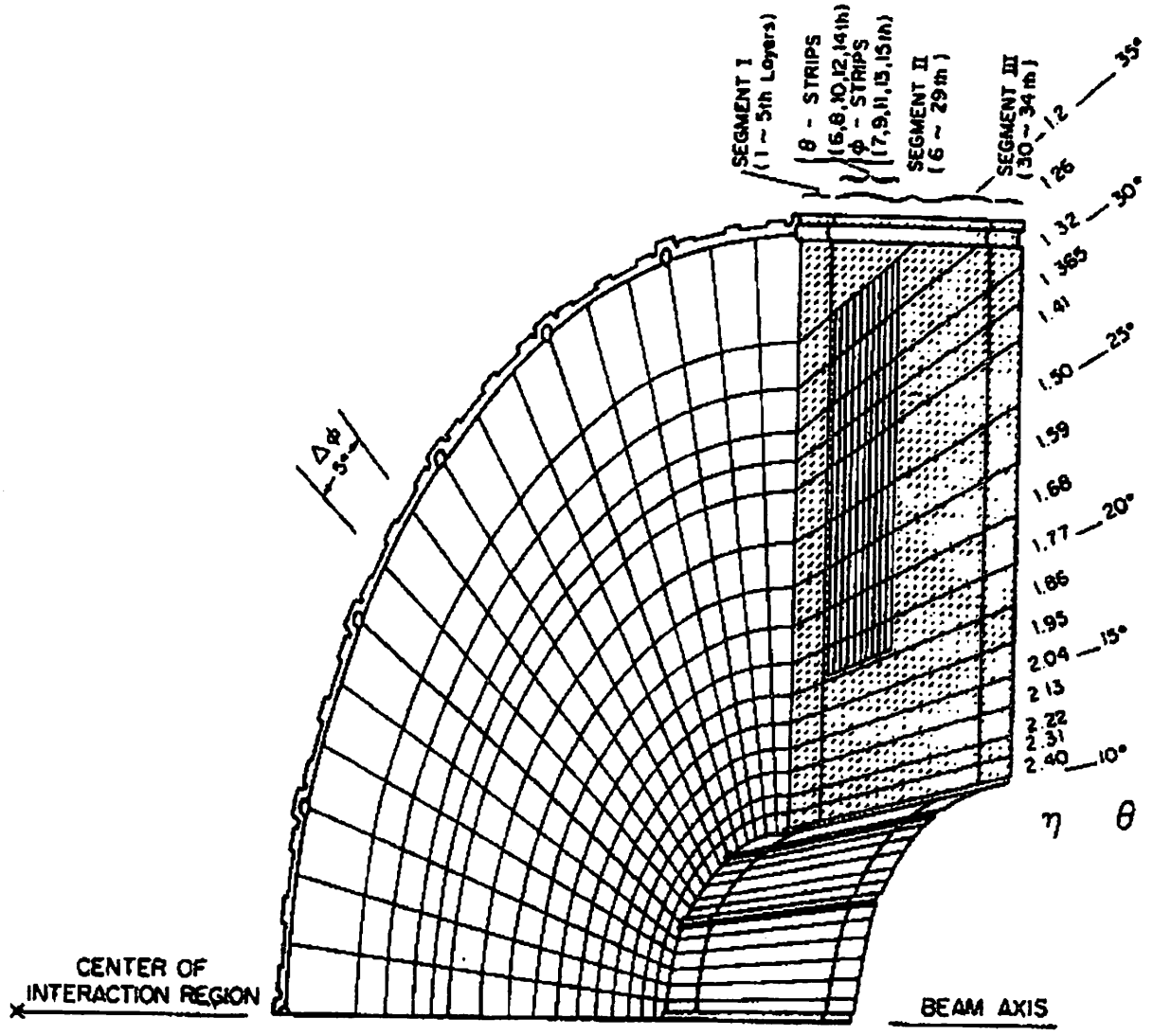

Figure 2.6: Isometric view of a PEM quadrant, showing the projective pad tower structure and the longitudinal layers.

Chapter 3

Event selection

The data collected at CDF during the 1992-1993 and 1994-1995 runs corresponding to 110 pb^{-1} are used in this Z' search. All data used in this analysis were stripped from a data stream for immediate processing after event reconstructions. In the first section, trigger requirement for this analysis is described. The next section describes electron identification and other requirements for this analysis. The efficiencies of these requirements are described in Section 3.3.

3.1 Trigger requirement

In the CDF electron triggers, there is a requirement on a ratio of the hadronic energy to the electromagnetic energy of the cluster (E_{HAD}/E_{EM}). The efficiency of the E_{HAD}/E_{EM} cut is affected by the leakage of EM shower into hadron calorimeter as well as by the limitations due to various saturations of the hardware bits in the trigger level for high E_T electrons. If we require a central electron trigger to be set, then we suffer substantial inefficiency for the high mass Z' search. However, there are other non-electron triggers which become efficient for high E_T electrons. Example of such triggers, with no E_{HAD}/E_{EM} requirements, are "JET 100" and "SUMET 175" triggers. The "JET 100" trigger requires an event to have a jet with transverse energy greater than 100 GeV and the "SUMET 175" trigger requires that sum of all jet cluster energies be greater than 175 GeV. We have studied efficiencies of the "JET 100" trigger for high E_T electrons by selecting $W \rightarrow e\nu$ events with electron E_T above 150 GeV using independent triggers. We found 202 such events and the efficiency for electron E_T above 150 GeV is 99.0 $^{+0.6}_{-0.8}$%, while the efficiency of a central electron trigger is 60.4 $^{+4.2}_{-4.5}$%. The electron trigger requires an energy cluster with $E_T > 16$

GeV and $P_T > 13$ GeV/c. As we will discuss in Section 3.3.3, the central electron trigger and a plug electron trigger led to a trigger efficiency above 99% for electrons with 25 GeV $< E_T <$ 150 GeV for dielectron events and the "JET100" trigger also led to an efficiency above 99.9% for electron $E_T > 150$ GeV.

We conclude that by accepting any combination of triggers we make the search insensitive to the E_T dependent inefficiency due to the E_{HAD}/E_{EM} cut imposed in the CDF trigger.

3.2 Electron identification

In this search, events are required to have at least one central electron candidate which satisfies a set of tight cuts and another electron candidate which passes a set of loose cuts for central or plug detector signals. These requirements are summarized in Table 3.1 and Table 3.2.

3.2.1 Central electron parameters

Transverse energy and momentum

The transverse energy (E_T) and the transverse momentum (P_T) of an electron are defined by Equation 2.4 and 2.3, respectively.

Fiducial volume for electron

In order to ensure a correct energy measurement, a fiducial region is defined so as to avoid inactive detector region. Figure 3.1 shows schematically the fiducial volume of the detector for electrons used in this analysis.

Track-shower matching variables

The CTC track pointing to an electron cluster is extrapolated to the CES. The extrapolated position is compared to the shower position as measured in the CES. The variable $|\Delta X|$ is the separation in the r-ϕ view between the extrapolated track position and the CES strip cluster position. The variable $|\Delta Z|$ is the corresponding separation in the z view. The variable $|\Delta X|$ and $|\Delta Z|$ are defined as

$$\Delta X = X_{track} - X_{CES},$$

$$\Delta Z = Z_{track} - Z_{CES},$$

where X_{track} and Z_{track} are the coordinates of the extrapolated position of the track at the radius of the strip chamber; X_{CES} and Z_{CES} are the coordinates of the shower centroid measured by the CES.

Isolation

The presence of energetic particles near an electron can be quantified by measuring the isolation variable defined as

$$Isolation = \frac{E_T^{cone} - E_T^{cluster}}{E_T^{cluster}},$$

where E_T^{cone} is the sum of the electromagnetic and hadronic transverse energies measured in all of the towers in a radius of R = $\sqrt{\Delta\phi^2 + \Delta\eta^2} = 0.4$ centered around the electron cluster. $E_T^{cluster}$ is the transverse energy of the electron cluster. The isolation requirement is not for identification of an electron cut but for a selection of the event topology. Electrons from Z^0, Drell-Yan and also Z' productions are expected to be "isolated". That is, they are not expected to be produced in association with other particles.

E_{HAD}/E_{EM}

The ratio of the hadronic energy to the electromagnetic energy is called E_{HAD}/E_{EM}. In this case (unlike the trigger level), dynamic range effects are not a problem for electron energies relevant for this measurement (electron E_T < 350 GeV).

E/P

The ratio of the electron energy to the electron track momentum, $E/P \equiv E_T/P_T$, is used to verify matching between the CEM and the CTC measurements of the electron energy. Since high energy electrons tend to radiate in the detector, the E/P cut is only applied on the electrons whose transverse momenta are less than 50 GeV/c.

3.2.2 Plug electron parameters

Since the CTC does not cover the entire plug region, track requirements are not imposed for PEM electron candidates. For plug electron candidates, Isolation, E_{HAD}/E_{EM} and $\chi^2_{3\times3}$ are imposed. The $\chi^2_{3\times3}$ is a χ^2 obtained by comparing observed lateral shower shape with the predicted shape from test beam electrons. The shape comparison is performed in the 3 towers in η by the 3 towers in ϕ around the electron cluster's center.

3.2.3 Central electron identification

The requirements on the central electrons in the Z' search are shown in Table 3.1. The "loose" cuts is the same set of the "tight" cuts except for the isolation cut. Figures 3.2 and 3.3 (a) show the distributions of electron identification variables for central electron candidates.

Variable	tight cuts	loose cuts
Isolation	< 0.1	< 0.2
E_T	> 25 GeV	
P_T	> 13GeV/c	
$\lvert\Delta X\rvert$	< 3 cm	
$\lvert\Delta Z\rvert$	< 5 cm	
E_T/P_T	< 4.0 or $P_T > 50$ GeV/c	
E_{HAD}/E_{EM}	$< 0.055 + 0.00045 \times$ E	
Fiducial cut		

Table 3.1: Central electron selection requirements.

3.2.4 Plug electron identification

The requirements on the plug electrons in the Z' search are shown in Table 3.2. Figures 3.3 (b)-(d) show the distributions of electron identification variables for plug electron candidates.

Variable	loose cuts
E_T	> 25 GeV
Isolation	< 0.1
E_{HAD}/E_{EM}	$< 0.055 + 0.00045 \times$ E
$\chi^2_{3\times3}$	< 3
Fiducial cut	

Table 3.2: Plug electron selection requirements.

3.2.5 Event topology cuts

Missing E_T significance

To eliminate background from $W \rightarrow e\nu$ and $Z \rightarrow \tau\bar{\tau}$ events, a missing E_T significance(S) is required less than 2.5. The missing $E_T(\not\!\!E_T)$ and S are defined as

$$\not\!\!E_T = |(-1) \times \sum \overrightarrow{E_T^i}|,$$
$$S = \frac{\not\!\!E_T}{\sqrt{\sum E_T^i}}, \tag{3.1}$$

where $\overrightarrow{E_T^i}$ is a two-dimensional vector whose magnitude is the transverse energy in a calorimeter tower and whose direction points in the transverse plane from the event vertex to the center of the calorimeter tower. The $\sum E_T^i$ is a scalar sum of the transverse energy of the calorimeter tower's over-all calorimeter towers. Figure 3.4 (a) shows the S distributions of the W (see appendix A) events. Figure 3.4 (b) shows the S distributions of the Z events with the requirements of the dielectron invariant mass between 70 GeV/c^2 and 110 GeV/c^2 in addition to the identical requirements for the Z' search sample.

3.2.6 Event vertex

Figure 3.5 shows the distribution of z coordinate of the primary vertex (z_{vertex}) for the sample of these events. To insure good containment of the electrons in the calorimeters, we require the z_{vertex} of each event to be within 60 cm of the center of the detector.

3.2.7 Result of the selection

Figures 3.6 and 3.7 show dielectron invariant mass distributions satisfying our selection criteria at an integrated luminosity of 110 pb^{-1}. The sample contains 7120 events of which 4311 have both electrons in the central calorimeter (C-C) and 3709 have one electron in the central and the other electron in the plug calorimeters (C-P). The largest mass observed is 511 GeV/c^2. Figure 3.8 shows event pictures of the largest mass event.

3.3 Detection efficiency

In the previous section, event selection criteria for $Z' \rightarrow e^+e^-$ search were described. In this section, the efficiencies of these cuts and acceptance are described. The total detection efficiency ε_{total} can be written as

$$\varepsilon_{total} = \varepsilon_{acc}(M) \cdot \varepsilon_{ID} \cdot \varepsilon_{zvertex} \cdot \varepsilon_S \cdot \varepsilon_{trigger}, \tag{3.2}$$

where $\varepsilon_{acc}(M)$ is a geometrical and kinematical acceptance as a function of invariant mass of the dielectrons, M. ε_{ID} is an efficiency of identification cut including the isolation cut, $\varepsilon_{zvertex}$ is an efficiency of the event vertex cut, ε_S is an efficiency of the S cut, and $\varepsilon_{trigger}$ is the trigger efficiency.

3.3.1 Efficiency of identification cut

The ε_{ID} can be written as

$$\varepsilon_{ID} = 2\varepsilon_t\varepsilon_l - \varepsilon_t^2, \tag{3.3}$$

$$\varepsilon_{ID} = \varepsilon_t\varepsilon_p, \tag{3.4}$$

where ε_t, ε_l and ε_p are total efficiencies for the "tight" central electron cuts, for the "loose" central electron cuts, and that for the "loose" plug electron cuts, respectively.

The efficiency of the identification cut is determined from a sample of $Z \rightarrow e^+e^-$ decays, in which no selection biases are applied to one of the electron candidates (e_2). The efficiency for each cut is studied by imposing that cut on the second electron candidates, e_2. To ensure a 'clean' Z sample the events are required to have a central electron (e_1) satisfying stringent identification requirements and a dielectron invariant mass between 70 GeV and 110 GeV/c^2. The stringent electron cuts include the

"tight" cuts described in Section 3.2 and also a requirement that there be only one 3-dimensional track pointing to the central EM cluster of the electron. The other electron candidate (e_2) can be in the central or plug calorimeter, with none of the identification cuts applied. We use the number of the same-sign events in the sample to estimate the number of background events other than Z production in the control sample. As we will discuss the background events in our Z' search sample in Section 4, the major source of the same-sign events is a jet which fakes an electron candidate. Since the fake rate of jets to e^+ is equal to that to e^-, the number of the same-sign events in the sample is considered to be the number of opposite-sign background events.

In order to ensure a charge information of a plug electron candidate, we further require plug electron candidates have hits on the CTC super layer 0 (SL0), SL1, SL2, SL3, and SL4, because the CTC only covers $|\eta| < 1.5$ from the center of the detector. A reduced χ^2 (χ^2_N) of the reconstructed track is also required to be less than 2.0. The χ^2_N is defined as

$$\chi^2_N \equiv \frac{\chi^2}{N-1},$$

where N is the number of freedom.

This control sample consists of 2519 of the C-C and 361 of the C-P Z events, in which there are 38 of the C-C and 12 of the C-P same-sign events. Figures 3.2 and 3.3 show the distributions of variables used in the analysis, where the arrows indicate the cut thresholds. Tables 3.3 and 3.4 summarize the efficiencies for the central and plug electrons.

The efficiencies of the total "tight" and "loose" cuts are obtained by simultaneously imposing all the "tight" or "loose" cuts on the second electron candidates, e_2.

The total efficiency for the "tight" central electron cuts (ε_t), the "loose" central electron cuts (ε_l), and the "loose" plug electron cuts (ε_p) can be expressed as

$$\begin{cases} \varepsilon_t &= \dfrac{N_{tt}+N_{tt}}{N_{cc}+N_{tt}}, \\ \varepsilon_l &= \dfrac{N_{tl}+N_{tt}}{N_{cc}+N_{tt}}, \\ \varepsilon_p &= \dfrac{N_{tp}}{N_{cp}}, \end{cases} \tag{3.5}$$

Cut	Number of candidate events	Number of background events	Efficiency
Iso $<$ .1	2327	24	97.0 ± 0.3 %
Iso $<$ .2 ('loose' cut)	2435	34	99.1 ± 0.2 %
E/p $<$ 4 or $p_T >$ 50 GeV/c	2518	76	$99.98\ ^{+\ 0.02}_{-\ 0.1}$ %
$\lvert\Delta X\rvert \leq$3 cm	2439	56	98.7 ± 0.2 %
$\lvert\Delta Z\rvert \leq$5 cm	2462	52	99.3 ± 0.2 %
Had/Em $<$ 0.055 + 0.00045 $* E$	2471	60	99.3 ± 0.2 %
Total efficiency for 'tight' Central e's:			94.9 ± 0.4 %
Total efficiency for 'loose' Central e's:			96.8 ± 0.3 %

Table 3.3: Efficiency of analysis cuts: Central Region

Cut	Number of candidate events	Number of background events	Efficiency
Iso $<$ .1	353	22	$98.2\ ^{+\ 1.2}_{-\ 1.7}$ %
$\chi^2_{3X3} \leq$3	344	24	$95.0\ ^{+\ 1.5}_{-\ 1.7}$ %
Had/Em $<$ 0.055 + 0.00045 $* E$	359	24	$99.4\ ^{+\ 1.0}_{-\ 1.3}$ %
Total efficiency for 'loose' Plug e's:			$94.1\ ^{+\ 1.6}_{-\ 1.8}$ %

Table 3.4: Efficiency of analysis cuts: Plug Region

where $N_{tt}, N_{tl}, N_{tp}, N_{cc}$ and N_{cp} are defined by

$$\begin{cases} N_{cc} \equiv N_{cc}^{obs} - 2N_{cc}^{same}, \\ N_{cp} \equiv N_{cp}^{obs} - 2N_{cp}^{same}, \\ N_{tt} \equiv N_{tt}^{obs} - 2N_{tt}^{same}, \\ N_{tl} \equiv N_{tl}^{obs} - 2N_{tl}^{same}, \\ N_{tp} \equiv N_{tp}^{obs} - 2N_{tp}^{same}, \end{cases} \tag{3.6}$$

with

$$\begin{cases} N_{cc}^{obs} \equiv \text{number of C-C } Z \text{ events,} \\ N_{cp}^{obs} \equiv \text{number of C-P } Z \text{ events,} \\ N_{tt}^{obs} \equiv \text{number of C-C, "tight-tight" events,} \\ N_{tl}^{obs} \equiv \text{number of C-C, "tight-loose" events,} \\ N_{tp}^{obs} \equiv \text{number of C-P, "tight-plug " events,} \end{cases} \tag{3.7}$$

and

$$\begin{cases} N_{cc}^{same} \equiv \text{number of C-C same-sign events,} \\ N_{cp}^{same} \equiv \text{number of C-P same-sign events,} \\ N_{tt}^{same} \equiv \text{number of C-C same-sign events in "tight-tight" events,} \\ N_{tl}^{same} \equiv \text{number of C-C same-sign events in "tight-loose" events,} \\ N_{tp}^{same} \equiv \text{number of C-P same-sign events in "tight-plug" events.} \end{cases} \tag{3.8}$$

We calculate ε_t, ε_l and ε_p to be 94.9% $\pm$ 0.4%, 96.8% $\pm$ 0.3% and 94.1% $^{+\,1.6}_{-\,1.8}$ % respectively.

3.3.2 Energy dependences of identification cuts

We take particular care to choose cuts that maintain high efficiency for high E_T electrons. The E_T dependence of each electron identification cut is studied by using a control sample selected for the efficiency study. Figure 3.9 shows the $E_T(P_T)$ dependence of the mean values of each central electron identification cut. Figure 3.10 shows the $E_T(P_T)$ dependence of the efficiency of each electron central identification cut. Figure 3.11 shows the same distributions for plug electrons.

Within the limited statistics, we can state that these cuts are efficient for high E_T electrons. We perform a similar study using a higher statistic W electron sample. The selection criterion of the W sample is described in appendix A. In order to select pure W sample we need to use the electron selection cuts which we use for our analysis. Thus, we can not get true efficiencies of each identification cut variable from this sample. However, we can look at the tendency of behavior of the selection cuts as a function of the E_T. Figure 3.12 show the $E_T(P_T)$ dependence of the mean values of each central electron identification cut using the W sample. The plots indicate that our electron identification cuts tend to be efficient for high E_T electrons.

3.3.3 Other efficiencies

Efficiencies of the S cut and the event vertex cut

To establish efficiencies of the S cut and the event vertex cut, we use a sample of Z events, with both electrons passing central "tight" cuts, and invariant mass of the electron pairs between 80 GeV/c^2 and 100 GeV/c^2. In addition, we require that the electron pairs have opposite charge. After requiring $S < 2.5$ on the Z sample, we get 99.6 $\pm$ 0.1% of efficiency.

Figure 3.5 shows the distribution of z coordinate of the primary vertex for the sample of these events. The distribution shows 94.9 $\pm$ 0.4% of events have the event vertex within 60 cm of the detector center. A gaussian fit to this distribution gives a mean value of 1.6 $\pm$ 0.6 cm and standard deviation of 27.6 $\pm$ 0.5 cm.

Trigger efficiency

The data used in this analysis was selected if an event passed any triggers in order to avoid the E_T dependence of inefficiency which was described in Section 3.1. The efficiencies of main electron triggers are estimated from $W \rightarrow e\nu$ events selected with $\not\!\!E_T$ triggers which are independent of electron triggers. For electrons with 25 GeV $< E_T <$ 150 GeV, the central electron trigger that requires $E_T > 16$ GeV and $P_T >$ 13 GeV/c has an efficiency for central electrons of 92.1 $\pm$ 0.1%. An efficiency of an electron trigger for plug electrons that requires an energy cluster with $E_T > 20$ GeV is 94.6 $\pm$ 0.4%. Since either electron could provide the trigger, this led to trigger efficiency of 99.4% for C-C events and 99.6% for C-P events for electron with 25 GeV $< E_T <$ 150 GeV. For electron $E_T > 150$ GeV, an efficiency of the "JET100" trigger is 99.0 $^{+0.6}_{-0.8}$%(Section 3.1). This led to a trigger efficiency more than 99.9% for dielectron events. Hence trigger efficiency for this search is higher than 99.4% for electrons with $E_T > 25$ GeV.

3.3.4 Acceptance

A Monte Carlo simulation is used for determination of the geometrical and kinematical acceptance[24]. The Monte Carlo events are generated by using the leading order diagrams for Z, Drell-Yan and Z' productions. No quark-gluon diagrams or initial-state radiation are considered. In order to mimic the effects of higher-order

diagrams, the events are generated with Z P_T distribution measured in the 1988-1989 at CDF. The MRSD$-'$ parton distribution function [25] is used. We generate 100,000 events for various invariant mass of Z'. The electrons are propagated to the calorimeter and their momenta are smeared according to the nominal detector resolutions (Table 2.2). The event vertex of each event is smeared with a gaussian distribution with a sigma of 27.3 cm in the region (-60.0 cm $< z_{vertex} <$ 60.0 cm).

The same fiducial region of calorimeters (Section 3.2.1) is considered. For both central and plug electrons a kinematical requirement, $E_T > 25$ GeV, is required.

A mass dependence of the acceptance is shown in Figure 3.13. The combined acceptance of C-C and C-P is fairly flat for the dielectron mass greater than 250 Gev/c^2 and slightly above 50%.

3.3.5 Total efficiency

The total efficiencies can be written as

$$\varepsilon_{total}^{c-c}(M) = 0.885 \times \varepsilon_{acc}^{c-c}(M), \tag{3.9}$$

$$\varepsilon_{total}^{c-p}(M) = 0.844 \times \varepsilon_{acc}^{c-p}(M), \tag{3.10}$$

where $\varepsilon_{total}^{c-c}(M)$ and $\varepsilon_{total}^{c-p}(M)$ are the total efficiencies for C-C and C-P events. $\varepsilon_{acc}^{c-c}(M)$ and $\varepsilon_{acc}^{c-p}(M)$ are the acceptances for C-C and C-P events. We assume 100% of the trigger efficiency in the total efficiency calculations. Figure 3.14 shows efficiencies for C-C, C-P and both events. For dielectron mass above 300 GeV/c^2, the total efficiency is fairly constant and is around 47%.

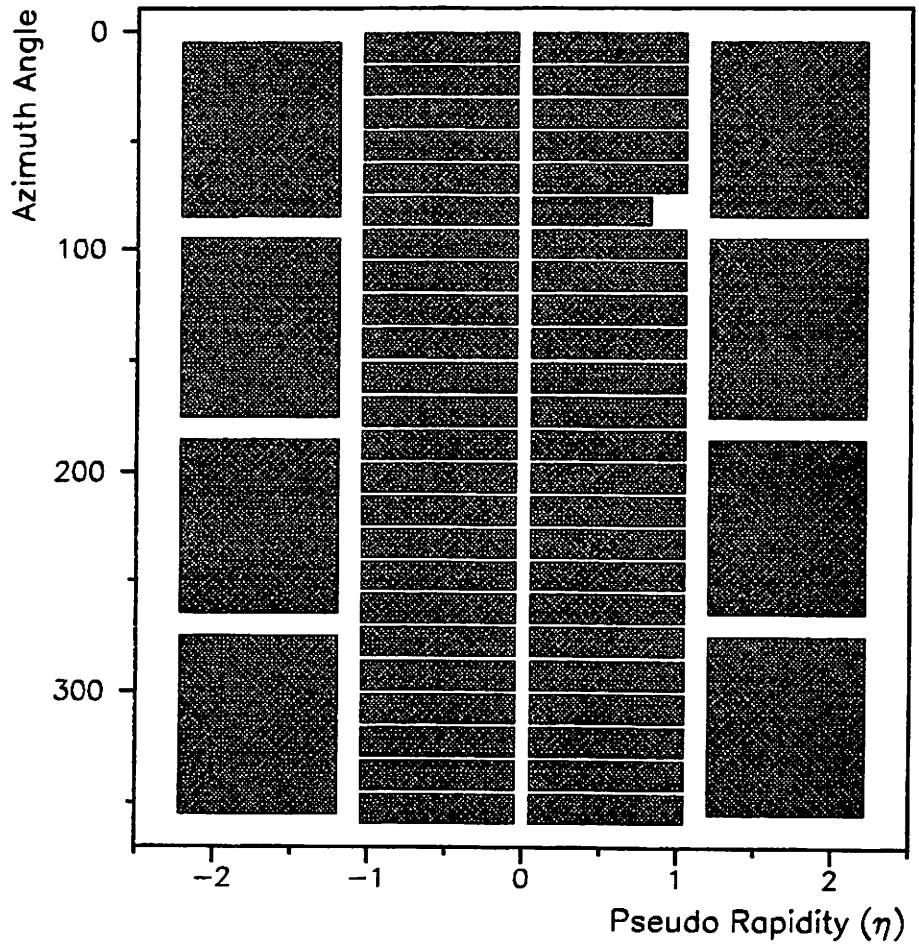

Figure 3.1: Map in η-ϕ space of fiducial volume for electrons. Hatched areas indicate part of fiducial volumes.

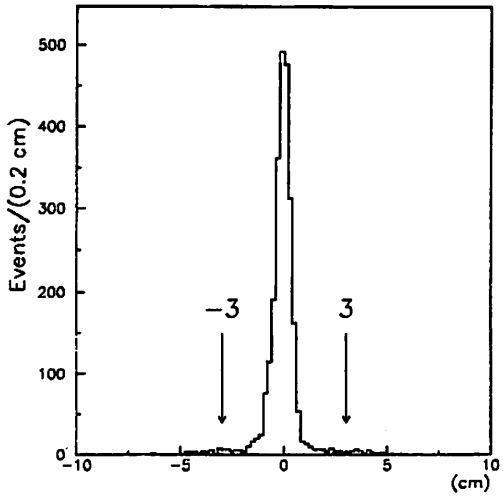

3.2 - (a) Central $|\Delta X|$

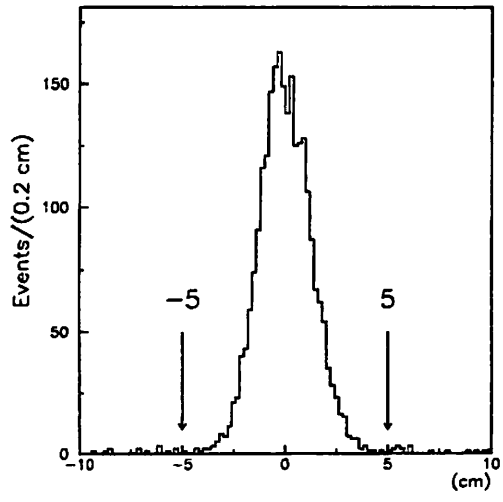

3.2 - (b) Central $|\Delta Z|$

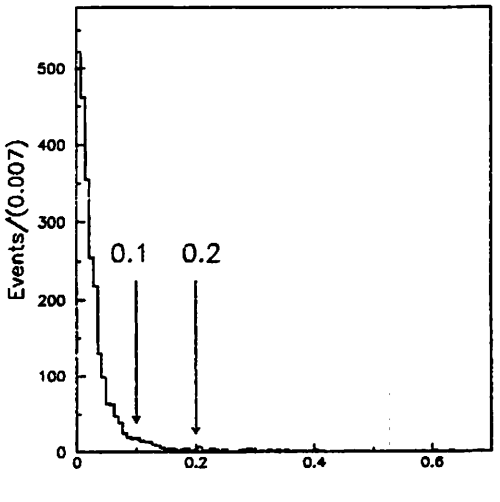

3.2 - (c) Central Isolation

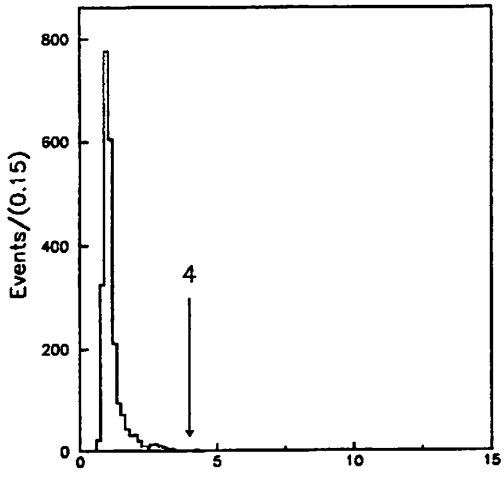

3.2 - (d) Central E/P with $P_T < 50\text{GeV}/c$

Figure 3.2: Distributions of electron identification variables including the isolation cut for central electron candidates. The arrows indicate the cut thresholds.

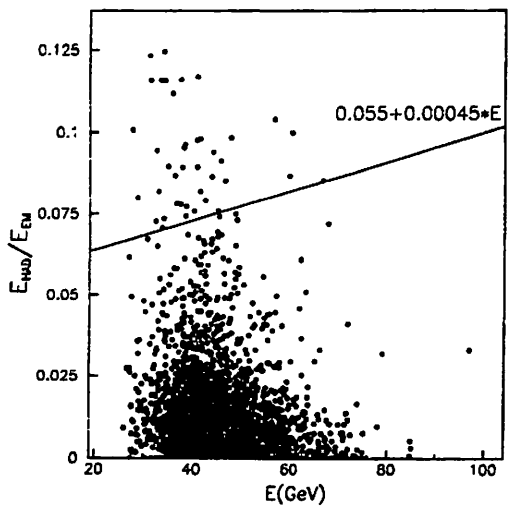

3.3 - (a) Central E_{HAD}/E_{EM}

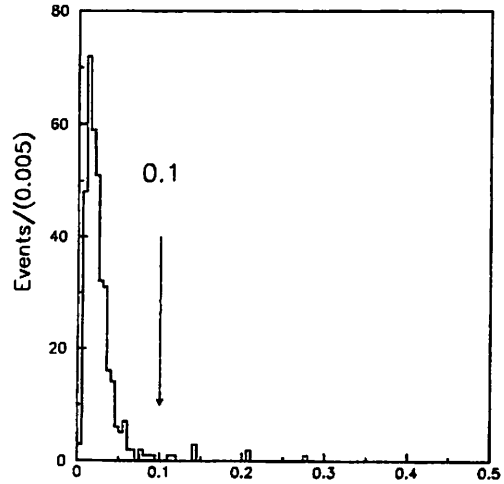

3.3 - (b) Plug Isolation

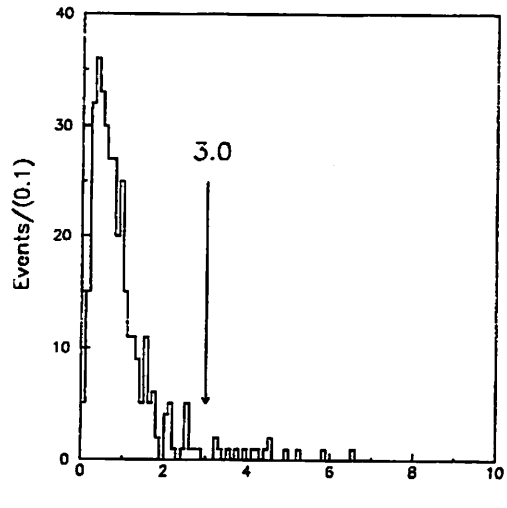

3.3 - (c) Plug $\chi^2_{3\times3}$

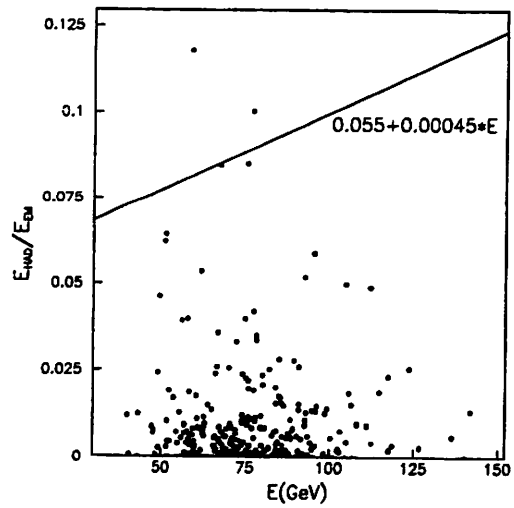

3.3 - (d) Plug E_{HAD}/E_{EM}

Figure 3.3: Distributions of electron identification variables including the isolation cut. Figure (a) shows E_{HAD}/E_{EM} for central electron candidates. Figure (b) $\sim$ (d) show distributions for plug electron candidates. The arrows indicate the cut thresholds.

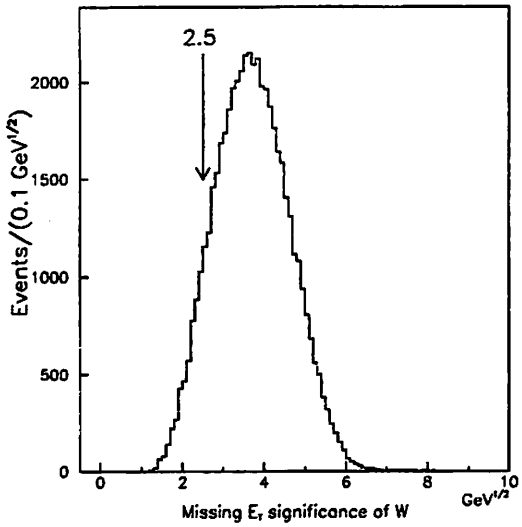

3.4 - (a) The $\not\!\!E_T$ significance distribution of W sample.

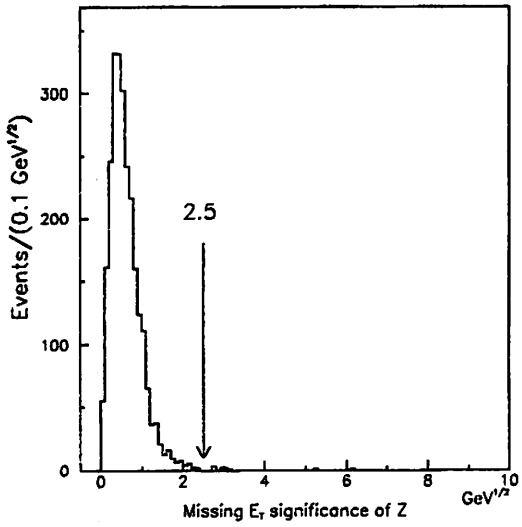

3.4 - (b) The $\not\!\!E_T$ significance distribution of Z sample.

Figure 3.4: The $\not\!\!E_T$ significance distributions of W and Z samples. Arrows indicate cut value we applied.

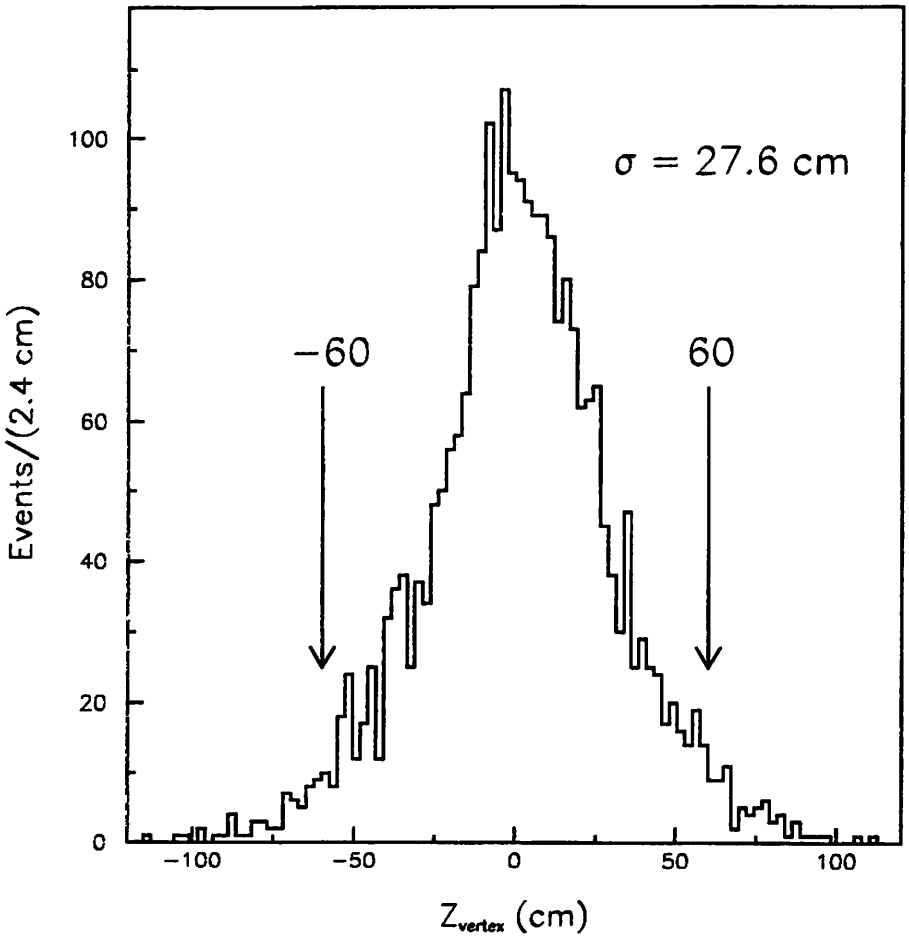

Figure 3.5: The z coordinate of the primary vertex.

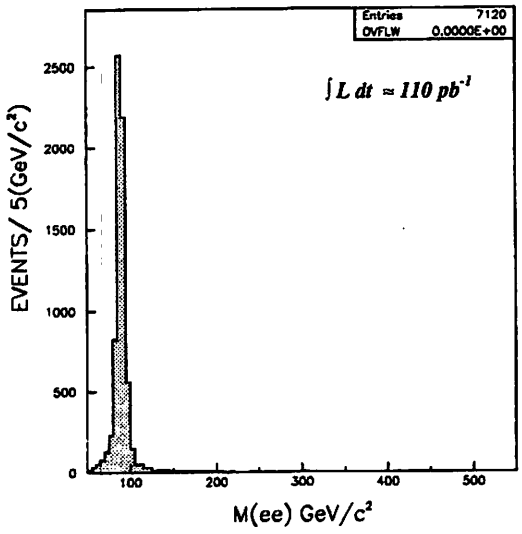

3.6 - (a)

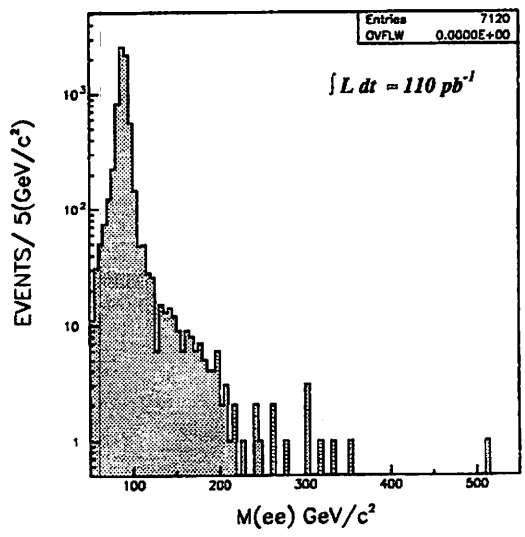

3.6 - (b)

Figure 3.6: The invariant mass distribution for 7120 dielectron candidates; (a) linear, (b) log vertical scale.

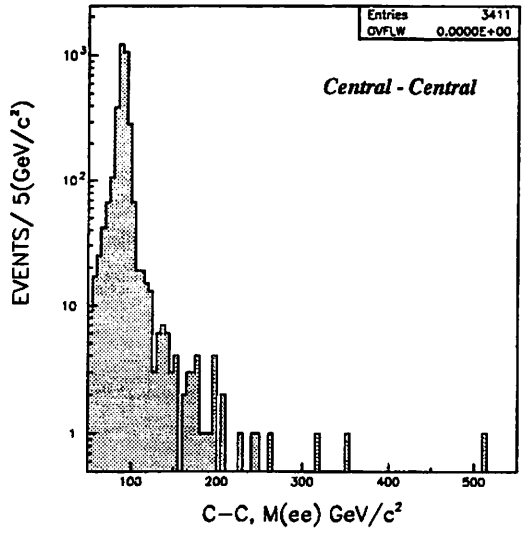

3.7 - (a) The invariant mass distribution for 3411 dielectron candidates in the C-C category

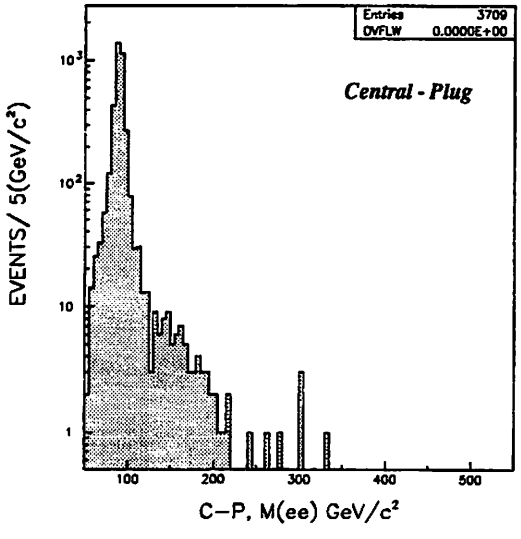

3.7 - (b) The invariant mass distribution for 3709 dielectron candidates in the C-P category

Figure 3.7: Figure (a),(b) show invariant mass distributions of the C-C and C-P categories.

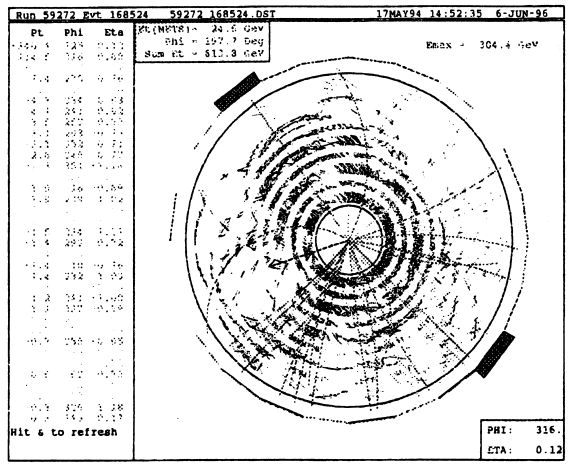

3.8 - (a)

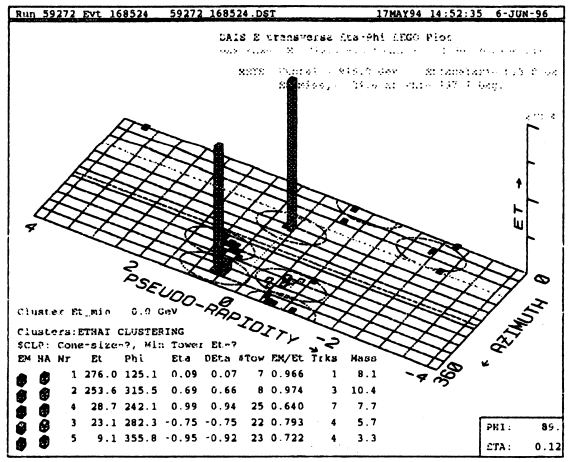

3.8 - (b)

Figure 3.8: Event pictures of the highest invariant mass event.

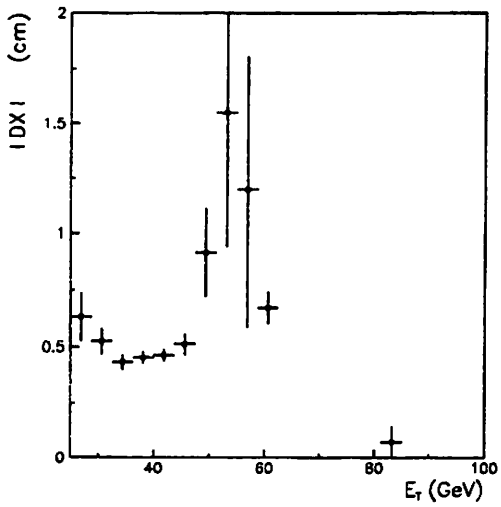

3.9 - (a) Central $|\Delta X|$

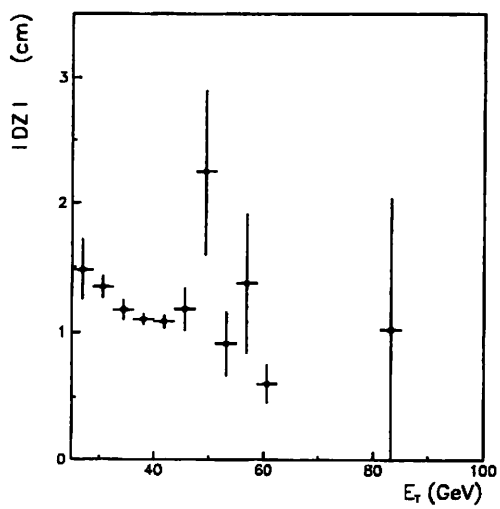

3.9 - (b) Central $|\Delta Z|$

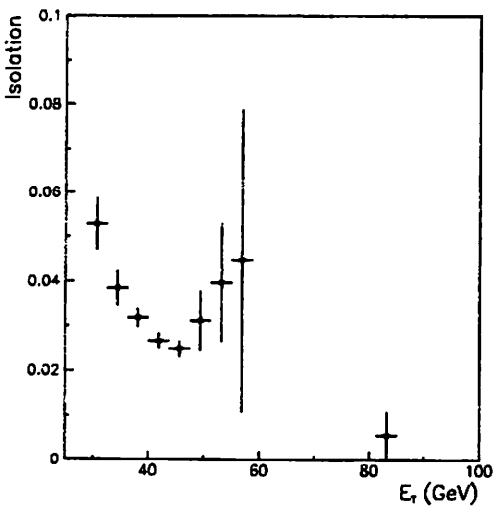

3.9 - (c) Central Isolation

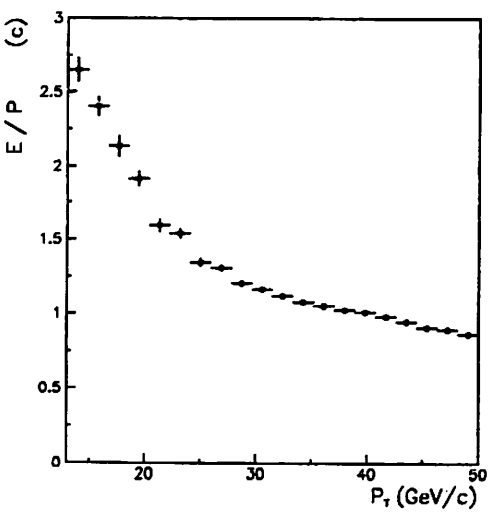

3.9 - (d) Central E/P with $P_T < 50\text{GeV}/c$

Figure 3.9: The $E_T(P_T)$ dependence of the mean of each variable for central electrons in the Z efficiency sample.

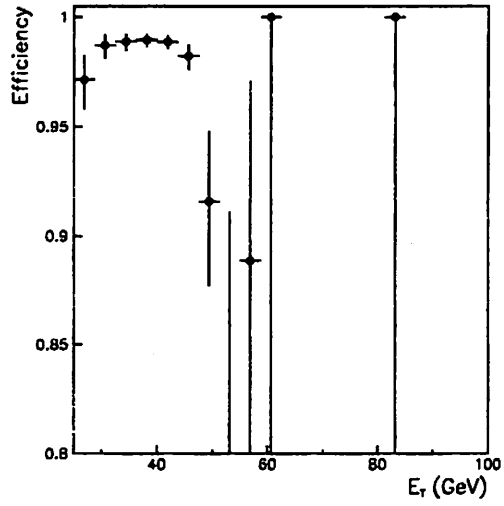

3.10 - (a) Central $|\Delta X|$

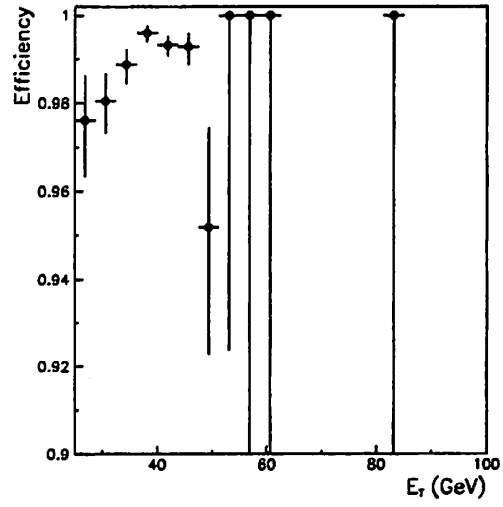

3.10 - (b) Central $|\Delta Z|$

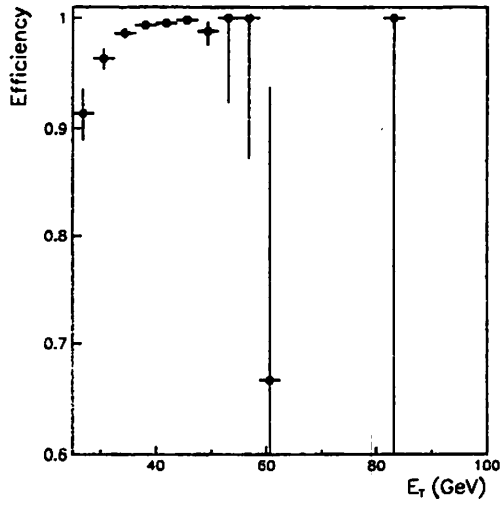

3.10 - (c) Central Isolation

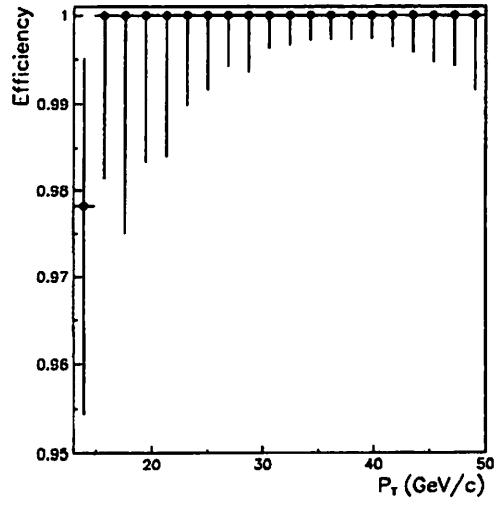

3.10 - (d) Central E/P with $P_T < 50\text{GeV}/c$

Figure 3.10: The $E_T(P_T)$ dependence of the efficiency of the various cuts on the central electrons in the Z efficiency sample.

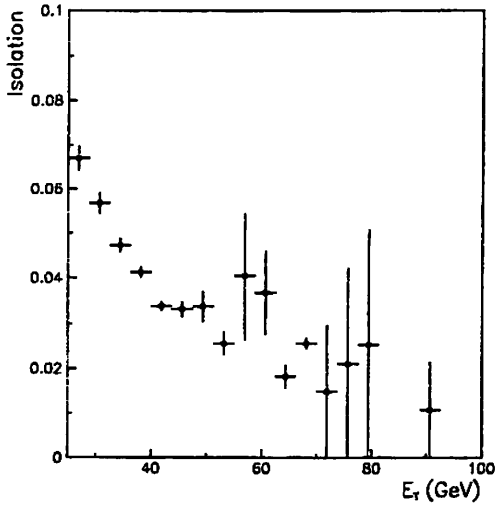

3.11 - (a) Plug Isolation

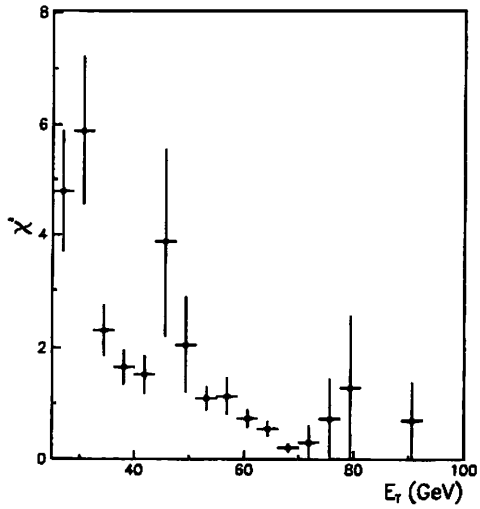

3.11 - (b) Plug $\chi^2_{3\times3}$

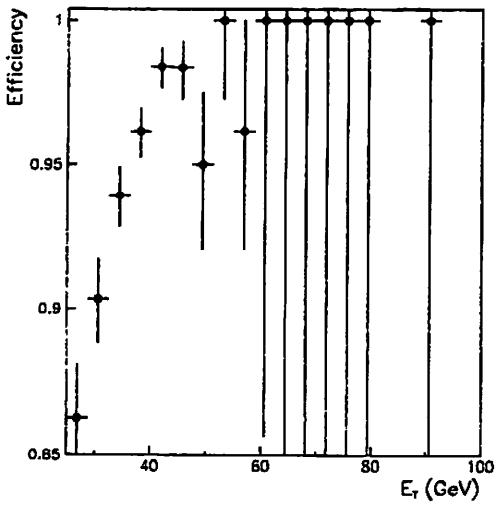

3.11 - (c) Plug Isolation

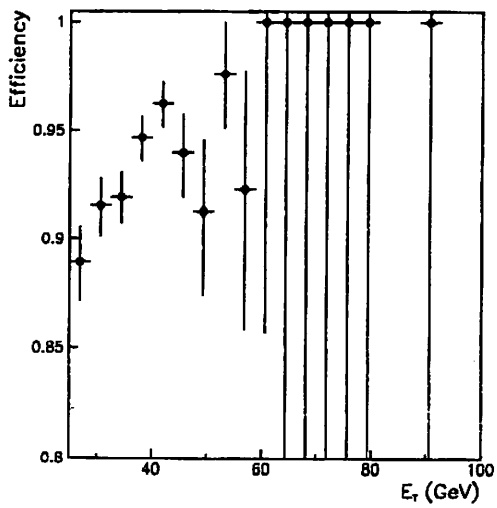

3.11 - (d) [Plug $\chi^2_{3\times3}$

Figure 3.11: Top two figures show the E_T dependence of the mean of each variable for the plug electrons in the Z efficiency sample without opposite charge requirement. Bottom two figures show E_T dependence of efficiency of the various cuts on the plug electrons.

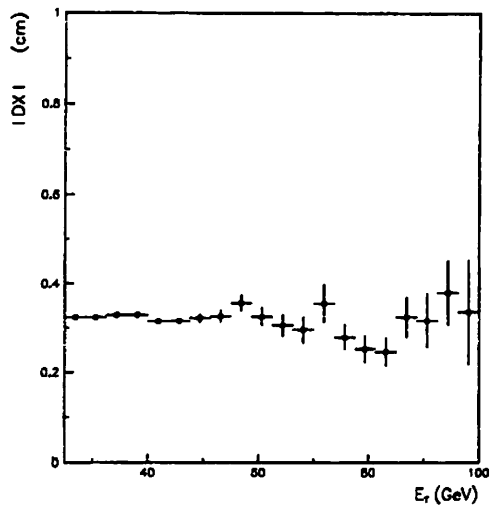

3.12 - (a) Central $|\Delta X|$

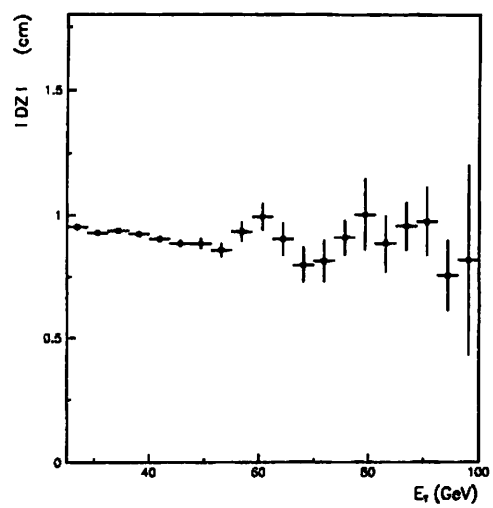

3.12 - (b) Central $|\Delta Z|$

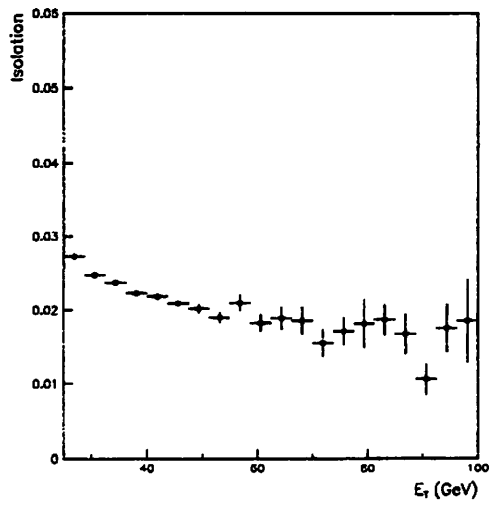

3.12 - (c) Central Isolation

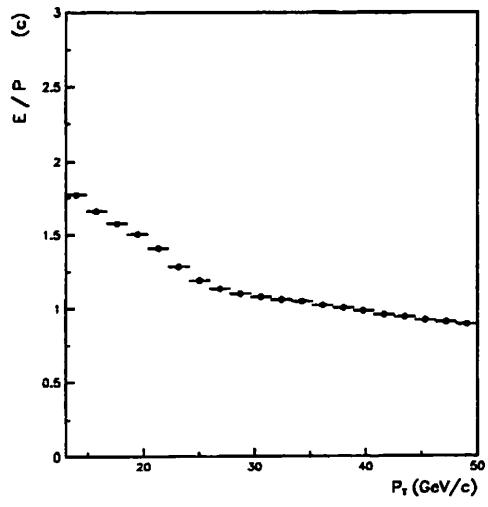

3.12 - (d) Central E/P with $P_T < 50\text{GeV}/c$

Figure 3.12: The $E_T(P_T)$ dependence of the mean of each variable for central electrons in the W sample.

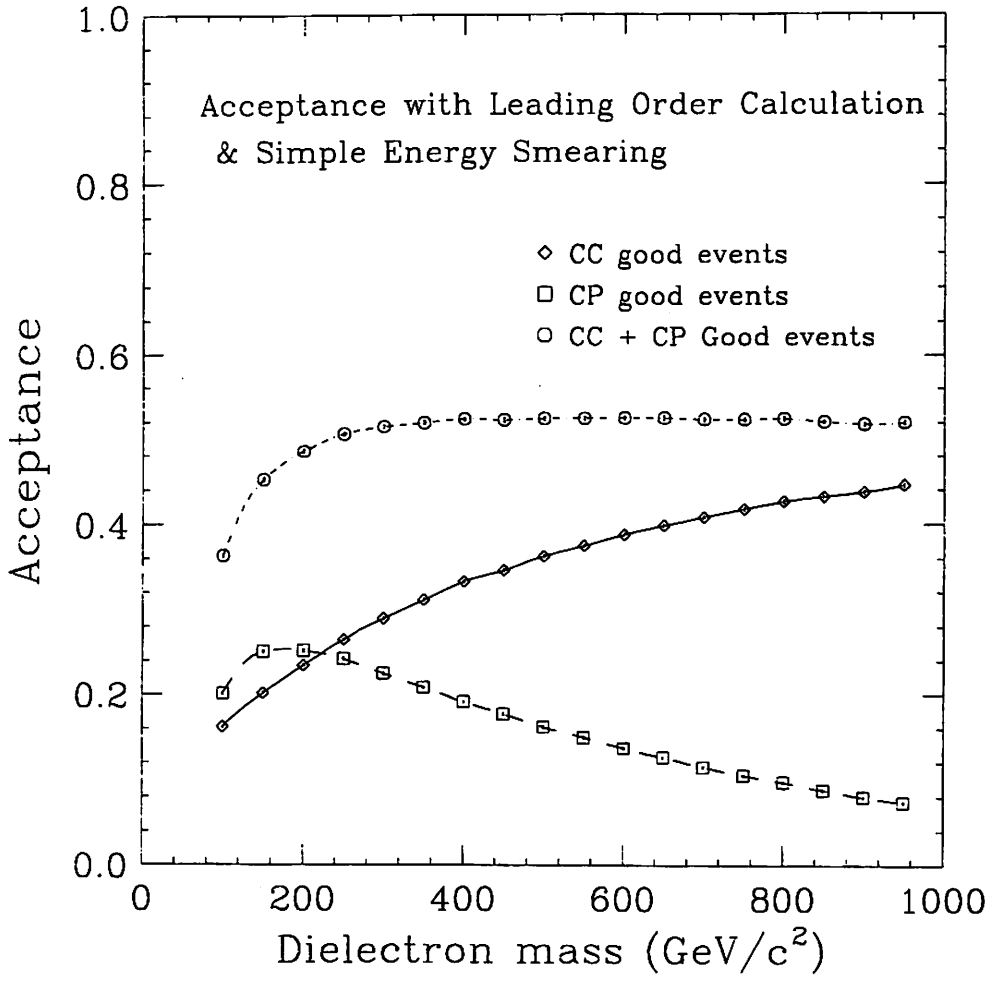

Figure 3.13: Dielectron mass dependence of geometrical and kinematical acceptance.

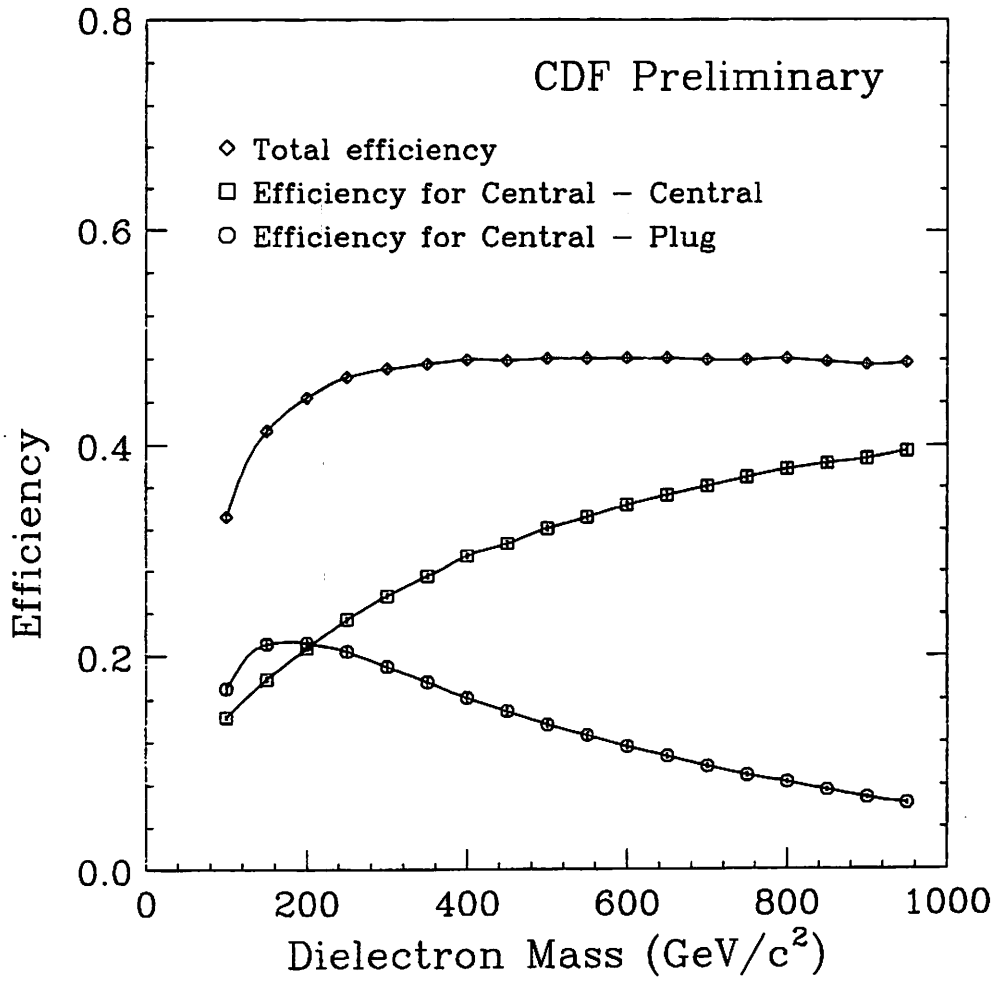

Figure 3.14: The total efficiency including geometrical and kinematical acceptance as a function of the dielectron mass.

Chapter 4

Background estimation

The background sources of the $Z' \rightarrow e^+e^-$ can be classified into three categories. The first source has the same final state, e^+e^-, and thus, interferes with Z' productions. Topology of the second category is different from Z' events. Hence, these events are able to be eliminated by topological cuts. The last one is not a real dielectron event but an event in which jets fake electron candidates. The backgrounds under consideration are

1. Drell-Yan, $Z \rightarrow e^+e^-$,
2. (a) $Z \rightarrow \tau^+\tau^-$,
   (b) Diboson productions (WW,WZ,ZZ),
   (c) $t\bar{t}$,
   (d) $b\bar{b}$,
3. fake events.

The dominant background in the high mass region where we are looking for Z' is expected to be the Drell-Yan production. Section 4.1 describes a comparison of data with expected Drell-Yan events and Section 4.2 describes estimations of other dielectron background events in our sample. Section 4.3 describes background events from fake electrons.

4.1 Comparison of data with Drell-Yan events

The expected numbers of dielectron events from the Drell-Yan and Z boson productions (DY+Z) are estimated with the Monte Carlo simulation (MC) described

in Section 3.3.4. Table 4.1 shows a comparison of data with the Monte Carlo results for dielectron mass above 150 GeV/c^2. Figure 4.1 (a) and (b) show the comparison for C-C and C-P events separately. In the region of the dielectron mass above 150 GeV/c^2, observed C-P events are consistently higher than the Drell-Yan predictions, while the differences between observed C-C events and the Drell-Yan predictions are smaller than C-P category. This indicates that for C-P category there is substantial contribution of background events from a source other than the Drell-Yan production.

Mass GeV/c^2	(DY + Z) MC		CDF data	
	C-C	C-P	C-C	C-P
M > 150	15.5	15.3	26	44
M > 200	6.0	4.8	8	11
M > 250	2.7	1.8	3	6
M > 300	1.3	0.8	2	4
M > 350	0.7	0.3	2	0
M > 400	0.4	0.2	1	0
M > 450	0.2	0.1	1	0
M > 500	0.1	0.0	1	0
M > 550	0.1	0.0	0	0
M > 600	0.0	0.0	0	0

Table 4.1: Data compared with the expected number of events from the DY+Z Monte Carlo simulation.

4.2 Other dielectron background

To estimate the number of background events from the second category, ISAJET[26] (version 7.06) Monte Carlo simulator and QFL CDF detector simulator [27] are used.

The estimated number of events are shown in Table 4.2. A few events from $b\bar{b}$ and $Z(\tau\bar{\tau})$ are expected in our Z' search sample. In the region of dielectron mass above 150 GeV/c^2, the expected number of events is very small. The major source contributing to the difference between data and Drell-Yan expectation is not from the second type background events.

e^+e^- source	Events($M_{ee} > 150\text{GeV}/c^2$)
$b\bar{b}$	0.8 ± 0.4
$t\bar{t}$	0.4 ± 0.2
WW	< 0.2
WZ	0.04 ± 0.02
ZZ	0.02 ± 0.02
$Z(\tau\bar{\tau})$	< 0.1

Table 4.2: The estimated number of events from the second type background sources.

4.3 Fake electron events

The last category is the fake electron events. In order to keep high efficiency for Z' events, our electron identification cuts are relatively looser than ones for Z boson or Drell-Yan studies at CDF [28][29]. Hence, more events with fake electrons are expected.

4.3.1 Background estimation with the same-sign events

The number of the fake events are estimated with the same-sign events. A charge of the fake electron is determined with the highest P_T track pointing to the calorimeter tower. The probability of negative charge found in the highest P_T track in a jet is roughly the same one of positive charge. From a dijet sample, a ratio

$$f = \frac{\text{number of the same-sign events}}{\text{number of the opposite-sign events}}$$

is estimated. Events which pass our Z' search cuts are removed from this dijet sample for this study. In the leading two jets in the sample, charges of the the highest P_T tracks in each jet are used in the charge determination. In this sample, 26182 same-sign and 27192 opposite-sign events are found. This leads to $f = 0.96 \pm 0.01$.

While the charges of electron candidates in the central region can be determined by the CTC, the charges of most plug electron candidates cannot be determined since the CTC does not cover most of the plug region. Additional requirements listed below are imposed on the plug electron candidates to determine its charge.

- The track of an electron candidate has a hit in all of the CTC super layer 0 (SL0), SL1, SL2, SL3, and SL4.
- A reduced χ^2 of the track < 2.0 .

We find 26 same-sign events in the C-C events and 15 same-sign events out of 390 events in the C-P events. Figure 4.2 show the invariant mass distributions of the same-sign events. The number of fake electron events from jet events are estimated to be 52 ± 10 and 234.1 ± 60.5 events in the C-C and C-P samples, respectively.

4.3.2 Background estimation from the electron isolation

As a cross check, the isolation as a topological cut is used to estimate the number of the fake events. Since a jet event will be expected to be produced in association with other particles, the isolation of the jet event is higher than ones of the Z, Z' or Drell-Yan events. The second type background events ($b\bar{b}$, $t\bar{t}$, etc) are also expected to have high isolation, since electrons of these types of events are produced in association with other particles. However, as discussed in Section 4.2, we expect very small number of these type of events in the Z' search sample. Hence we assume that most events which have high isolation are jet events.

To estimate the number of background events, a control sample is made by imposing all our analysis cuts except for the isolation cut. The events are categorized as shown in Figure 4.3. Iso_1 and Iso_2 are the isolations of the first and second electron candidates, respectively. In this study, there are two assumptions listed below:

- There is no correlation between Iso_1 and Iso_2.
- All signal events are only in region I and all events in other regions including second type events are background events.

Figure 4.4 shows a scatter plot of the isolations in the control sample. There is no significant correlation between Iso_1 and Iso_2 in the figure. Figures 4.5 show the invariant mass distributions for each category. Except for region I (Figure 4.5 (a)), there is no significant excess around 91 GeV/c^2 in Figure (b) $\sim$ (d). This indicates that signal events are only located in region I.

We may estimate the number of the background events in region I by

$$N_{bk\_I} = \frac{N_{III}}{N_{IV}} \times N_{II},$$

where N_{bk_I} is the number of background events in region I. N_{II}, N_{III} and N_{IV} are the numbers of events in region II, III and IV, respectively. The number of events in each region of the C-C and C-P categories are shown in Tables 4.3 and 4.4.

Iso_2	Iso_1	
	$Iso_1 < 0.1$	$0.2 < Iso_1 < 0.4$
$Iso_2 < 0.2$	2739	74
$0.2 < Iso_2 < 0.4$	40	67

Table 4.3: The number of events in each category in the C-C events.

Iso_2	Iso_1	
	$Iso_1 < 0.1$	$0.2 < Iso_1 < 0.4$
$Iso_2 < 0.1$	3045	291
$0.2 < Iso_2 < 0.4$	29	38

Table 4.4: The number of events in each category in the C-P events.

From this estimation, we get 44 $\pm$ 10 background events in the C-C and 222 $\pm$ 56 events in the C-P categories. The numbers of estimated background events are consistent with the estimation from the same-sign events.

4.3.3 Comparison of data with background expectations

In the high mass region, the number of background events is too small in the Z' sample to estimate as a function of dielectron invariant mass. To estimate the number of background events as a function of dielectron mass we use the inclusive QCD dijet invariant mass distributions. The events for the dijet invariant mass distributions are required to pass "JET20" trigger. The trigger requires that there is at least one jet whose transverse energy in the $\Delta R = 0.7$ be greater than 20 GeV. The transverse energies of the jet are corrected. Figure 4.6 shows a scatter plot of the corrected and uncorrected E_T of the jet. Typically the jet corrections increase E_T by 25 %. After the energy correction, we require that both of leading two jets have $E_T > 25$ GeV and

the jets are in the fiducial region of either C-C or C-P. The dijet mass distributions are shown in Figure 4.7. The dijet masses above 110 GeV/c^2 are used for the background estimation. We fit the dijet mass distributions with the following function [30]:

$$F(M_{jj}) = \alpha \frac{(1 - \frac{M_{jj}}{\sqrt{s}})^{\beta}}{M_{jj}{}^{\gamma}}, \tag{4.1}$$

where α, β and γ are the free parameters and M_{jj} is the invariant mass of dijet. The result of the fits are also shown in Figure 4.8. Figure 4.9 shows comparisons of QCD dijet mass distributions with background events estimated with the isolation method. The mass distributions of the isolation method background are summed up for regions II, III and IV. The QCD dijet mass distributions are consistent with ones of the isolation method background in the mass range above 110 GeV/c^2 for both C-C and C-P categories. From the isolation method, we find 11.1 $\pm$ 5.0 events in the C-C category and 86.2 $\pm$ 39.4 events in the C-P category.

Figures 4.10 (a) and (b) show the CDF dielectron mass distributions with expected ones from (DY+Z+dijet) Monte Carlo events. The dijet mass distributions in the figures are normalized to the number of events estimated by the isolation method in the mass region above 110 GeV/c^2. The (DY+Z) MC histogram is constrained to the number of events in the Z events in 70 GeV/c^2 < M_{ee} < 110 GeV/c^2. The CDF data is shown with closed circles and the background from (DY+Z+dijet) are shown by curves. The shaded region indicates the dijet contribution. The observed C-C and C-P dielectron mass distributions agree with the (DY+Z+dijet) background estimations. Figure 4.11 shows the C-C and C-P combined result. Table 4.5 shows the number of observed events, the expected number from Drell-Yan production and also the sum of Drell-Yan and the QCD dijet background estimates for various mass ranges. The CDF data in the high mass region are in reasonable agreement with (DY+Z+Dijet) estimations.

Mass GeV/c^2	(DY+Z) MC		Dijet		DY+Z+Dijet		CDF Data	
	C-C	C-P	C-C	C-P	C-C	C-P	C-C	C-P
M > 150	15.5	15.3	3.1	34.1	18.6	49.4	26	44
M > 200	6.0	4.8	0.8	10.1	6.8	14.9	8	11
M > 250	2.7	1.8	0.3	3.2	3.0	5.1	3	6
M > 300	1.3	0.8	0.1	1.1	1.4	1.9	2	4
M > 350	0.7	0.3	0	0.4	0.7	0.7	2	0
M > 400	0.4	0.2	0	0.1	0.4	0.3	1	0
M > 450	0.2	0.1	0	0.1	0.2	0.1	1	0
M > 500	0.1	0.0	0	0	0.1	0.1	1	0
M > 550	0.1	0.0	0	0	0.1	0	0	0
M > 600	0.0	0.0	0	0	0	0	0	0

Table 4.5: Data compared with the expected number of events from the Drell-Yan Monte Carlo + background events.

4.3.4 Z boson cross section

As another cross check of this study, the Z boson cross section times branching ratio decaying into electron pairs are calculated with the number of observed dielectron candidate events and with the efficiencies described in the previous section. The Z boson candidates from the Z' search sample are selected by requiring that the dielectron invariant mass should be between 70 GeV/c^2 and 110 GeV/c^2. With this requirement, a sample of 5492 Z's is obtained (2630 of these are C-C events and 2862 are C-P events). The geometrical acceptances at the Z boson mass ($M_Z = 91.0$ GeV/c^2) are 15.3% for C-C, and 18.2% for C-P events. In the efficiencies of the event selection cuts described above, $\varepsilon^{c-c}_{total}$(at $M_{ee} = M_Z$) is 13.5% and $\varepsilon^{c-p}_{total}$(at $M_{ee} = M_Z$) is 14.3%. In the mass region of $70 < M_{ee} < 110$ GeV/c^2, 31 ± 9 fake dielectron events in C-C category and 112 ± 40 events in C-P category are expected with the isolation method. Integrated luminosity for this calculation is 90.2 ± 7.2 pb^{-1}. These parameters are summarized in Table 4.6. Subtracting the expected background events, the Z cross sections for C-C and C-P categories are obtained. The results are shown in Table 4.7. The first error is statistical, the second error reflects the uncertainty in event selection efficiency, and the third one corresponds to the luminosity uncertainty of 8%. The Z boson cross sections agree with the CDF result [29] within errors.

Category	Geometrical Acceptance	Efficiency	Observed Events	Estimated Background Events	Integrated Luminosity (pb^{-1})
C-C	$15.3 \pm 0.7\%$	$13.5 \pm 0.4\%$	2630	31 ± 9	90.2 ± 7.2
C-P	$18.2 \pm 1.7\%$	$14.3 \pm 0.5\%$	2862	112 ± 40	

Table 4.6: Parameters for the Z boson cross section.

Category	Z boson cross section (pb)
C-C	$215 \pm 4 \pm 7 \pm 17$
C-P	$200 \pm 4 \pm 7 \pm 16$

Table 4.7: Z boson cross sections for the C-C and C-P categories.

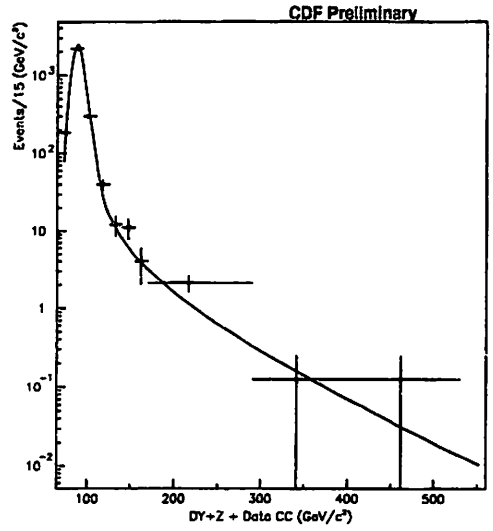

4.1 - (a) C-C events

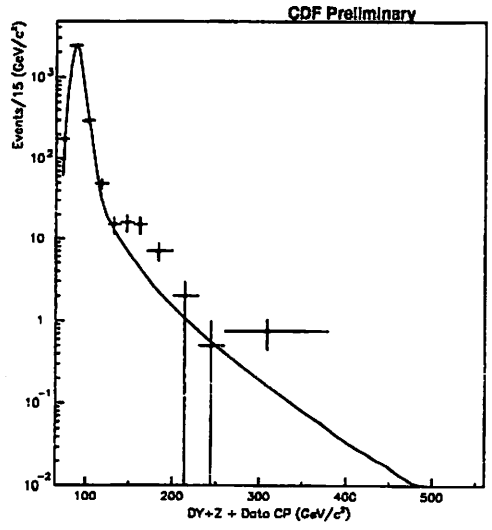

4.1 - (b) C-P events

Figure 4.1: Figure (a) shows a comparison of data with Drell-Yan events for the C-C category and Figure (b) shows the same comparison for C-P events. Plots with error bar indicate the CDF data points and curves indicate the estimated Drell-Yan events.

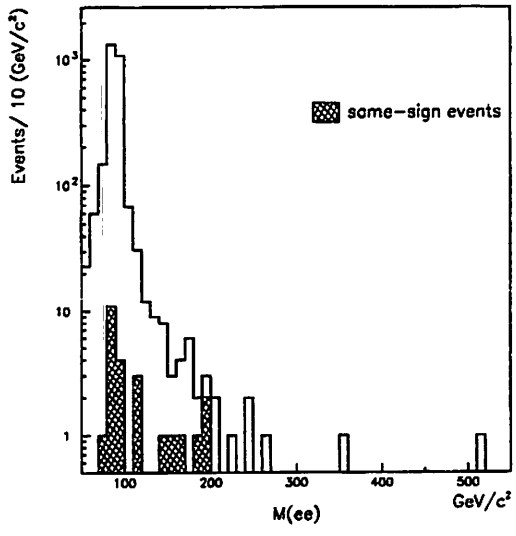

4.2 - (a) C-C events

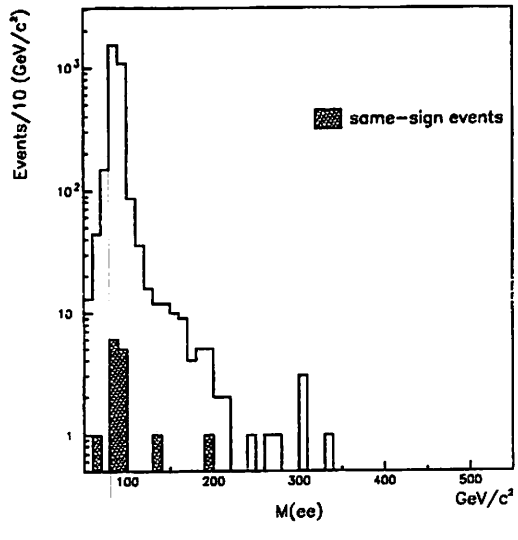

4.2 - (b) C-P events

Figure 4.2: Shaded histograms indicate the invariant mass distributions of the same-sign events.

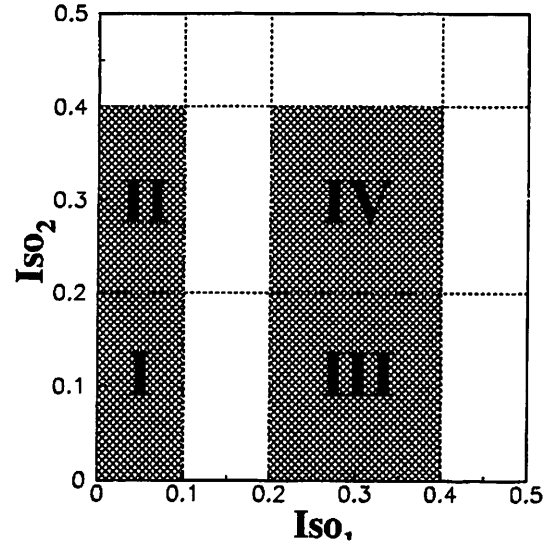

4.3 - (a) Categories for the C-C events.

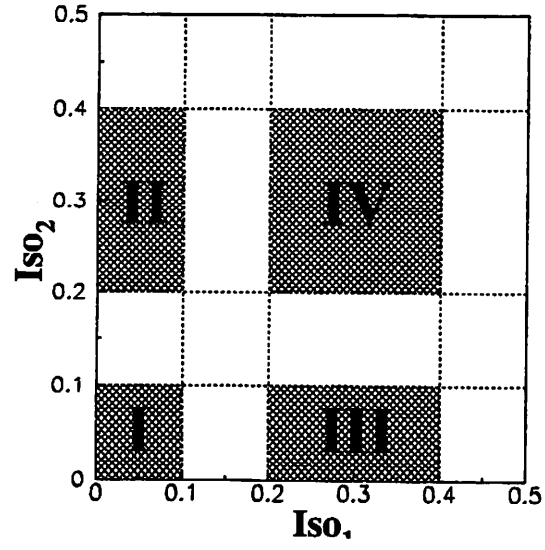

4.3 - (b) Categories for the C-P events.

Figure 4.3: Figures (a) and (b) show categorizations of events for the C-C and C-P events.

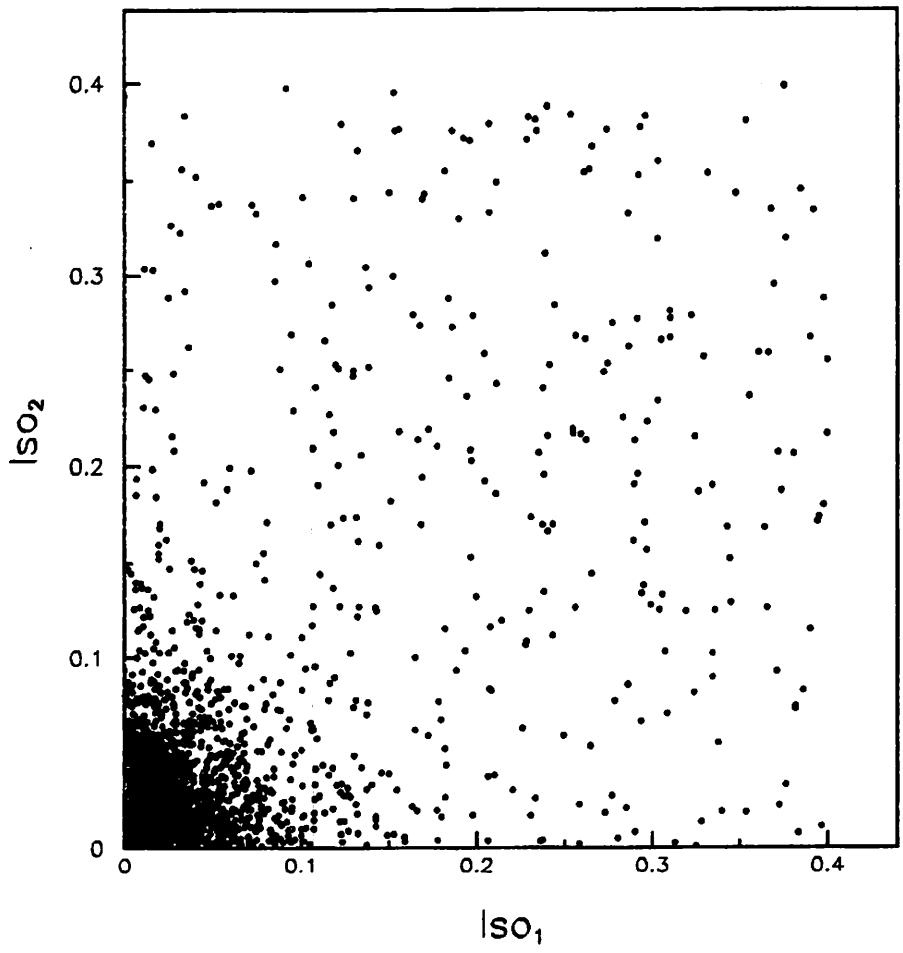

Figure 4.4: Isolation of the first electron candidate(Iso_1) vs Isolation of the second electron candidate(Iso_2).

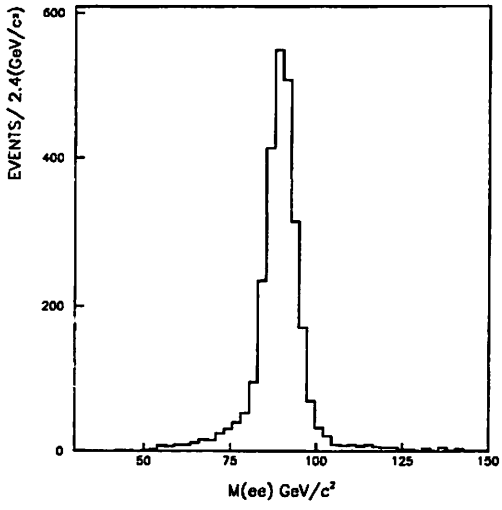

4.5 - (a) $Iso_1 < 0.1$, $Iso_2 < 0.2$

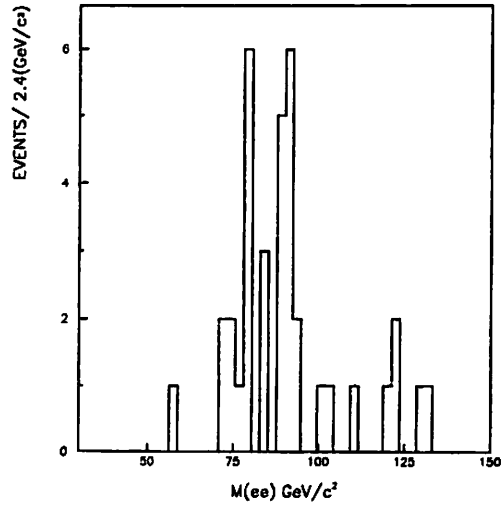

4.5 - (b) $Iso_1 < 0.1$, $Iso_2 > 0.2$

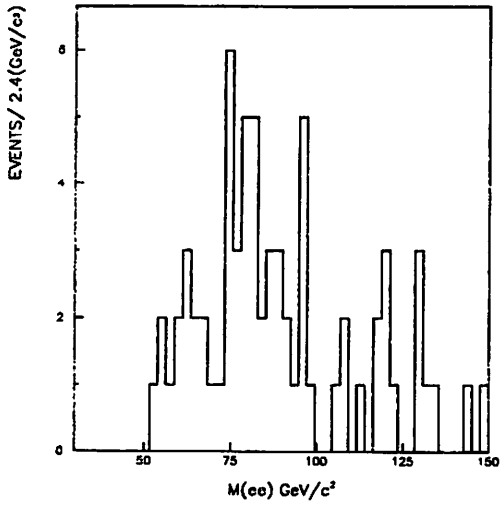

4.5 - (c) $Iso_1 > 0.2$, $Iso_2 < 0.2$

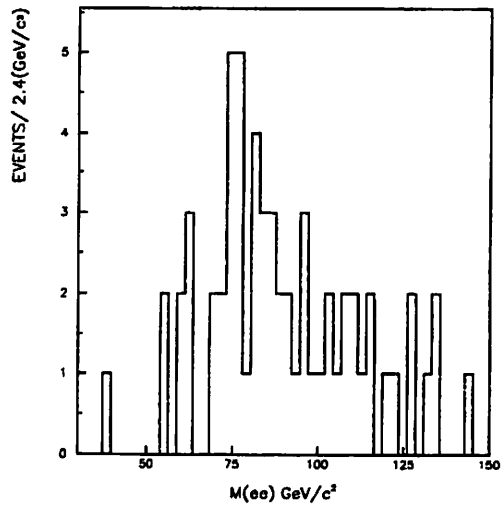

4.5 - (d) $Iso_1 > 0.2$, $Iso_2 > 0.2$

Figure 4.5: Invariant mass distributions for each category.

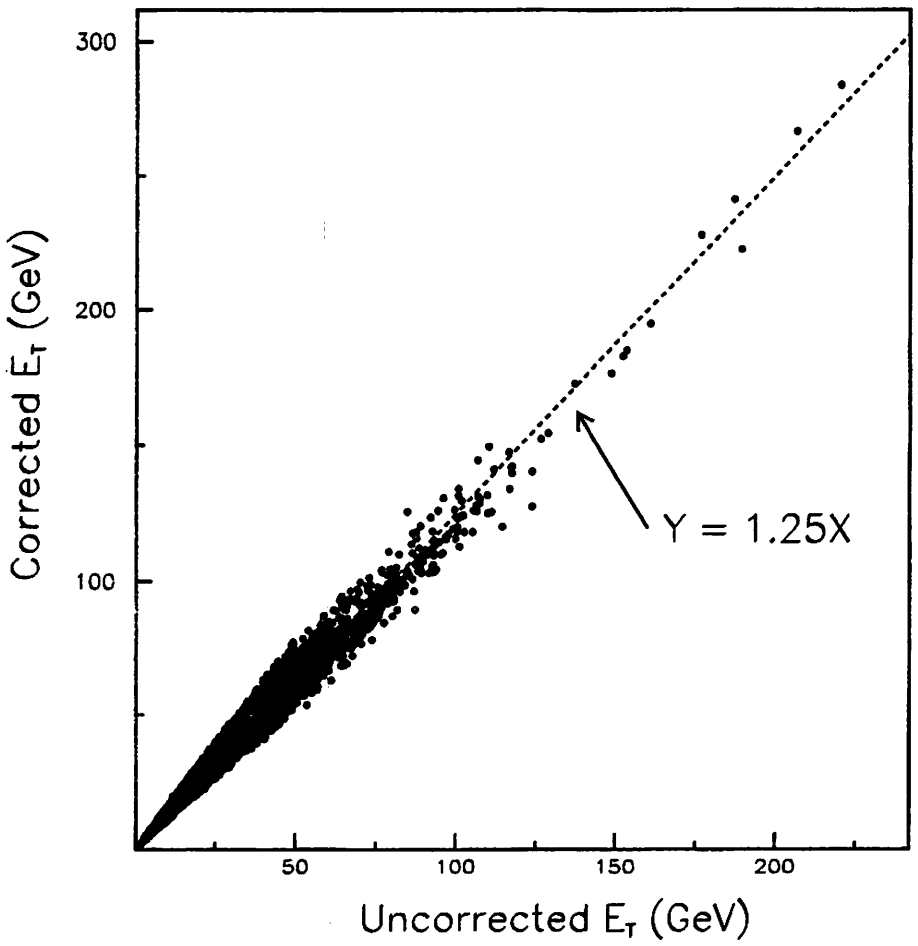

Figure 4.6: The scatter plot of the corrected and uncorrected jet E_T.

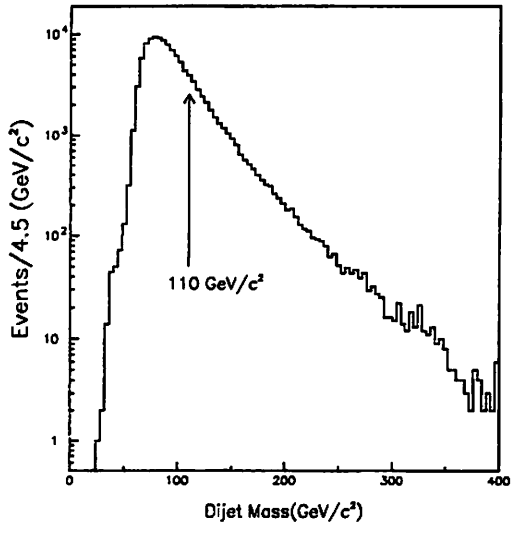

4.7 - (a) C-C dijet mass distribution

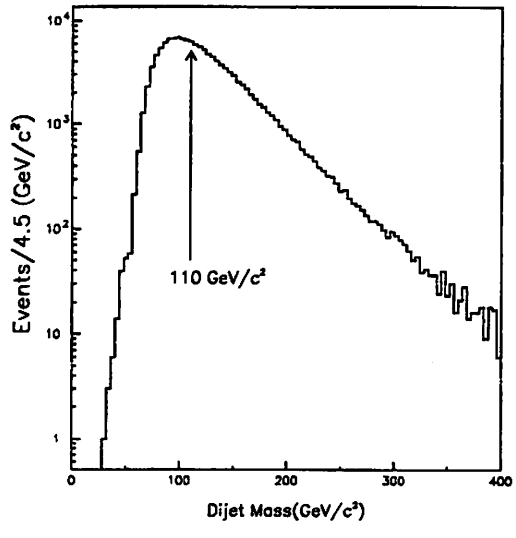

4.7 - (b) C-P dijet mass distribution

Figure 4.7: Figures (a) and (b) show dijet mass distributions for the C-C and C-P categories.

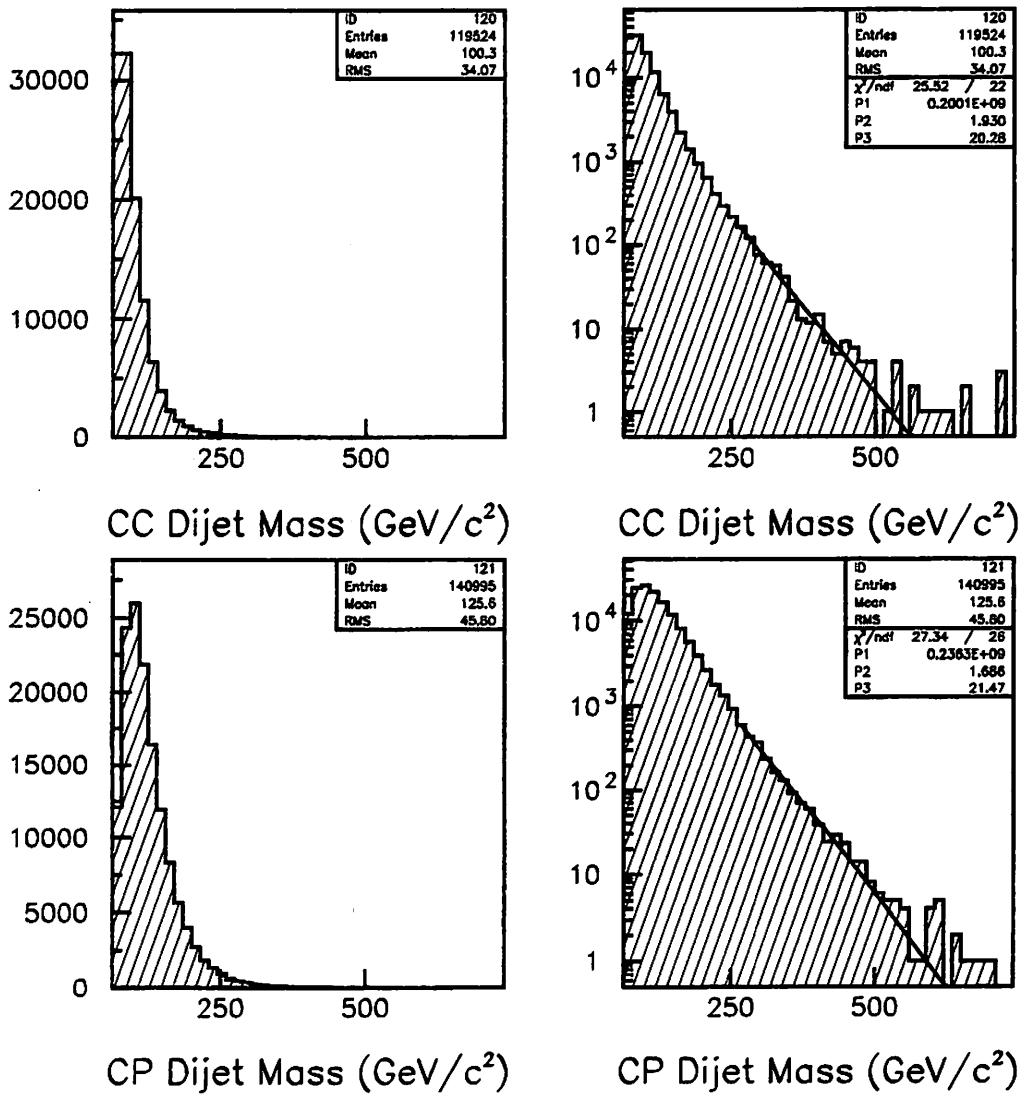

Figure 4.8: Top two figures show dijet mass distributions compared to the fit in a linear and log scales for C-C events. Bottom two figures are the same plots for C-P events. Fitted dijet mass distribution function is

$$F(M_{jj}) = \alpha \frac{(1 - \frac{M_{jj}}{\sqrt{s}})^{\beta}}{{M_{jj}}^{\gamma}},$$

where α = P1, β = P2 and γ = P3.

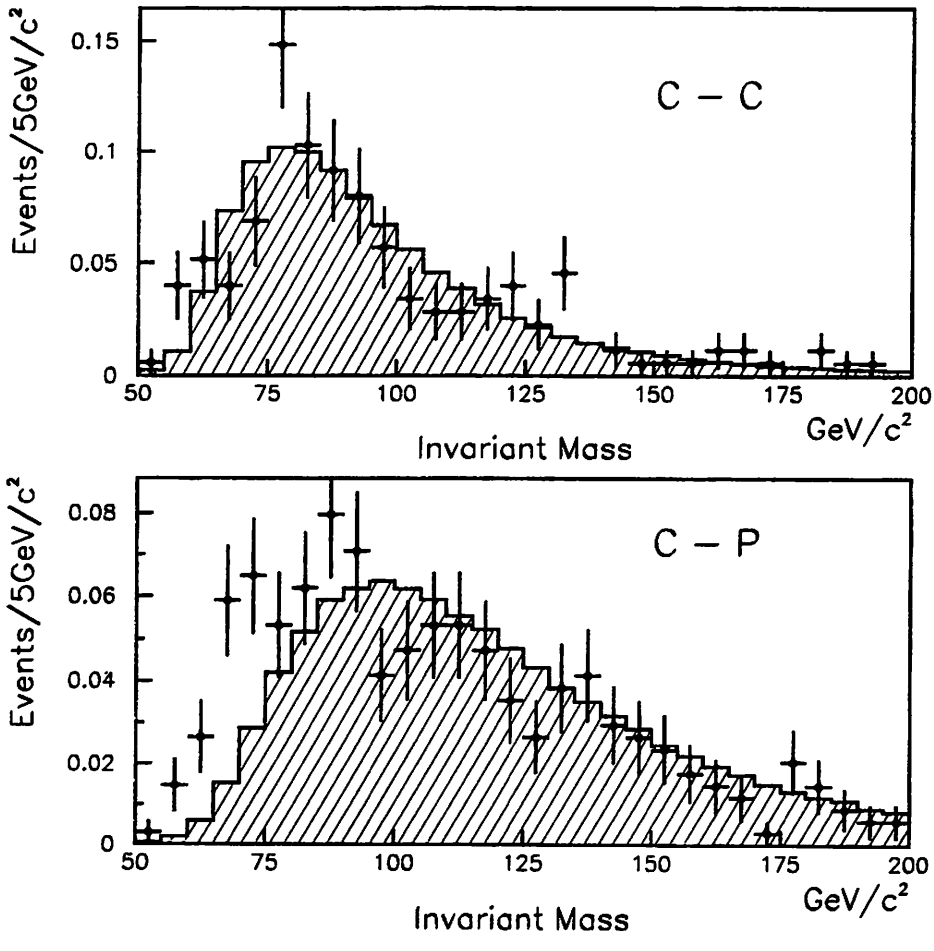

Figure 4.9: The comparisons of the QCD dijet mass distributions with the background mass distributions of the isolation method for C-C and C-P events. Shaded histograms are the QCD dijet mass distributions and plots are the isolation method background events.

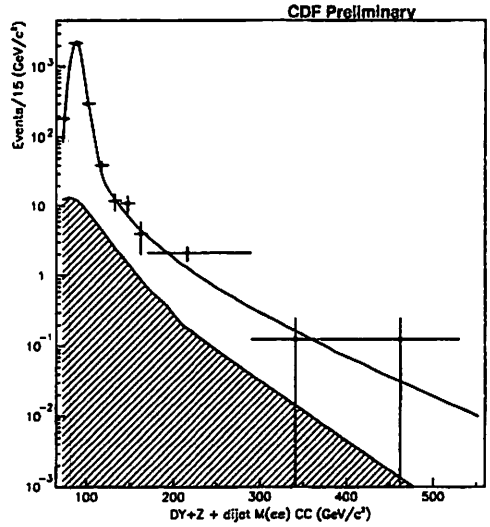

4.10 - (a) C-C events

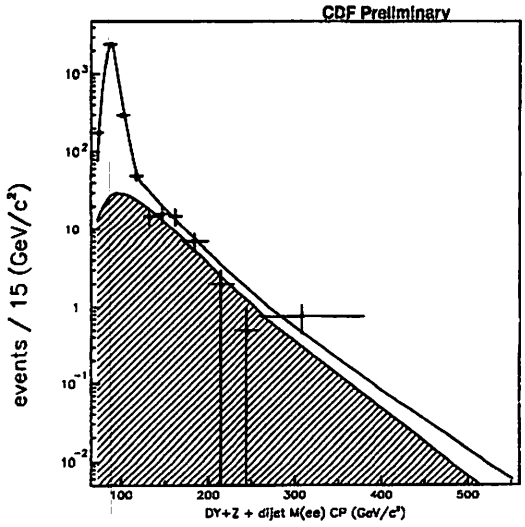

4.10 - (b) C-P events

Figure 4.10: Figures (a) and (b) show the comparisons of dielectron mass distribution with the estimated DY+Z+dijet events for the C-C and C-P Z' search sample, separately. Closed circles with error bar are the CDF data points. The shaded area shows the expected dijet background events. The upper curve is the estimated background(DY+Z+dijet) events.

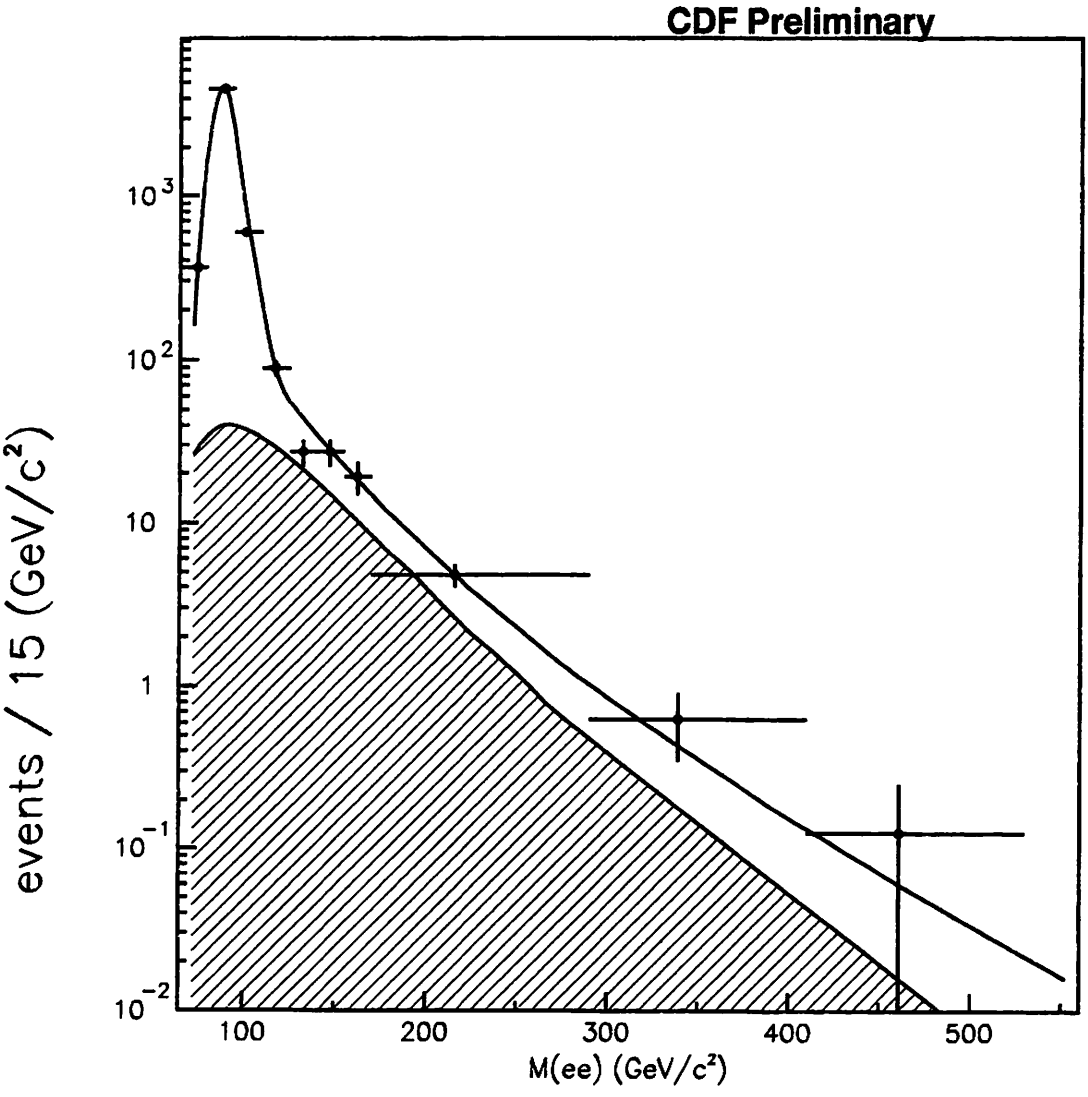

Figure 4.11: The dielectron mass distribution compared with the estimated DY+Z+dijet events for the total (C-C+C-P) Z' search sample. Closed circles with error bar are the CDF data points. The shaded area shows the expected dijet background events. The upper curve is the expected background(DY+Z+dijet) events.

Chapter 5

Mass limit on the Z' bosons

In the previous chapter, we concluded that we observe high mass dielectron events at a rate expected from background processes. In this chapter, we set upper limits on the Z' cross section times branching ratio decaying into dielectrons ($\sigma \cdot Br(e^+e^-)$) as a function of the invariant mass of Z'. We can place an upper limit on the number of $Z'(\rightarrow e^+e^-)$ events using observed dielectron events. The upper limit on the number of Z' events can be translated to an upper limit on the Z' production cross section times branching ratio by the equation,

$$\sigma_{Z'} \cdot Br(Z' \rightarrow e^+e^-) = \frac{N}{\mathcal{L} \times \varepsilon_{total}(M_{Z'})}, \tag{5.1}$$

where Br is the branching ratio to dielectron channel, N is number of events, $\mathcal{L}$ is the integrated luminosity, and $\varepsilon_{total}(M_{Z'})$ is the total detection efficiency. Systematic uncertainty associated with the luminosity measurement is estimated to be 8% [23]. As described in the following section, this uncertainty is the largest among all the systematic uncertainties in the limit calculations.

In order to avoid the effect of uncertainty from the luminosity measurement, we do the following modifications of Equation 5.1. Equation 5.1 can be modified to a formula which does not include the integrated luminosity term. The Z boson cross section can be expressed in the same way as

$$\sigma_Z \cdot Br(Z \rightarrow e^+e^-) = \frac{N_Z}{L \times \varepsilon_{total}(M_{Z'})}. \tag{5.2}$$

Taking ratio of Equations 5.1 and 5.2, we obtain

$$\sigma_{Z'} \cdot \mathrm{B}(Z' \rightarrow e^+e^-) = \sigma_Z \cdot Br(Z \rightarrow e^+e^-) \times \frac{\frac{N_{Z'}}{\varepsilon_{total}(M_{Z'})}}{\frac{N_Z}{\varepsilon_{total}(M_Z)}}. \tag{5.3}$$

Since we know the overall efficiencies ($\varepsilon_{total}(M_Z)$, $\varepsilon_{total}(M_{Z'})$) (see Figure 3.14), the Z cross section and N_Z, $\sigma_{Z'} \cdot \mathrm{B}(Z' \to e^+e^-)$ is only a function of $N_{Z'}$.

In the first section, the systematic uncertainties are described. Assuming that the coupling strengths of Z' are the same as those of Z boson, a calculation of lower Z' mass limit is described in Section 5.1. Section 5.2.1 discusses the procedure of setting the $\sigma_{Z'} \cdot \mathrm{B}(Z' \to e^+e^-)$ limit, and Section 5.2.2 describes a calculation of Z' mass limit assuming that the coupling strengths of Z' to quarks and leptons are the same as those of Z boson. Lower limits on the Z' mass for various other Z' models at 95% C.L. are described in Section 5.2.3.

5.1 Systematic uncertainties

The systematic uncertainties are discussed in this section. The systematic uncertainties considered in this study are:

1. uncertainties in the acceptance calculation.
   (a) uncertainty due to the P_T of Z'.
   (b) uncertainty due to the choice of the parton distribution functions (PDF).
2. uncertainty due to the efficiency of event selection cuts.
3. uncertainty due to the background estimation.

5.1.1 Uncertainties in the acceptance calculation

Uncertainty due to the P_T of the Z' bosons

The geometrical and kinematical acceptance was calculated with the Monte Carlo simulation described in Section 3.3.4. In the program, a P_T of the boson was given according to the measured P_T distribution of Z boson. In order to estimate systematic uncertainty due to the P_T distribution of the boson, the measured slope of the P_T distribution is changed by $\pm 10\%$. Trying these shapes for the P_T choice, we find 1.6% of variation in the acceptance.

Uncertainty due to the choice of parton distribution functions

We employ different sets of PDF's to estimate the systematic uncertainty due to the parton distribution functions. Table 5.1 shows differences in the acceptance from MRSD$-'$. A systematic uncertainty of 1.1 % due to the different PDF in the

Parton Distribution Function	Difference
MRSA	0.7 %
HMRSE	0.7 %
CTEQ2PL	1.1 %
CTEQ2M	0.7 %
CTEQ2ML	1.1 %
GRV94LO	0.7 %

Table 5.1: Systematic uncertainties due to different parton distribution functions.

acceptance is assigned.

Another systematic uncertainty due to statistical error of the Monte Carlo acceptance calculation is 0.4% in the mass range above 250 GeV/c^2.

5.1.2 Other systematic uncertainties

Uncertainty due to the efficiency of event selection cuts

A systematic uncertainty due to the efficiency of event selection cuts is 0.8%. This uncertainty is caused by statistical uncertainties in the control data sample which was used to study the electron identification cuts and the topological cuts.

Uncertainty due to the background estimation

As we described in Section 4.3.4, 143 $\pm$ 49 background events are expected in the Z boson mass region (70 GeV/c^2 < M_{ee} < 110 GeV/c^2). A systematic uncertainty due to the statistical errors of background subtraction in the Z mass region is 1.5%.

In total, we assign 2.6% of the total systematic uncertainty which is obtained by adding these uncertainties in quadrature.

5.2 Z' Mass Limits

5.2.1 Procedure for setting limit

With Equation 5.3, a 95% C.L. limit on the number of Z' events can be translated to the 95% C.L. limit on the Z' production cross section. The 95% C.L. limit on the number of Z' events is obtained by comparison of observed dielectron invariant mass distribution to the sum of the Monte Carlo Z' production and the Drell-Yan + Z (DY+Z) continuum. The dijet type background events are not taken into account in this comparison. There are two reasons:

- In the dielectron mass region above 250 GeV/c^2, we expected very small contributions from dijet background.
- Uncertainty associated with estimating amount of dijet background for $M_{ee} > 110$ GeV/c^2 is fairly large ($\sim 20\%$).

We take a conservative approach and decide not to subtract dijet background to obtain the $\sigma_{Z'} \cdot \mathrm{B}(Z' \rightarrow e^+e^-)$ limit.

We assume that the dielectron sample contains only DY+Z and possible Z' events so that the dielectron invariant mass distribution of the observed events is given by

$$\frac{dN}{dM_{ee}} = \alpha Z'(M_{ee}) + \beta Z \cdot DY(M_{ee}), \tag{5.4}$$

where $Z'(M_{ee})$ and $Z \cdot DY(M_{ee})$ are the theoretical dielectron mass distributions for Z' and DY+Z events, respectively. α and β are coefficients. The function $Z'(M_{ee})$ varies as a function of the Z' mass and a probability distribution is calculated for each Z' mass. Standard model couplings are assumed in generating Z' events and the Z' width is set equal to the Z^0 width scaled by $M_{Z'}/M_{Z^0}$. To calculate the branching ratio to dielectrons we have assumed a top mass of 174 GeV/c^2. Figure 5.1 shows the invariant mass distributions of $Z' \rightarrow e^+e^-$ events generated with the Monte Carlo simulation and the energy smearing program.

A binned maximum-likelihood method is used with the contents of the bins treated with Poisson statistics [31][32]. The probability associated with the ith bin is

$$P_i(k_i, m_i) = \frac{m_i^{k_i} e^{-m_i}}{k_i!}, \tag{5.5}$$

where k_i is the number of events observed in the ith bin, m_i is the number of events expected in the ith bin:

$$m_i \stackrel{\text{def}}{=} \alpha Z'_i + \beta Z \cdot DY_i, \tag{5.6}$$

with Z'_i and $Z \cdot DY_i$ the number of events predicted in the ith bin by the Z' and $Z \cdot DY$ Monte Carlo's, respectively. The likelihood function is defined as the total probability, which is the product of the individual probabilities for each bin,

$$\mathcal{L}(\alpha, \beta) \stackrel{\text{def}}{=} P = \prod_{i=1}^{N} P_i(k_i, m_i) = \prod_{i=1}^{N} \frac{m_i^{k_i}}{k_i!} e^{-m_i}, \tag{5.7}$$

where N is the total number of bins.

In order to reduce a two-dimensional likelihood function $\mathcal{L}(\alpha, \beta)$ to a one-dimensional one, the Monte-Carlo DY+Z prediction is normalized to the data in the region of the Z boson mass (70 GeV/c^2 < M_{ee} < 110 GeV/c^2). Thus the coefficient for the DY+Z, β is obtained by

$$\beta = \frac{Z_{Data}}{Z_{MC}}. \tag{5.8}$$

It is more convenient to get $\sigma_{Z'} \cdot \mathrm{B}(Z' \to e^+e^-)$ (95% C.L.) with a normalized likelihood function which is normalized to an area of 1.0 over the range of positive α. Hence Equation 5.7 can be written as

$$L(\alpha) \stackrel{\text{def}}{=} f_{norm} \cdot \mathcal{L}(\alpha) = f_{norm} \cdot \prod_{i=1}^{N} \frac{m_i^{k_i}}{k_i!} e^{-m_i}, \tag{5.9}$$

where f_{norm} is a normalization factor defined by

$$\int_0^{+\infty} L(\alpha)\, d\alpha = f_{norm} \cdot \int_0^{+\infty} \mathcal{L}(\alpha)\, d\alpha = 1.0. \tag{5.10}$$

Figure 5.2 shows a typical likelihood distribution as a function of α. The 95% C.L. upper limit on $\alpha(\equiv \alpha_{95\%})$ is calculated by

$$\int_0^{+\alpha_{95\%}} L(\alpha)\, d\alpha = 0.95. \tag{5.11}$$

Before extracting 95% C.L. limits on the Z' cross section from $L(\alpha)$, we must convolute this likelihood function with a smearing factor which we take to be a Gaussian with a width equal to the total systematic uncertainty $\sigma(\alpha)(= 2.6\%)$ obtained in the

previous section. The likelihood function smeared according to the total systematic uncertainty is defined as

$$\hat{L}(\hat{\alpha}) \stackrel{\text{def}}{=} \int_0^{+\infty} L(\alpha) \frac{e^{-\frac{1}{2}\frac{(\hat{\alpha}-\alpha)^2}{\sigma(\alpha)^2}}}{\sqrt{2\pi\cdot\sigma(\alpha)^2}} d\alpha. \tag{5.12}$$

A simple Monte Carlo program is used for this smearing of the likelihood function. First, a value of α, called α_0, is generated from the parent likelihood distribution. Then the smearing due to $\sigma(\alpha)$ is applied by adding a random number to α_0, whose parent distribution is a Gaussian with a mean of one and standard deviation of $\sigma(\alpha)$. This procedure is repeated one million times, yielding the smeared likelihood function for a given Z' mass. Figure 5.3 shows a typical smeared likelihood function as a function of α. The function is smeared one of Figure 5.2. The smeared function is then integrated over the range $0 < \hat{\alpha} < \infty$ and normalized to unity. The normalized function is used to determine the value of $\hat{\alpha}$, denoted $\hat{\alpha_{95\%}}$, above which we find 5% of the area under the probability curve. Figure 5.4 shows an integrated likelihood function for a typical one. The arrow indicates $\hat{\alpha_{95\%}}$.

The 95% C.L. lower limit on the number of Z' events (N_{95}) is obtained by

$$N_{95} = \hat{\alpha_{95\%}} \times Z'(M_{ee}). \tag{5.13}$$

Then it can be translated to the 95% C.L. limit on the Z' production cross section times branching ratio with Equation 5.3. The observed number of Z events in Equation 5.3, N_Z, is the same number of generated Z events with Equation 5.8. With Equation 5.13 and 5.1, Equation 5.3 can be modified as

$$\begin{aligned} \sigma_{Z'} \cdot \mathrm{B}(Z' \to e^+e^-) &= \frac{\sigma_Z^{MC} \cdot Br^{MC}}{\frac{N_Z^{MC}}{\epsilon_{total}(M_Z)}} \times \frac{N_{Z'}}{\epsilon_{total}(M_{Z'})}, \\ &= \frac{\sigma_Z^{MC} \cdot Br^{MC}}{\frac{N_Z^{MC}}{\epsilon_{total}(M_Z)}} \times \frac{N_{95}}{\epsilon_{total}(M_{Z'})}, \end{aligned} \tag{5.14}$$

where $\sigma_z^{MC} \cdot Br^{MC}$ is the cross section used in the Monte Carlo program and N_z^{MC} is the number of events expected in the Monte Carlo program. Using Equation 5.14, a systematic uncertainty in the Z boson cross section can be removed.

5.2.2 Z' mass limit assuming standard model coupling strengths

The 95% C.L. limit on $\sigma_{Z'} \cdot \mathrm{B}(Z' \to e^+e^-)$ is shown in Figure 5.5 as a function of the Z' mass. The top solid line is the predicted $\sigma_{Z'} \cdot \mathrm{B}(Z' \to e^+e^-)$ using MRSD$-'$ structure function and standard model couplings. The middle dot-dashed line is the $\sigma_{Z'} \cdot \mathrm{B}(Z' \to e^+e^-)$ with data of the 1992-1993 run, already published[10]. The bottom line is the $\sigma_{Z'} \cdot \mathrm{B}(Z' \to e^+e^-)$ with data of the 1994-1995 run. The intersections of the predicted curve and 95% C.L. limit curves determine the 95% C.L. lower limits on the Z' mass. With data of the 1994-1995 run only, a lower limit on the Z' mass is extended to 640 GeV/c^2 from 505 GeV/c^2. Figure 5.6 shows the result with combined 1992-1993 and 1994-1995 data. The 95% C.L. upper limit on the $\sigma_{Z'} \cdot \mathrm{B}(Z' \to e^+e^-)$ with the combined data is set as a function of the dielectron invariant mass. In the region of mass above 650 GeV/c^2, the upper limit of the $\sigma_{Z'} \cdot \mathrm{B}(Z' \to e^+e^-)$ is set to be 6×10^{-2} pb. We also set a lower limit on the Z' mass of 655 GeV/c^2 with the combined data.

5.2.3 Z' mass limits for various models

We also derive 95% C.L. limits on the mass of Z' for several E_6 models and a right-handed Z' in the alternative left-right model (ALRM). Model differences may affect the $\sigma_{Z'} \cdot Br(Z' \to e^+e^-)$ limit. To cover a representative range of the Z' width ($\Gamma_{Z'}$) values, we consider models based on the E_6 symmetry group. In this calculations, we assume that the Z' decays only to standard model fermions. These models predict narrower widths than that expected for standard model couplings ($\Gamma^{SM}_{Z'}$),

$$\begin{aligned} \Gamma_{Z'} &< \Gamma^{SM}_{Z'}, \\ \Gamma_{Z'} &= \alpha \times \Gamma^{SM}_{Z'}. \end{aligned} \tag{5.15}$$

Figure 5.7 (a) shows dielectron invariant mass distributions ($M_{z'} = 600\mathrm{GeV}/c^2$) for $\alpha = 0.16$ and 1.00 with energy smearing.

Figure 5.7 (b) shows 95% C.L. limits on $\sigma_{Z'} \cdot \mathrm{B}(Z' \to e^+e^-)$ for $\alpha = 0.16$ and 1.00. We conclude that using $\Gamma^{SM}_{Z'}$ results in conservative Z' limits.

Figure 5.8 shows our 95% C.L. limit curve together with the predictions from several E_6 models and with the prediction of a right-handed Z' in the alternative

left-right model (ALRM). The solid line in each plot corresponds to the model's prediction. From intersections of the solid and dashed curves in each plot we set the lower mass limits for Z_χ, Z_ψ, Z_η, Z_I, Z_{LR} and Z_{ALRM} to be 530, 520, 550, 505, 585 and 525 GeV/c^2, respectively, for those cases when the Z' boson decays only to known particles. All these models predict new fermions. Allowing Z' to decay to the new fermions would make worse the mass limits quoted.

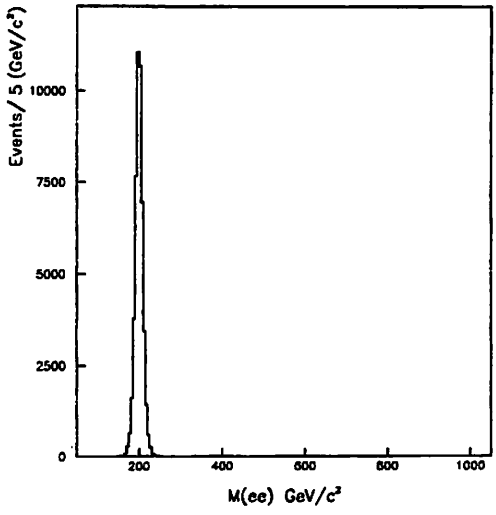

5.1 - (a) $M_{Z'} = 200$ GeV/c^2

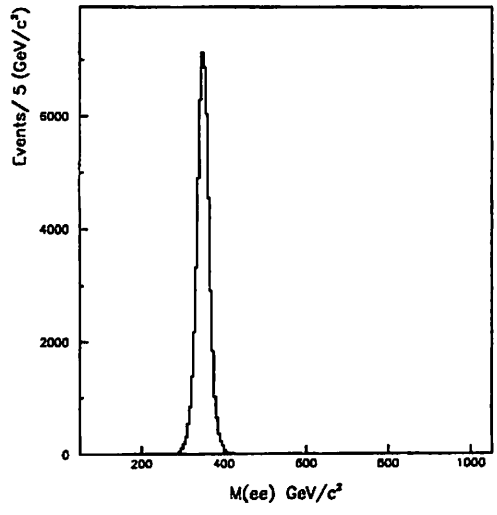

5.1 - (b) $M_{Z'} = 350$ GeV/c^2

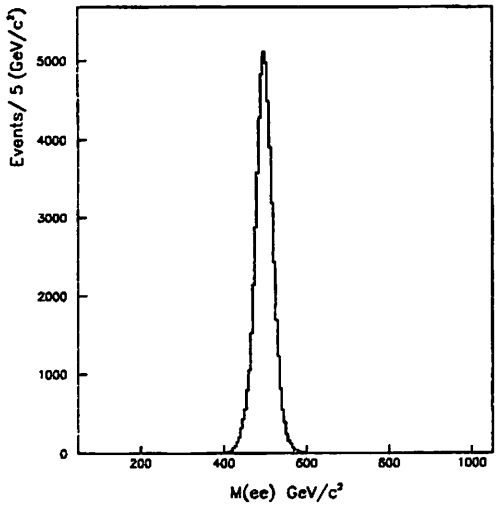

5.1 - (c) $M_{Z'} = 500$ GeV/c^2

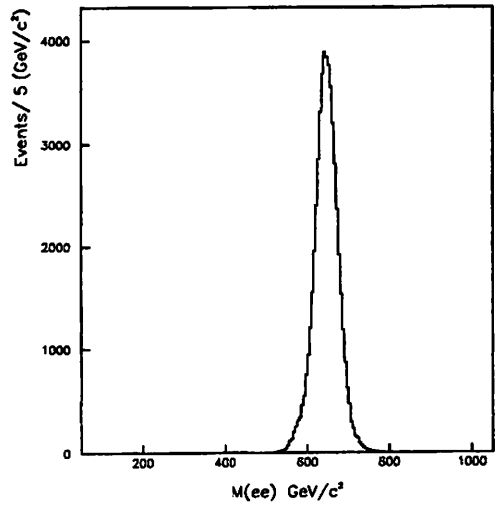

5.1 - (d) $M_{Z'} = 650$ GeV/c^2

Figure 5.1: Dielectron invariant mass distributions of $Z' \rightarrow e^+e^-$ events.

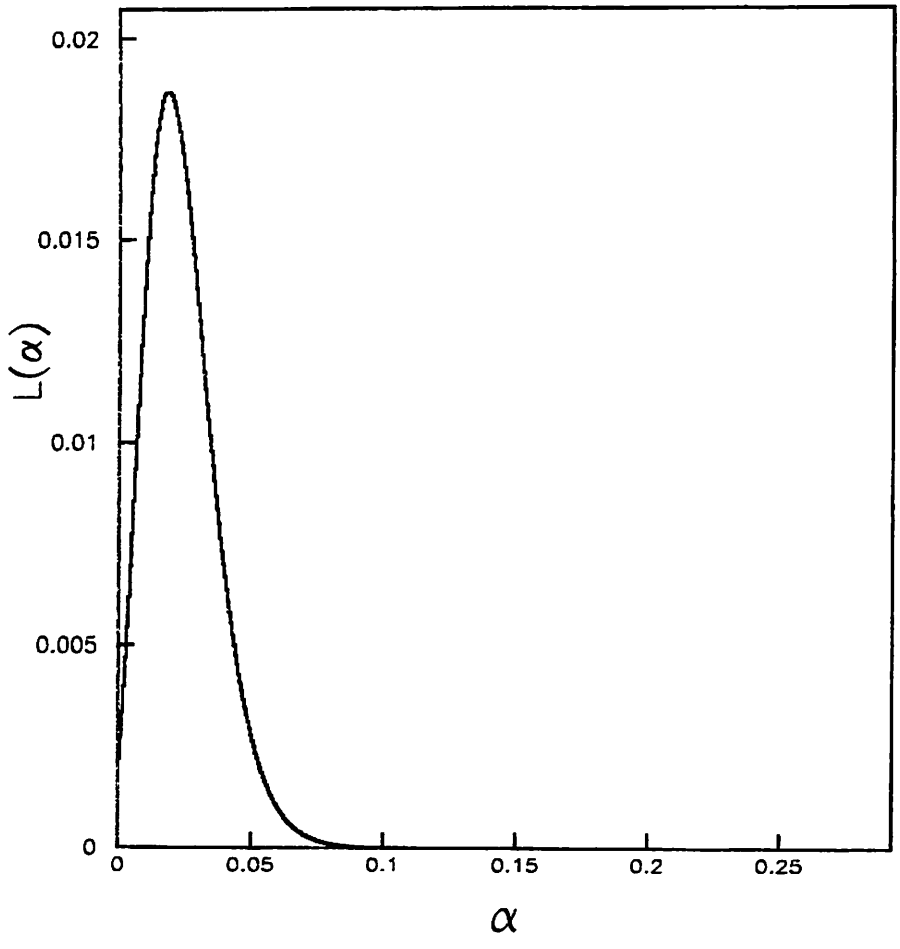

Figure 5.2: A typical likelihood distribution as a function of α.

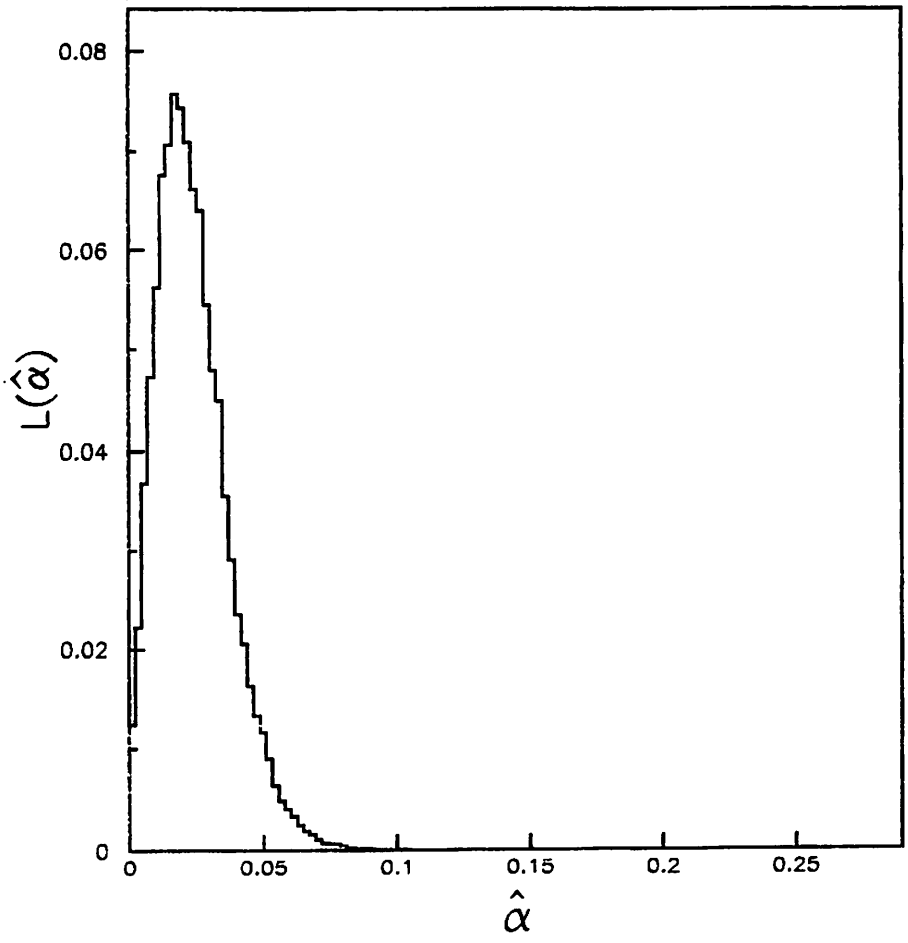

Figure 5.3: A smeared likelihood distribution as a function of $\hat{\alpha}$.

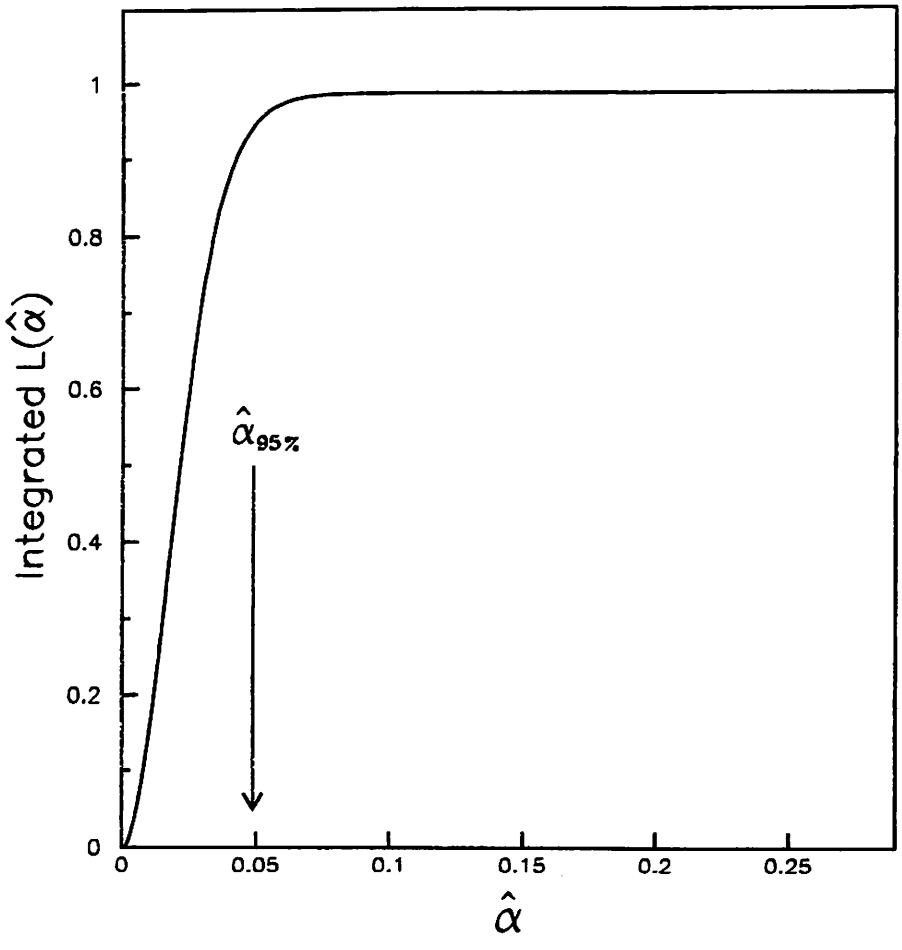

Figure 5.4: An integral likelihood distribution as a function of $\hat{\alpha}$. The arrow indicates the point of $\hat{\alpha}_{95\%}$.

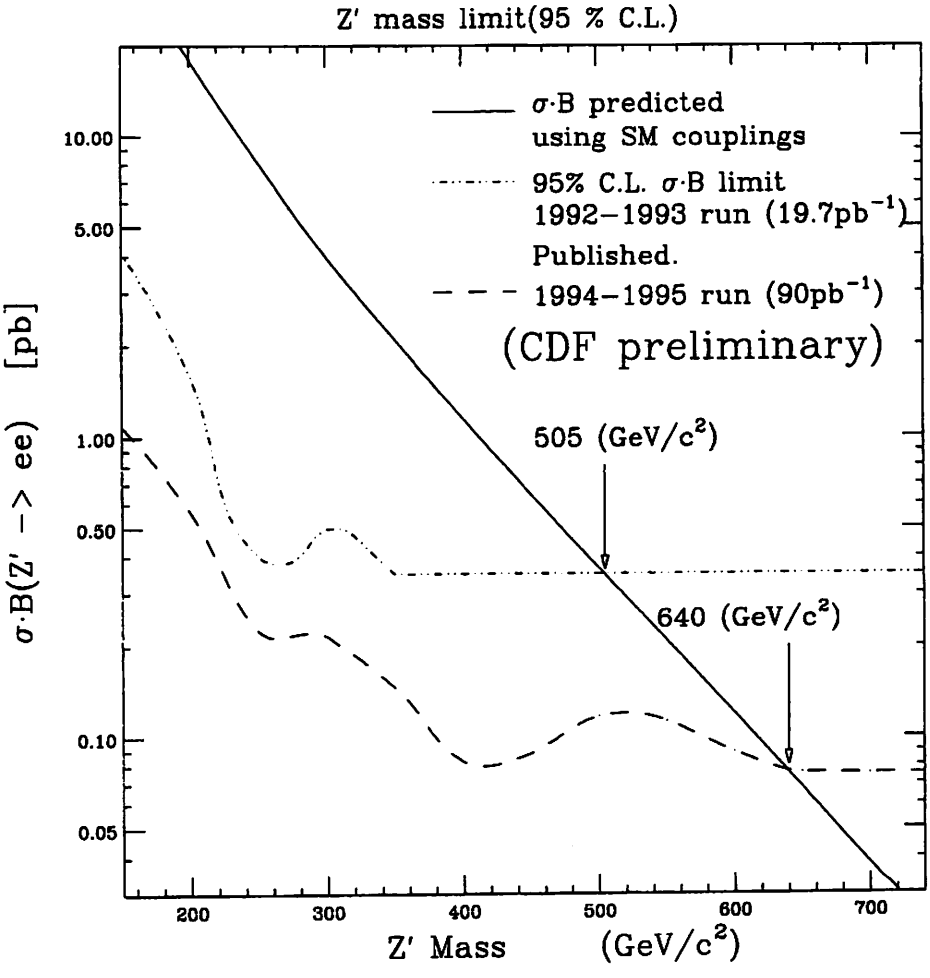

Figure 5.5: A Z' 95 % C.L. limit on $\sigma_{Z'} \cdot \mathrm{B}(Z' \to e^+e^-)$ for a Z' decaying into a dielectron as a function of the dielectron invariant mass. We set a 95% C.L. lower bound on the mass of the Z' to be 640 GeV/c^2 using 1994-1995 data assuming the standard coupling strengths.

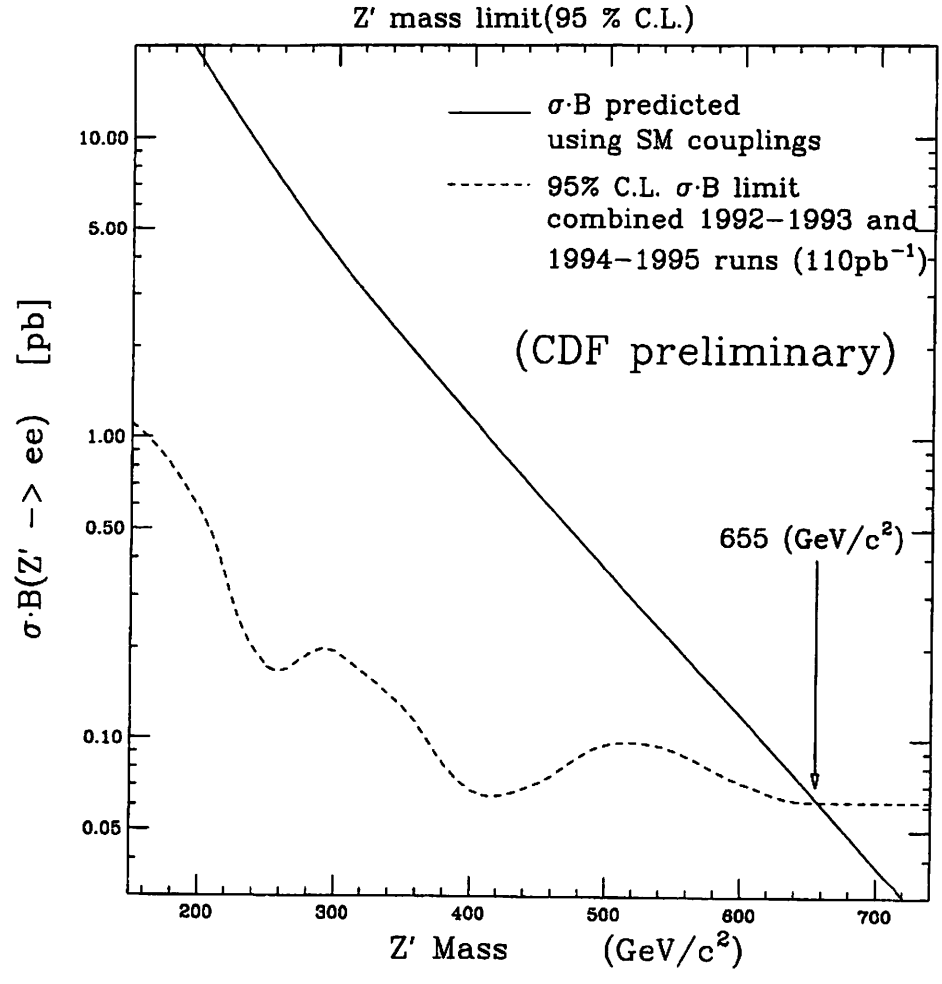

Figure 5.6: A Z' 95 % C.L. limit on $\sigma_{Z'} \cdot \mathrm{B}(Z' \rightarrow e^+e^-)$ for a Z' decaying into a dielectron as a function of the dielectron invariant mass. We set a 95% C.L. lower bound on the mass of the Z' with combined data of 1992-1993 and 1994-1995 runs (integrated luminosity = 110 pb^{-1}). A 95% C.L. lower limit on Z' mass is set to be 655 GeV/c^2.

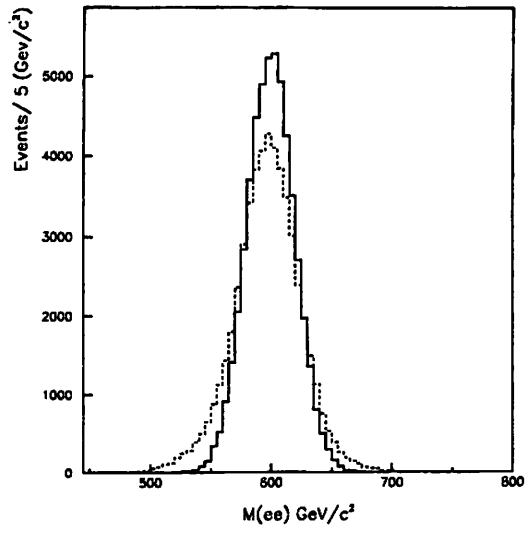

5.7 - (a) Dielectron invariant mass distributions for different $\Gamma_{Z'}$.

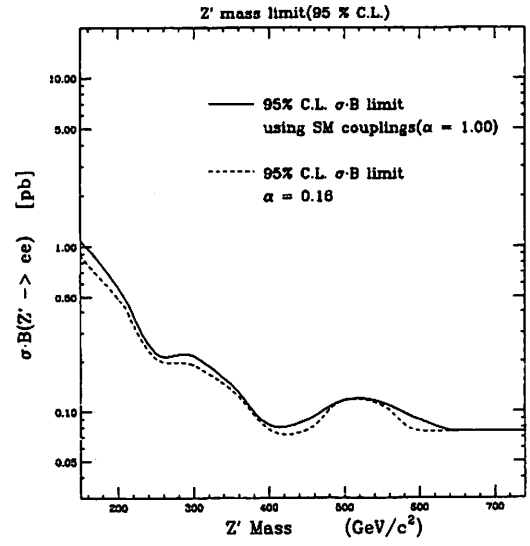

5.7
- (b) 95% C.L. limits on $\sigma_{Z'} \cdot \mathrm{B}(Z' \to e^+e^-)$ for different $\Gamma_{Z'}$.

Figure 5.7: Top figure shows dielectron invariant mass distributions for different $\Gamma_{Z'}$, α =0.16 and 1.00. Solid histogram is the mass distribution with α =0.16, and dotted histogram is one with α =1.00. Bottom figure shows 95% C.L. limits on $\sigma_{Z'} \cdot \mathrm{B}(Z' \to e^+e^-)$ for different $\Gamma_{Z'}$, α =0.16 and 1.00.

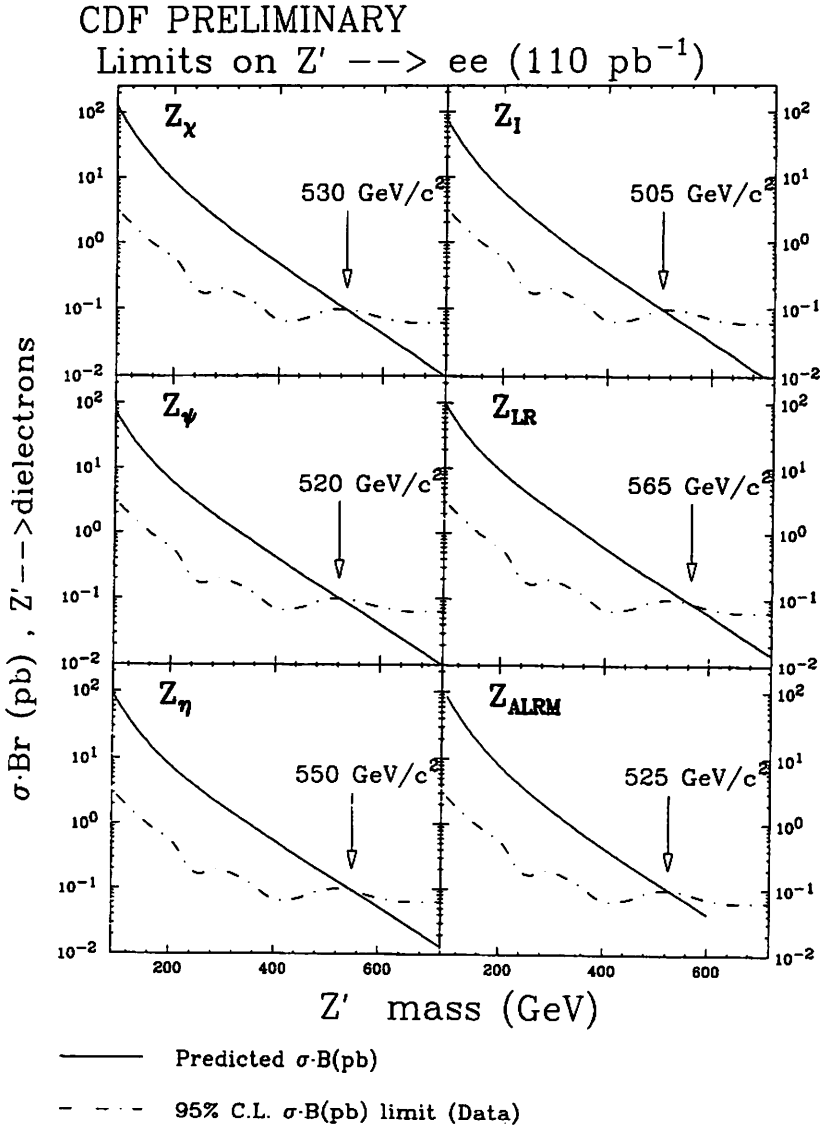

Figure 5.8: The 95% C.L. lower mass limit for five different Z' models from the E_6 symmetry group and one for a right-handed Z' in the Alternative Left-Right model (ALRM). The dashed curve in each plot is the $\sigma_{Z'} \cdot \mathrm{B}(Z' \to e^+e^-)$. The solid curves in figures are $\sigma_{Z'} \cdot \mathrm{B}(Z' \to e^+e^-)$ calculated for the six models, namely Z_χ, Z_ψ, Z_η, Z_I, Z_LR and Z_ALRM. The intersections of the solid and dashed curves set the lower mass limit for each case.

Chapter 6

Conclusions

We have presented a search for additional neutral heavy bosons in dielectron decay mode in $\bar{p}p$ collisions at $\sqrt{s} = 1.8$ TeV using the CDF detector. The data were collected during the 1992-1993 and 1994-1995 runs corresponding to an integrated luminosity of 110 pb^{-1}. The largest invariant mass observed is 511 GeV/c^2. The observed dielectron invariant mass distribution is consistent with the expected one from background processes. We obtain a 95% confidence level limit on the production cross section times branching ratio for a Z' decaying into an electron pair($\sigma_{Z'} \cdot \mathrm{B}(Z' \to e^+e^-)$) as a function of the dielectron invariant mass. In the mass region above 650 GeV/c^2, the $\sigma_{Z'} \cdot \mathrm{B}(Z' \to e^+e^-)$ is less than 6×10^{-2} pb at 95% confidence level. Assuming standard model coupling strengths, we exclude Z' mass below 655 GeV/c^2 at 95% confidence level. A lower bound on the Z' mass

$$M_{Z'} > 655 \text{ GeV}/c^2 \text{ (at 95\% confidence level)}$$

is obtained. In addition, with assumption that the Z' boson decays only to known particles, we set the lower bounds on the Z' mass for Z_χ, Z_ψ, Z_η,Z_I, Z_{LR} and Z_{ALRM} to be 530, 520, 550, 505, 585 and 525 GeV/c^2, respectively.

Appendix A

W event selection

A W($\rightarrow e\nu$) sample is used for the E_T dependence study in Section 3.3.2. In this appendix, the W sample selection criteria are described.

This sample is made from the high P_T inclusive electron data set. The W sample consists of events which satisfy the following requirements. Each event has an electron candidate which satisfies:

- $E_T > 22$ GeV
- $E_T/P_T < 2.0$
- $|\Delta X| < 3$ cm (track-strip chamber cluster match)
- $|\Delta Z| < 5$ cm (track-strip chamber cluster match)
- $Isolation < 0.1$
- number of 3D track = 1
- $L_{shr} < 0.2$
- $\chi^2_{strip} < 10$
- Not a conversion
- fiducial cut

Events have:

- $\not\!\!E_T > 20$ GeV

- $|Z_{vertex}| < 60$ cm

L_{shr} is a transverse profile of a central electron that allows a comparison of the lateral sharing of energy in the calorimeter towers of an electron cluster to electron shower shapes from test beam data. The variable L_{shr} is defined as

$$L_{shr} = 0.14 \sum_i \frac{E_i^{adj} - E_i^{prob}}{\sqrt{0.14^2 E + (\Delta E_i^{prob})^2}},$$

where E_i^{adj} is the measured energy in a tower adjacent to the seed tower, E_i^{prob} is the expected energy in the adjacent tower , $0.14\sqrt{E}$ is the error on the energy measurement, and ΔE_i^{prob} is error on the energy estimate. E_i^{prob} is calculated using a parameterization from test beam data. χ^2_{strip} is a χ^2 of a fit of the energy deposited on each of the 11 strips in z in the CES shower compared to the test beam shape.

After imposing above requirements, 51026 events are obtained from an integrated luminosity of 90 pb^{-1}. Figure A.1 shows a transverse mass distributions of the W($\rightarrow e\nu$) sample.

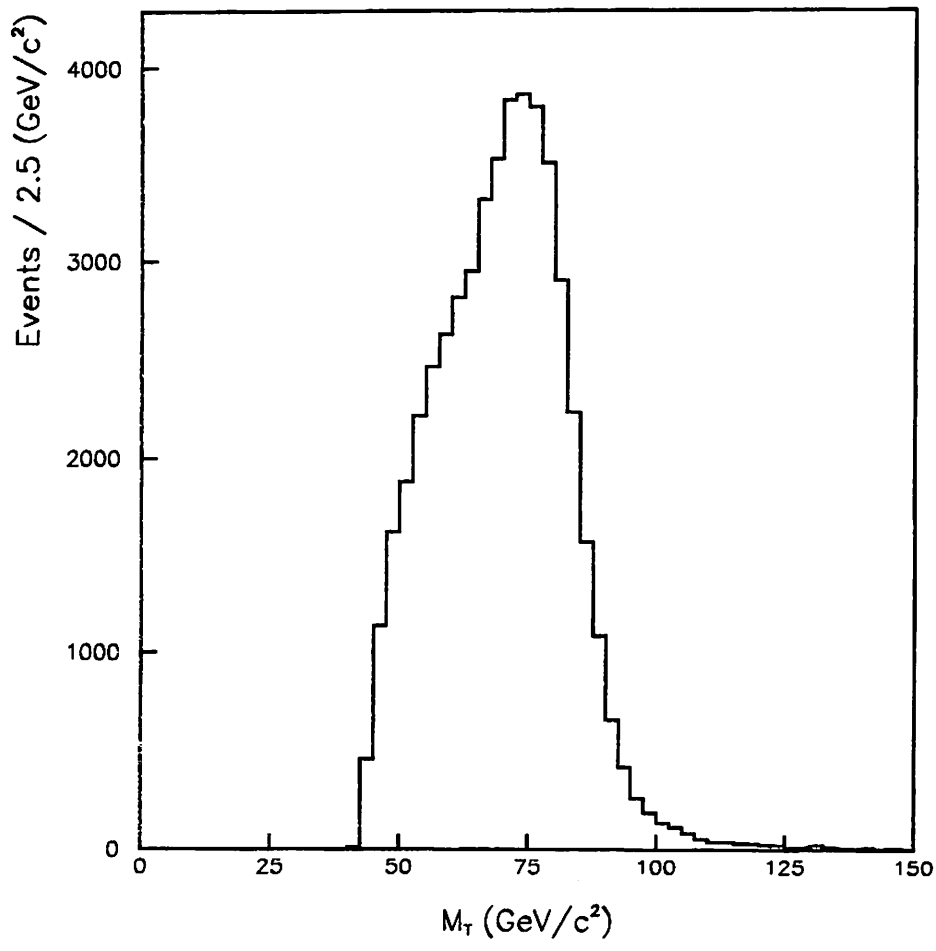

Figure A.1: Transverse mass distribution for $W \rightarrow e\nu$.

Appendix B

Z' search in both dielectron and dimuon decay modes

In this appendix, we describe a brief summary of the Z' search in dielectron and dimuon decay modes at CDF [33]. The details of the Z' search in dimuon decay mode is described in reference [34].

The calorimeters, the Central Tracking Chamber (CTC) and the Muon chambers are the principal detector components used for this search. Data are collected with a multi-level trigger. The electron trigger requires a minimum E_T in the calorimeter with $\sim$ 100% efficiency. The muon trigger requires a match between a Central Muon Chamber stub and a high P_T track in the CTC with $\sim$ 90% efficiency.

Candidate events are selected by requiring one "tight" and one "loose" lepton. Dielectron events are required to have one isolated central electron with $E_T >$ 25 GeV/c^2 and $P_T >$ 13 GeV/c. The second electron could be detected in the Central or in the Plug region of the detector. Muons are required to be a minimum ionizing particle with $P_T >$ 20 GeV/c. One muon is required to be isolated and detected in the Central Muon detector.

We find 7120 dielectron events and 2562 dimuon events. The distribution of these events as a function of invariant mass is shown in Figure B.1. The highest mass e^+e^- and $\mu^+\mu^-$ events have invariant masses of 511 GeV/c^2 and 320 GeV/c^2, respectively. Efficiencies of the lepton identification cuts are determined from a sample of dileptons from Z decays. The geometric and kinematic acceptance were determined from a Monte-Carlo sample of Z and Z' events generated at different masses. The overall acceptance times efficiency rises to 48% for dielectrons and 20% for dimuons at very high Z' invariant mass.

Mass (GeV/c^2)	ee DY+Z+Dijet predict/data	$\mu\mu$ DY+Z predict/data
> 150	68.0 / 70	16.5 / 17
> 200	21.7 / 19	6.2 / 7
> 250	8.1 / 9	2.8 / 4
> 300	3.3 / 6	1.4 / 2
> 350	1.4 / 2	0.7 / 0
> 400	0.7 / 1	0.4 / 0
> 450	0.3 / 1	0.2 / 0
> 500	0.2 / 1	0.1 / 0
> 550	0.1 / 0	0.0 / 0
> 600	0.0 / 0	0.0 / 0

Table B.1: The number of predicted events from Drell-Yan and other backgrounds compared with the data.

When the data is compared with the Standard Model expectation and backgrounds we find no significant excess (see Table B.1). Systematic errors arising from the choice of structure functions and P_T distributions are less than 3%.

The dielectron and dimuon data are combined by assuming that lepton universality holds for Z' decays. Z' mass limits are obtained by comparing the observed data to a superposition of the Standard Model prediction and the expected distribution from Z' decays using the method of binned likelihood. Figure B.2 shows the 95% C.L. limit on the cross section times branching ratio for a Z' decaying to dileptons, as a function of the Z' mass. For a Z' with Standard Model couplings, this translates into a limit of $M_{Z'} > 690$ GeV/c^2 at the 95% C.L. or a limiting cross section of 4×10^{-2} pb for $M_{Z'} > 650$ GeV/c^2. We have also set limits for other interesting theoretical models (see Figure B.3).

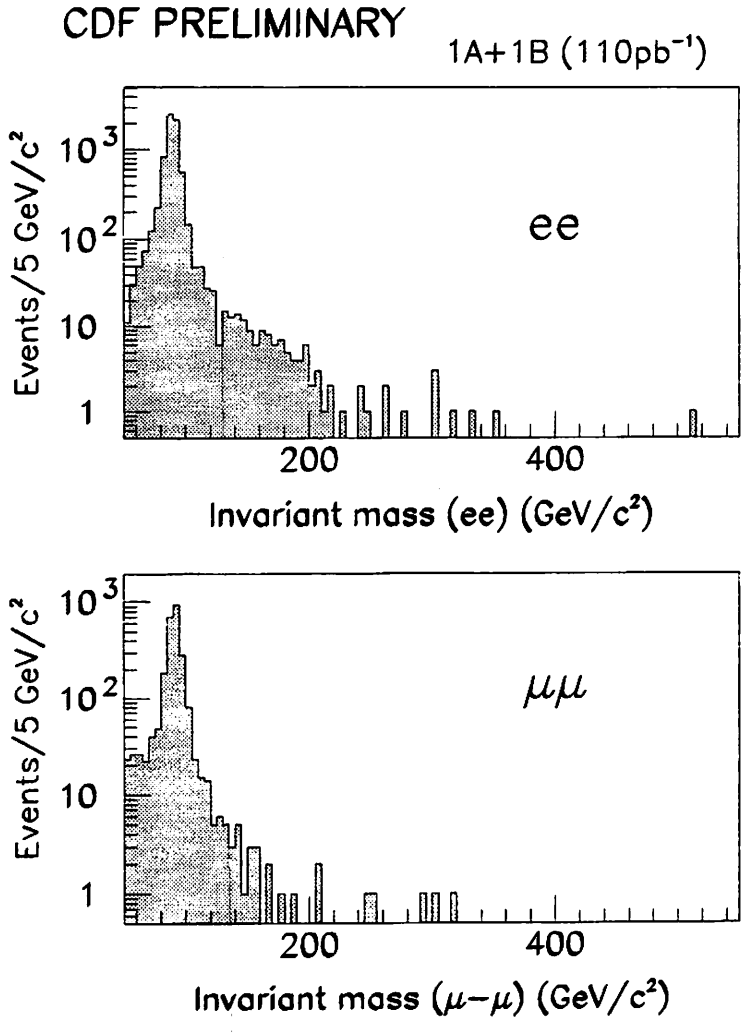

Figure B.1: The invariant Mass distributions for dielectron and dimuon events.

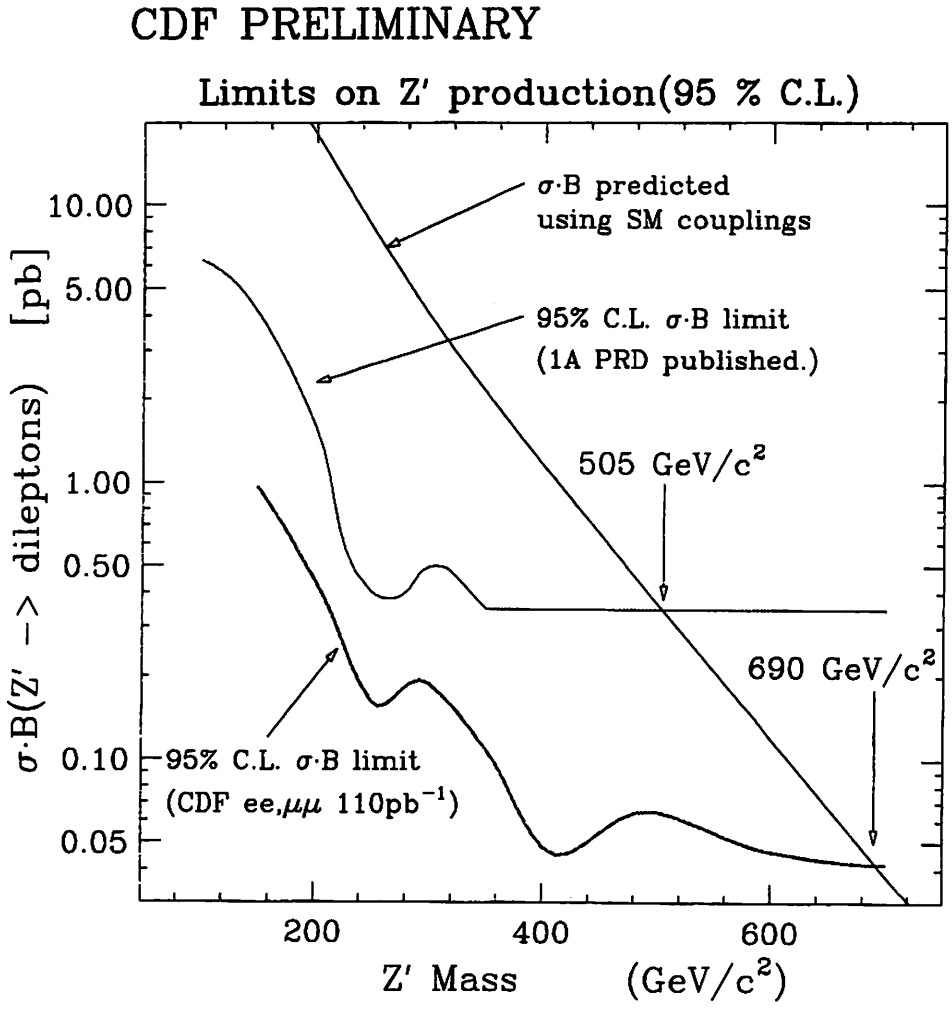

Figure B.2: A 95 % C.L. limit on $\sigma_{Z'} \cdot \mathrm{B}(Z' \to e^+e^-)$ in dielectron and dimuon channels as a function of the dilepton invariant mass. We set a 95% C.L. lower bound on the mass of the Z' boson with the data of 110 pb^{-1}. A 95% C.L. lower limit on Z' boson mass is set to be 690 GeV/c^2.

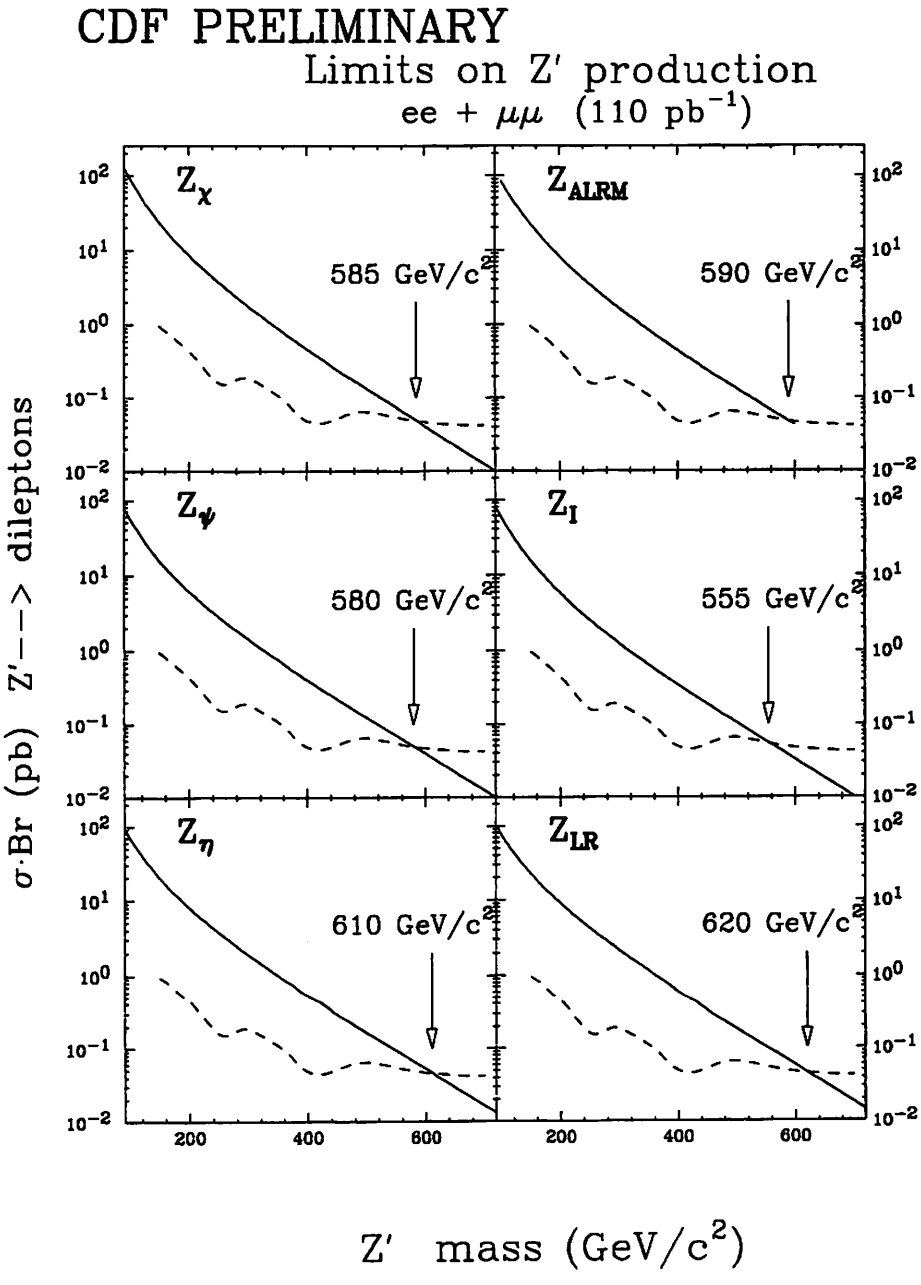

Figure B.3: The 95% C.L. lower mass limits for five different Z' models from the E_6 symmetry group and one for a right-handed Z' in the Alternative Left-Right model (ALRM). The dashed curve in each plot is the $\sigma_{Z'} \cdot \mathrm{B}(Z' \to e^+e^-)$. The intersections of the solid and dashed curves set the lower mass limit for each case.

Bibliography

[1] S.L. Glashow, Nucl. Phys. 22, 579(1961);
S. Weinberg, Phys. Rev. Lett. 19, 1264(1967);
A. Salam, Proc. 8th Nobel Symp.,ed. N.Svartholm(Almqvist and Wiksell, Stockholm and Wiley, New York, 1968).

[2] D.J. Gross and F. Wilczek, Phys. ReV. D8, 3633(1973);D9, 980(1974);
H.D. Politzer, Phys. Rep. 14, 129(1974).

[3] G. G. Ross, *Grand Unified Theories* (Cambridge Univ. Press, Cambridge, England, 1987), and references therein.

[4] L. Hewett and T.G. Rizzo, Phys. Rep. 183, 193(1989).

[5] L. Hewett, preprint SLAC-PUB-95-6960(1995);
F. Feruglio, L. Maiani and A. Masiero, Phys. Lett. B233, 512(1989);
F. del aguila, M. Quiros and F. Zwirner, Nucl. Phys. B287, 457(1987).

[6] Mirjam Cvetič and Paul Langacker, IASSNS-HEP-95/113, (To be appear in Phys. Rev. D, August,1996).

[7] V. Barger, J. Herwett and T. Rizzo, Phys. Rev. D42, 152(1990); G Altarelli et al., Phys. Lett. B261, 146(1991);B263,459(1991); G Bhattacharyya, A. Datta, S.N. Ganguli and A. Raychaudhuri, Mod. Phys. Lett. A6, 2551(1991);
P. Abreu et al.(DELPHI Collaboration), Z. Phys. C65,603(1995); C. Amsler et al.(Crystal Barrel Collaboration), Phys. Lett. B333,271(1994); Frank Cuypers, Int. J. Mod. Phys. A11,1571(1996).

[8] P. Langacker, Phys. Lett. B256, 277(1991).

[9] J. Grifols, E. Masso, T. Rizzo, Phys. Rev. D42, 3293(1990).

[10] F. Abe et al.(CDF Collaboration), Phys. Rev. D51, 3 R949(1995).

[11] M.B. Green and J.H. Schwarz, phys. Lett. B149, 117(1984);
M.B. Green and J.H. Schwarz and E. Witten, *Superstring Theory* (Cambridge Univ. Press, England, 1987) and references therein.

[12] S.T. Yau, Proc. Natl. Acad. Sci. USA, 74, 1798(1977).

[13] V. Barger, N.G. Deshpande, J.L. Rosner and K. Whisnant, Phys. Rev. D35, 2893(1987).

[14] A.Like, S. Riemann and T. Riemann, Phys. Lett. B291,187(1992).

[15] Goran Senjanović, Nucl. Phys. B153, 334(1979); Ernest Ma, preprint, UCRHEP-T149.

[16] F. Feruglio, L. Maiani and A. Masiero, Phys. Lett. B233,512(1989).

[17] E. Ma, Phys. Rev. D36, 274(1987);Mod. Phys. Lett. A3, 319(1988).

[18] L. Montanet *et al.*, Phys. Rev. D50, 1357(1994).

[19] V. Barger and K. Whisnant, Int. J. Mod. Phys. A3, 879(1988).

[20] F. Abe et al.(CDF Collaboration), Nucl. Intrum. Methods Phys. Res. Sect. A 271, 387 (1988).

[21] CERN-Pisa-Rome-Stony Brook Collaboration, Phys. Lett. B62, 460(1976); M. Bozzo et al.(UA4 Collaboration), Phys. Lett. B147, 392(1984).

[22] F. Abe et al.(CDF Collaboration), Phys. Rev. D50, 5518(1994); Phys. Rev. D50, 5550(1994).

[23] C. Grosso-Pilcher et al., "Luminosity for the Top PRL", CDF internal note 3021(1995).

[24] F. Abe et al.(CDF Collaboration), Phys. Rev. D52, 2624(1995).

[25] A.D. Martin, R.G. Roberts and W.J. Stirling, Phys. Lett. B306 145(1993) and Phys. Lett. B309 492(1993).

[26] Frank E.Paige and Serban D. Protopopescu, BNL-38034, 1986 (unpublished).

[27] M. Shapiro et al., "A User's Guide to QFL", CDF internal note 1810(1992).

[28] F. Abe et al.(CDF Collaboration), Phys. Rev. Lett. 77, 448(1996);Phys. Rev. D49, R1(1994).

[29] Phys. Rev. Lett. 76, 3070 (1996).

[30] F. Abe et al.(CDF Collaboration), Phys. Rev. Lett. 74, 18 (1995).

[31] F.Solmitz, Ann, Rev. Nucl. Sci. 14, 375(1964).

[32] F. Abe et al.(CDF Collaboration), Phys. Rev. D43, 3 664(1991).

[33] F. Abe et al.(CDF Collaboration), Proc. of American Physical Society Division of Particle and Fields 1996 Divisional Meeting, Minnesota(1996).

[34] Manoj K. Pillai, Doctoral Thesis, *A Search for New Gauge Boson in $\overline{p}p$ Collisions at $\sqrt{s} = 1.8$ TeV*, University of Rochester(1996).